1-1-2017

System Identification of a Circulation Control Unmanned Aerial Vehicle

Mohammed Agha
University of Denver

System Identification of a Circulation Control Unmanned Aerial Vehicle

---

A Thesis

Presented to

the Faculty of the Daniel Felix Ritchie School of Engineering and Computer Science

University of Denver

In Partial Fulfillment

of the Requirements for the Degree

Master of Science

---

by

Mohammed Agha

November 2017

Advisors: Kimon P. Valavanis, Ph.D. and Matthew J. Rutherford, Ph.D.

Author: Mohammed Agha
Title :System Identification of a Circulation Control Unmanned Aerial Vehicle
Advisors : Kimon P. Valavanis, Ph.D. and Matthew J. Rutherford, Ph.D.
Degree Date : November 2017

Abstract

The advancement in automation and sensory systems in recent years has led to an increase the demand of UAV missions. Due to this increase in demand, the research community has gained interest in investigating UAV performance enhancing systems. Circulation Control (CC), which is an active control flow method used to enhance UAV lift, is a performance enhancing system currently studied. In prior research, experimental studies have shown that Circulation Control wings (CCW) implemented on class-I UAVs can reduce take-off distance by 54%. Wind tunnel tests reveal that CC improves aircraft payload capabilities through lift enhancement. Increasing aircraft payload capabilities causes an increase in UAV applications. Design and implementation of autopilot algorithms making the CC-based UAV capable af autonomous flight increases the number of applications for which it is suited. In this thesis, mathematical models of a CC-based UAV are derived and validated. The mathematical models are used to determine the effects of CC on the stability properties of the UAV. Capturing the dynamics of a CC-based UAV paves the way for designing autopilot algorithms for autonomous flights. Verification experiments demonstrate a good match between the model and UAV (RMS error < 2.5) and good model predictive ability (Theil inequality coefficient is < 0.19). Flight tests reveal the introduction of a nose down pitching moment effect due to CC which changes trim flight values. Parameter estimation is performed to derive stability derivatives that capture the stability properties of the CC UAV.

Acknowledgments

I would like to offer my sincere gratitude to all of those at the University of Denver who helped me complete this thesis. I would like to thank my advisers, Dr. Valavanis and Dr. Rutherford for their guidance throughout this project. I would like to thank Dr. Kanistras for his continuous mentorship and support. I also offer my sincere appreciation to all my colleagues at the University of Denver Unmanned Systems Research Institute.

Finally, I would like to thank my parents, Saeed and Tara, my sister Lara, and all my family and friends for their love and support throughout this process.

This research was partially supported by NSF grant CMMI/DCSD-1728454.

Table of Contents

List of Tables

List of Figures

Chapter 1

Introduction

The research in the field of aviation and the continuous improvement of avionics systems has led to an increase in the usage of Unmanned Aerial Vehicles (UAVs). Today, UAVs are commonly used for aerial photography, landscape surveying, pipeline inspection, and many more applications due to their ability to perform highly dynamic maneuvers, relatively low cost of manufacturing, and elimination of the need of an on board pilot. However, the small size and low payload capabilities of UAVs restrict their applicability to limited missions. Therefore, enhancement of UAV performance is currently a highly active research topic. Circulation Control (CC) is an active flow control method that has been shown to increase aircraft payload through implementation of a Circulation Control Wing (CCW) [10, 11, 12, 13, 14]. Lift enhancement introduces numerous opportunities for new UAV applications such as: reduction in take-off distance, increase of payload capabilities, increase of maximum take-off weight, or delay of aircraft stall. However, implementation of such applications requires extensive understanding of the effects of CCW on aircraft dynamics which in turn is required to design robust autopilot algorithms. Due to the lack of experimental studies on CCW UAVs, there exists little information describing effects of CCW on aircraft aerodynamic properties and there remain many challenges that require

resolution before the CC applications can be implemented. In this thesis, a system identification procedure for capturing mathematical models and performing parameter estimation of an Unmanned Circulation Control Aerial Vehicle (UC^2AV) is presented.

1.1 Motivation

System identification research performed on class-I UAVs has paved the way for implementation of autopilot algorithms, understanding of UAV dynamics, and understanding UAV limitations. Researchers have successfully designed system identification algorithms capable of capturing dynamics introduced by accessory items such as high lift devices (flaps, slats...etc.) [15, 16, 17, 18]. An emerging high-lift device is the Circulation Control Wing. Kanistras et al. [10] have shown that CCW can reduce take-off distance of a small-scale UAV by 54% (Figure 1.1). Further potential applications of CCW are increase in payload capability, increase in maximum take-off weight, or slow speed aerial photography. In order to increase the viability of a CCW UAV capable of performing the aforementioned tasks, an UC^{2}AV platform capable of autonomous flight is researched and implemented. Mathematical models of the UC^{2}AV have been captured to allow designing autopilot controller algorithms. This thesis summarizes the research to capture UC^{2}AV mathematical models through simulation flights, flight testing, and a system identification algorithm.

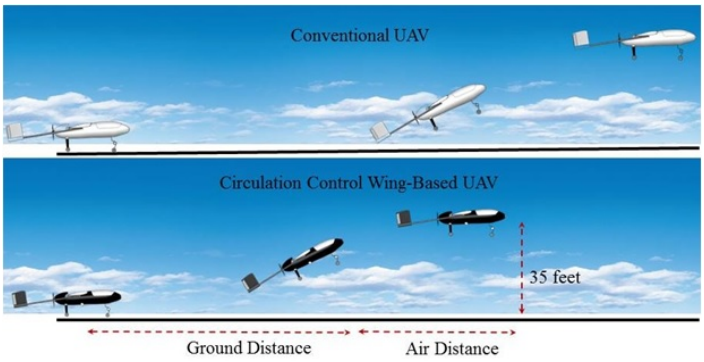

Figure 1.1: CC results in enhancement of lift which leads to reduction in take-off distance.

1.2 Problem Statement

Research on CC in wind tunnel environments and through flight tests has shown that CC has desirable effects on the performance of a UAV. However, wind tunnel tests reveal that CC changes the aircraft's aerodynamic coefficients and introduces a nose down pitching moment effect [13, 9]. These are indications that the stability and control derivatives used to study an aircraft's stability properties are affected by CC. Due to the complexity of designing an efficient UC^{2}AV, the extra weight caused by the addition of a CC system on a UAV, space requirements, and the CC air mass flow rate requirements, few CC-based UAVs have taken flight and the effects of CC on the aerodynamic properties of a UAV remain largely unknown. The following research questions have motivated this work:

- How does CC effect the aerodynamic properties of a Class-I (less than 55 lbs) UAV?
- What are the static and dynamic stability properties of a UC^{2}AV?
- Can linear mathematical models of a UC^{2}AV aimed for controller design be captured using flight testing?
- Can the models capture the CC induced nose down pitching moment effect?

1.3 Methodology

The research focuses on determining a suitable method for performing parameter estimation and derivation of mathematical models of the UC^{2}AV to study the effects of CC on stability and control properties without relying on wind tunnel tests.

The proposed system identification procedure is first tested in a simulation environment. X-Plane flight simulation software is used to create simulation models of the UC^{2}AV and to perform simulation flight tests. The data obtained from simulation tests are processed with Matlab and Simulink. Derivation of mathematical models is performed using CIFER flight identification software. Once the proposed procedure is verified and simulation models are obtained, flight tests are held with the UC^{2}AV in two separate phases, first, with the CC system turned off, and second, with the CC system turned on. CIFER is used again to derive the mathematical models (Figure 1.2). The obtained models are then used to determine the effects of CC on the stability and control derivatives.

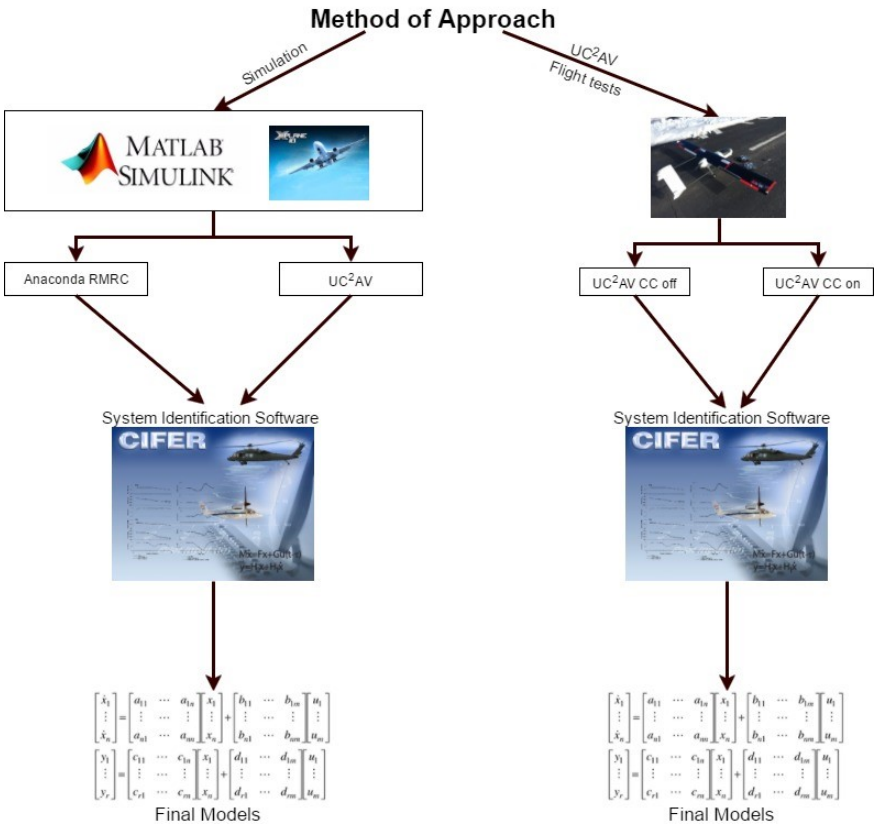

Figure 1.2: The proposed method of approach.

1.4 Summary of Contributions

The primary contribution of this work is the derivation of mathematical models of a UC^{2}AV and investigation of the effects of CC on the mathematical models of the aircraft. To the best of the authors knowledge, there has not been any work on experimental derivation of mathematical models of CC-based UAVs. The contributions of this work are summarized as follows:

- Two sets of mathematical models of the UC^{2}AV (CC on and off) are derived and validated.
- X-Plane Simulation models for the UC^{2}AV that can be used for software in the loop

simulation testing of autopilot algorithms are created and validated using flight data.

- Stability and control derivatives of the UC^{2}AV required for designing autopilot algorithms are identified.

1.5 Organization of the Thesis

The remainder of the thesis is organized as follows: Chapter 2 presents a literature review of circulation control studies highlighting the effects of CC on aircraft dynamic properties and presents a review of system identification algorithms used on class-I fixed wing UAVs. Chapter 3 presents the system identification procedure, the stability properties of a conventional fixed wing UAV and how such properties are affected by CC, along with the mathematical models to be identified. Chapter 4 presents the mathematical models obtained through simulation. Chapter 5 presents the mathematical models obtained through flight testing and the estimated stability and control parameters of the UC^{2}AV. Chapter 6 contains the concluding remarks and future work recommendations.

Chapter 2

Literature Review

There have been many studies conducted to investigate the effects of CC on aircraft aerodynamic properties [11, 9, 19, 20, 21, 8]. Such studies have concluded that CC can be used to enhance aircraft lift but that CC can also cause an increase in drag and a negative pitching moment. Kanistras et al. [11, 22] conducted wind tunnel experiments and flight tests of CC-based UAV and concluded that CC can be used for lift enhancement in UAV platforms as well. Conventional UAV platforms offer numerous advantages over manned aircraft such as the ability to perform highly dynamic maneuvers. Such advantages led to an increase in the demand for autonomous UAV missions. However, payload limitations reduce the number of conventional UAV applications. In order to keep up with demand, researchers have developed many system identification methods to identify the dynamic models of a UAV. Identification of dynamic models in turn allows for the design of autonomous UAV platforms. The chapter begins by presenting background information on CC research in literature and concludes by presenting a comprehensive literature review on UAV system identification methods.

2.1 Circulation Control Background

Circulation Control is an active flow control method that can be used to enhance UAV lift properties [10, 11]. Research conducted proves CC to be the most efficient lift augmentation method when compared to traditional high lift devices such as (flaps, slats,etc.) [22]. CC uses the Coanda effect phenomena for lift enhancement. The tendency of fluids to remain attached to a curved surface is called the Coanda effect. Figure (2.1) shows water attaching to the curved surface of a spoon, this is an illustration of the Coanda effect. A CCW uses the Coanda effect by blowing air at high velocity through slots placed at the trailing edge of the wing (Figure 2.2). Due to the Coanda effect, the curved surface of the wing, and the balance of static pressure, the airflow remains attached to the wing surface and the separation point moves towards the trailing edge of the wing. These changes of the aerodynamics of the wing cause lift enhancement.

Figure 2.1: Illustration of the Coanda effect [23].

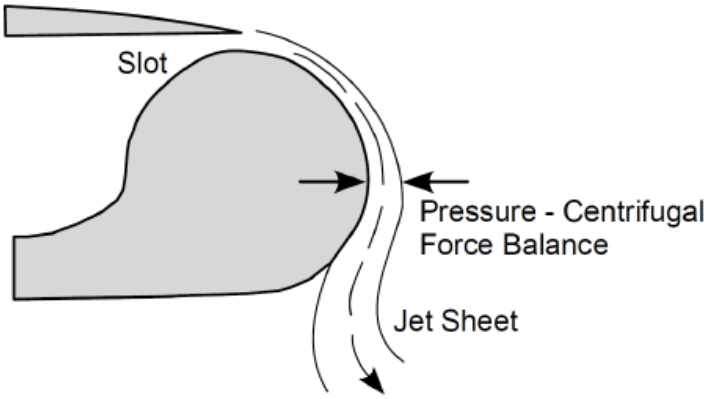

Figure 2.2: Coanda effect seen on a CCW [24].

There have been many wind tunnel studies investigating the effects of CC on the aerodynamic properties of an aircraft [12, 13, 20, 24]. The knowledge gained from such studies is used to optimize and tune a CC design for implementation on an aircraft. Englar in [19] developed a CC airfoil to improve subsonic aircraft lift and cruise performance. Englar defines a momentum blowing coefficient parameter (C_μ) to quantify the intensity of CC blowing. Momentum coefficient of blowing is a crucial parameter when evaluating CC systems (Equation 2.1), it depends on mass flow at the slot ($\dot{m}_j$), air velocity (V_j), free stream velocity (V_∞), the dynamic pressure (q_∞), and the wing surface area (S)

$$C_\mu = \frac{\dot{m}_j V_j}{q_\infty S} \tag{2.1}$$

Englar performed wind tunnel tests to investigate the effects of CC on aircraft lift and pitching moment by varying momentum blowing parameter C_μ, slot height (and slot numbers), and angle of attack. The results obtained indicate enhancement in lift and introduction of a nose down pitching moment effect (Figure 2.3).

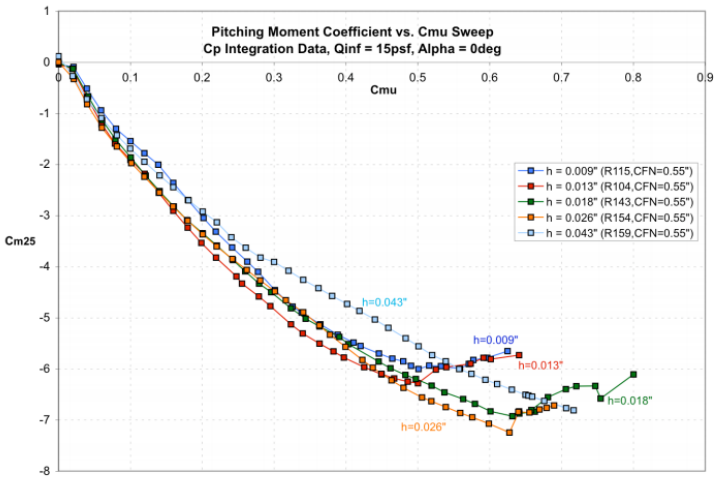

Figure 2.3: Pitching moment variations with C_μ [19].

It can be seen that the negative pitching moment introduced is directly proportional to C_μ. This implies a change in the aircraft trim values. Englar proposes resolving the negative pitching moment either by leading edge blowing or through aircraft control surfaces.

Cagle in [20] presents a CC wind tunnel model that implements unsteady CC pulsed blowing to reduce the total air mass required. The wind tunnel model is used to conduct a study to investigate some of the concerns associated with CCW techniques. The primary concerns investigated are the source of air for internal flow, increase in drag due to bluff trailing edge, nose down pitching moment, and the unknown noise effects of CC. As in [19], Cagle defines the C_μ parameter to quantify the intensity of blowing and to use as the primary control parameter. Results indicate lift enhancement that is directly proportional to C_μ (Figure 2.4), a reduction in drag at velocity ratio of 1.2 ($\frac{U_{jet}}{U_o} = 1.2$, where U_{jet} is the velocity of air at the on board air supply unit and U_o is the exit velocity of air at the CC slots), however the results also indicate an increase in drag at high C_μ values (Figure 2.5), and improvements in lift enhancement with pulsed blowing when compared to steady blowing (Figure 2.6).

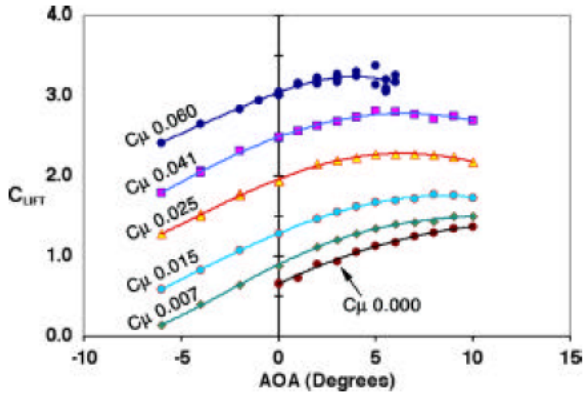

Figure 2.4: Lift enhancement due to CC blowing [20].

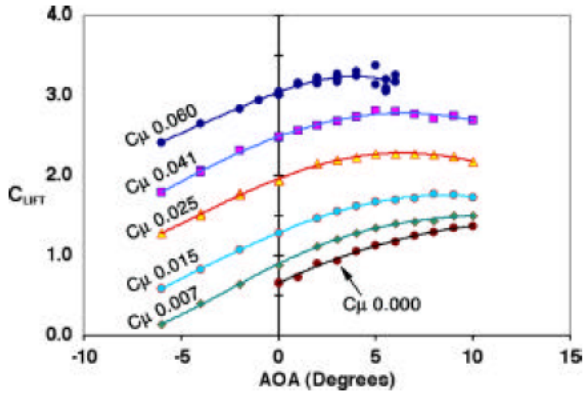

Figure 2.5: CC lift vs. AoA [20].

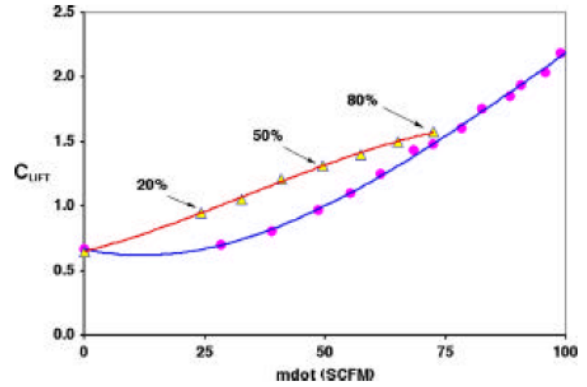

Figure 2.6: Lift enhancement caused by pulsed blowing at 35 Hz and varying duty cycle (orange) and steady blowing (blue) [20].

The results obtained by Englar and Cagle indicate drastic changes to aircraft aerodynamic properties due to CC. Such changes have an effect on aircraft stability, controllability, and dynamic properties. Therefore, it is crucial to understand the new aircraft properties before implementing autonomous CC based UAVs. The remainder of this Chapter presents an overview of the system identification methods used in literature to identify UAV dynamic properties.

2.2 System Identification Methods

System identification is the process of determining mathematical models of aircraft dynamics from input-output information [1]. Inputs signals designed to excite aircraft dynamics are applied to the control surfaces and system identification methods are used to capture the mathematical models of the aircraft. There are two methods for capturing mathematical models; parametric methods and nonparametric methods. Parametric methods are performed when the structure of the mathematical models is known and flight tests are performed to capture the aircraft parameters, this process is also called Parameter Estimation. Nonparametric methods identify the models from impulse or frequency responses without knowledge of model structure. Hoffer et al. [1] conducted a study summarizing the system identification methods used on small-scale UAVs. The study identifies five primary elements of UAV system identification (Figure 2.7):

i *Input Signals*: Inputs signals designed to excite the UAV dynamics are applied to the control surfaces. This is a crucial step in the system identification process as unexcited dynamic modes or the lack of persistent excitation (dynamic modes excited for short periods of time) will result in the dynamic modes not being captured in the identified mathematical models.

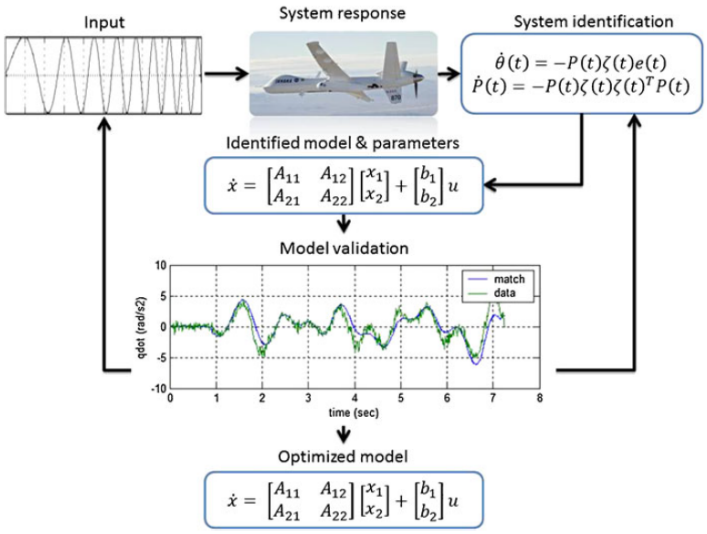

Figure 2.7: System identification process [1].

ii *Data Collection*: There are a number of sensory instrumentation requirements to be considered for accurate model identification. For example, flight data can be extremely noisy due to inherent sensor noise, structural vibrations, and electromagnetic interference. To overcome such issues, adequate signal filtering procedures have to be implemented to obtain low signal to noise ratios. Also, sensor sampling rates must be greater than the dynamic frequencies to capture the dynamic modes.

iii *Selection of the Model Structure*: The model structure to be identified is largely dependent on the end application. For example, if the end application is parameter estimation then the identified model must include the parameters of interest.

iv *Selection of System ID Method*: The system ID method implemented depends on the dynamics of the UAV to be captured and the application of the captured model (Figure 2.8). The UAV dynamics can be time varying or invariant; static or dynamic; linear or nonlinear; and continuous or discrete. Different system ID methods are better suited for different UAV dynamics.

v *Optimization and Verification of the Model*: The identified model requires validation using flight data that were not used for model identification. This is done to test the identified model's ability to predict UAV response. Testing criteria are designed to quantify the model predictive ability such as root mean error analysis or Theil Inequality Coefficient analysis.

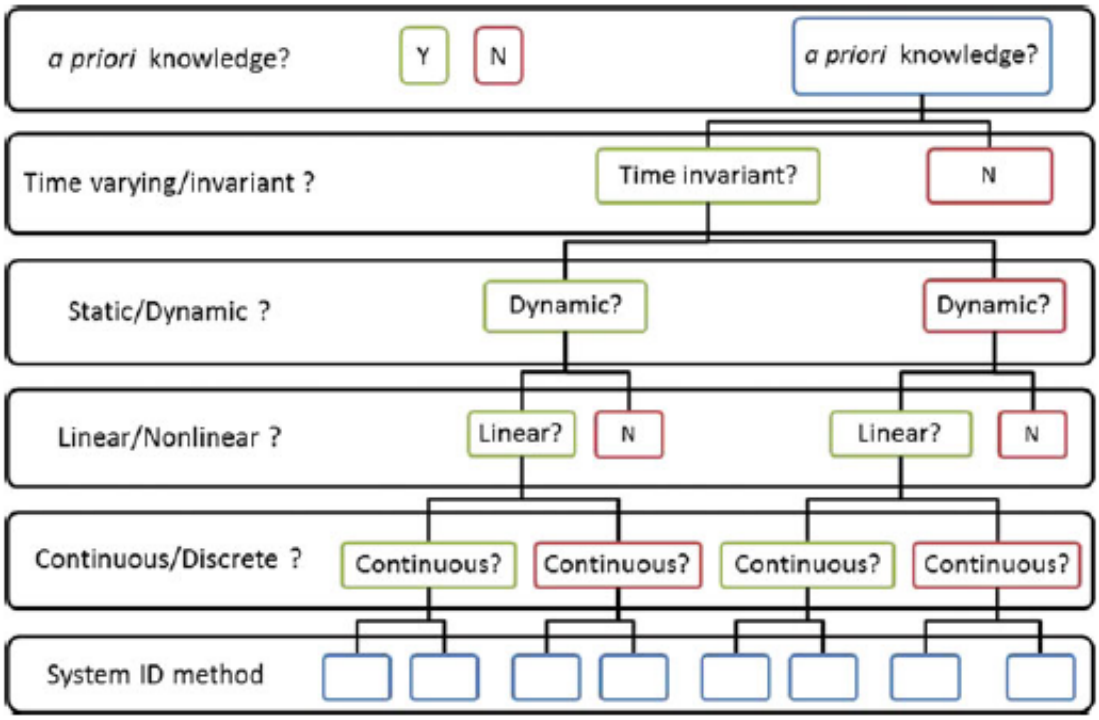

Figure 2.8: System identification method selection [1].

Literature shows that system identification algorithms have been implemented for a variety of applications ranging from parameter estimation, controller design, online system ID, and fault detection (Tables 2.1 and 2.2). Tables 2.1 and 2.2 summarize the system identification methods and their applications [1].

In the remainder of this section, the various nonparametric system identification algorithms are presented starting by presenting classical methods such as equation-error and

Table 2.1: System identification methods and their applications - part 1 [1].

Reference	Data Source	Model	System ID	Application
[15]	MCS	SS	LS	Post-stall dynamics
[25]	MCS	SS	LS	Longitudinal acceleration model
[26]	-	Second order ARX	LS	Motor and servo modeling
[27]	IMU, GPS, DP	Linear SS	Recursive FTR (LS in FD)	RT modeling
[16]	-	SS	FD LS	CSD
[28]	IMU	Fourth Order ARX	LS	Loitering flight model for improved CSD
[29]	IMU,GPS, altimeter, and PS	SS	OEM	Nonlinear CSD
[30]	IMU, GPS, and BS	Linear SS	TD OEM & MLM	Framework for flight CSD
[31]	-	Linear ARX	SOM-based local linear modeling scheme	Development of a set of inverse controllers
[17]	IMU,PS,silde-slip potentiometer, & AoA encoder	ARX	NN	Results validated using RT hardware in the loop
[32]	IMU	NonLinear SS	Model ID	CSD
[33]	IMU	SS	Batch LS	Support & validate autopilot hardware and software
[34]	IMU & GPS	FD to SS	CIFER	CSD
[35]	IMU & GPS	Fifth and First Order ARX	LS	Fractional order CSD
[36]	IMU,GPS,ADS, tachometer, potentiometers, & strain gauges	Mu-Markov parametrization	LS & Online Sys ID	
[37]	IMU,PS, & wind vane	SS	Square Root uKF	Online model ID for control
[38]	IMU,PS,side-slip potentiometer, & AoA encoder	ARX	NN	Comparison of RT online and offline NN models
[39]	-	ARX	Multi-network using NN & batch wise LM	Online and offline NN models for CSD
[40]	-	ARX & MPL	Recurrent NN & batch wise LM	Online and offline NN models for CSD

Table 2.2: System identification methods and their applications - part 2 [1].

Reference	Data Source	Model	System ID	Application
[41]	IMU,GPS, BS, and DP	SS	Online RLS	Control surface fault detection
[42]	-	Fourier transform SS	RT FTR	Fault detection and real time estimation of stability and control derivatives
[43]	Carrier phase differential GPS	SS	Moshe Idan MLM parameter estimation OKID, & subspace	comparison of three system ID methods
[18]	Wind tunnel	SS FD	For SS: EEM LS OEM MLM & for FD: LSR MLM FR	comparison of ID methods and survey of manned and unmanned aircraft
[32]	IMU	SS	Nonlinear mapping & fuzzy ID	Comparison of ID methods
[44]	IMU, GPS, & PS	ARX,ARMAX, & BJ	PEM	Comparison of 3 models of take-off dynamics
[45]	IMU, GPS, & PS	SS	GA based parameter ID & PEM	Comparison of the 2 system ID methods
[46]	IMU	SS	EKF & EMID	Comparison of the two methods
[47]	IMU & GPS	Fifth and first-order ARX	LS	Comparison of & fractional order (PI) CSD
[3]	IMU	FD to SS	CIFER	Baseline model used to design informative flight experiments for FD sys. ID
[48]	IMU,GPS, and PS	ARX for discrete-time, inverse, Z-transform convert to continuous-time & FD for small order model	LS	Sys. ID method proposal
[49]	IMU,GPS, and PS	SS	Nonlinear constrained optimization algorithm	Undergradaute education in UAVs
[50]	-	ARX	-	Autopilot tuning

output-error methods and Frequency domain methods. Afterwards, the artificial intelligence methods enabled by recent technology advances in computation are presented.

2.2.1 Equation-Error and Output-Error Methods

The aim of equation-error methods is determining the aerodynamic parameter estimates that minimize a least square cost function. The cost function is hence defined as the squared difference between model parameters estimated and model parameters obtained through flight testing. Equation-error methods are commonly used for parameter estimation purposes (Tables 2.1 and 2.2).

Klein and Morelli have illustrated the use of equation-error methods for parameter estimation in [51, 52]. Suppose that parameter estimation is to be performed to determine the derivatives shown below:

$$
\begin{aligned}
C_X = -C_A = \frac{(ma_x - T)}{\bar{q}S} C_Y = \frac{ma_y}{\bar{q}S} \quad C_Z = -C_N = \frac{ma_z}{\bar{q}S} \\
C_D = -C_x cos\alpha - C_z sin\alpha C_L = -C_z cos\alpha + C_X sin\alpha \\
C_l = \frac{I_x}{\bar{q}Sb}[\dot{p} - \frac{I_{xz}}{I_x}(pq + \dot{r} + \frac{I_z - I_y}{I_x})qr] \\
C_m = \frac{I_y}{\bar{q}S\bar{c}}[\dot{q} + \frac{(I_x - I_z)}{I_y}pr + \frac{I_{xz}}{I_y}(p^2 - r^2)] \\
C_n = \frac{I_z}{\bar{q}Sb}[\dot{r} - \frac{I_{xz}}{I_z}(p - qr) + \frac{(I_y - I_x)}{I_z}pq]
\end{aligned}
\tag{2.2}
$$

The coefficients appearing in Equation (2.2) can be modeled and represented with measurable aircraft states and controls. Although the models can vary depending on the aircraft configuration, the typical linear models are:

$$
\begin{aligned}
C_L &= C_{L_\alpha}\alpha + C_{L_{\delta_s}}\delta_s + C_{L_o} \\
C_D &= C_{D_\alpha}\alpha + C_{D_{\delta_s}}\delta_s + C_{D_o} \\
C_m &= C_{m_\alpha}\alpha + C_{m_q}\frac{q\bar{c}}{2V_o} + C_{m_{\delta_s}}\delta_s + C_{m_o} \\
C_Y &= C_{Y_\beta}\beta + C_{Y_{\delta_r}}\delta_r + C_{Y_o} \\
C_l &= C_{l_\beta}\beta + C_{l_p}\frac{pb}{2V_o} + C_{l_r}\frac{rb}{2V_o} + C_{l_{\delta_a}}\delta_a + C_{l_{\delta_r}}\delta_r + C_{l_o} \\
C_n &= C_{n_\beta}\beta + C_{n_p}\frac{pb}{2V_o} + C_{n_r}\frac{rb}{2V_o} + C_{n_{\delta_a}}\delta_a + C_{n_{\delta_r}}\delta_r + C_{n_o}
\end{aligned}
\tag{2.3}
$$

The equations above can be represented with a general model structure as shown:

$$
z(i) = \theta_o + \sum_{j=1}^{n} \theta_j \xi_j(j) + v(i) \quad i = 1, 2, ..., N \tag{2.4}
$$

where $z(i)$ are the output measurements, θ are the model parameters and are constant, ξ are explanatory data vector and are called regressors, $v(i)$ is measurement noise, and N is the number of data points. Equation (2.4) is called a regressor function. Assuming that the model parameters are unknown constants and that the measurement vector are affected by random noise, estimates of model parameters $\hat{\theta}$ can be obtained using the Least Squares method [52]. The least square method estimates $\hat{\theta}$ by minimizing the cost function J which is the sum of the squared differences between the estimated parameters and the model (Equation 2.5).

$$
J(\theta) = \frac{1}{2}(z - X\theta)^T(z - X\theta) \tag{2.5}
$$

The estimator equation based on the least square is [52]:

$$
\hat{\theta} = (X^T X)^{-1} X^T z \tag{2.6}
$$

Parameter Estimation using least square algorithm has been performed on full-scale aircraft [52] and class I UAVs (Tables 2.1 and 2.2). Hoffer in [2] implements a recursive least square method and an Error Filtering Online Learning (EFOL) filter to identify the mathematical models of a Minion UAV (Figure 2.9). The recursive least square method identifies the parameters a and b in Equation (2.7) by measuring state values x, state derivatives $\dot{x}$, and inputs u. However, not all measurements for state derivatives $\dot{x}$ are available. EFOL is implemented to measure the state derivatives as simply differentiating the states x leads to noise amplification.

Figure 2.9: Minion UAV [2].

$$\dot{x} = ax + bu \tag{2.7}$$

The linear longitudinal models to be identified using recursive least square is represented in Equation (2.8) where the additional column vector $e_{f1...4}$ is the errors associated with measurements and parameter estimations.

$$\begin{bmatrix} \Delta\dot{u} \\ \Delta\dot{w} \\ \Delta\dot{q} \\ \Delta\dot{\theta} \end{bmatrix} = \begin{bmatrix} \hat{A_{11}} & \hat{A_{12}} & \hat{A_{13}} & \hat{A_{14}} \\ \hat{A_{21}} & \hat{A_{22}} & \hat{A_{23}} & \hat{A_{24}} \\ \hat{A_{31}} & \hat{A_{32}} & \hat{A_{33}} & 0 \\ 0 & 0 & 1 & 0 \end{bmatrix} \begin{bmatrix} \Delta u \\ \Delta w \\ \Delta q \\ \Delta\theta \end{bmatrix} + \begin{bmatrix} \hat{B}_1 \\ \hat{B}_2 \\ \hat{B}_3 \\ 0 \end{bmatrix} \Delta\delta_e + \begin{bmatrix} e_{f_1} \\ e_{f_2} \\ e_{f_3} \\ e_{f_4} \end{bmatrix} \tag{2.8}$$

EFOL is applied to filter high frequency noise and eliminate the use of differentiation for estimating state derivatives $\dot{x}$. This is done by converting the model in Equation (2.8) to the Laplace domain. The Laplace domain model is filtered with a low pass first order filter Equation (2.9).

$$\frac{\lambda}{s+\lambda} \tag{2.9}$$

To estimate unmeasured state derivatives, the low pass filter is modified as shown in Equation (2.10). The modified filter can be implemented as shown in Equation (2.11) which eliminates the need for differentiation.

$$\frac{\lambda s}{s+\lambda} \tag{2.10}$$

$$\lambda(1 - \frac{\lambda}{s+\lambda}) \tag{2.11}$$

The models are converted back to the time domain and rewritten to a linear model as shown in Equation (2.12) where χ is the filtered state derivatives, $\hat{\theta}$ is parameter estimates, ζ is the filtered states, and δ are the filtered errors. By introducing an additional covariance matrix P, recursive least square algorithm can be implemented to estimate the change in parameters and covariance as shown in Equations (2.13) and (2.14).

$$\chi = \hat{\theta}\zeta + \delta \tag{2.12}$$

$$\dot{\hat{\theta}} = -P(t)\zeta(t)\delta \quad \theta(0) = \theta_0 \tag{2.13}$$

$$\dot{P} = -P(t)\zeta(t)\zeta(t)^T P(t) \quad P(0) = P_0 \tag{2.14}$$

Then the parameters are integrated:

$$\hat{\theta} = \int \dot{\hat{\theta}} dt \tag{2.15}$$

$$P = \int \dot{P} dt \tag{2.16}$$

Implementation of the presented recursive least square algorithm requires flight data. The system ID process uses seven sets of chirp maneuvers to calculate the models presented. Validation of the models is performed by comparing the response of the aircraft to sine wave, doublet, and singlet inputs to the response of the models to the same inputs (Figure 2.10).

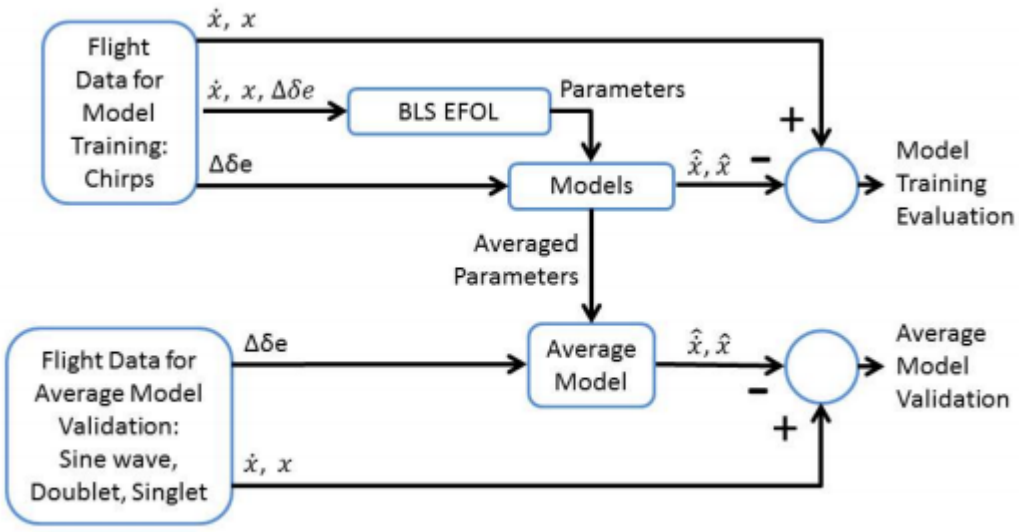

Figure 2.10: Method of approach includes training and validation phases [2].

The parameters of Equation (2.7) are identified using BLS (batch least squares) and BLS with EFOL. The results obtained indicate that using BLS with EFOL does not degrade the accuracy of the identified models (Table 2.3). Parameter estimation is performed using the identified parameters of the longitudinal model to solve for the aerodynamic coefficients of interest.

Table 2.3: Summary of the identified aerodynamic coefficients [2].

Parameter	***BLS mean***	***BLS std***	***EFOL mean***	***EFOL std***
C_X	-0.0064	0.0020	-0.0064	0.0020
C_Z	-0.026	0.0080	-0.026	0.0080
C_m	-0.52	0.45	-0.53	0.46
$C_{X,\alpha}$	0.013	0.017	0.013	0.017
$C_{Z,\alpha}$	-0.36	0.046	-0.36	0.046
$C_{m,\alpha}$	-17.56	4.62	-17.70	4.71
$C_{X,q}$	0.00058	0.0023	0.00057	0.0023
$C_{Z,q}$	-0.027	0.0076	-0.027	0.0076
$C_{m,q}$	-0.45	0.58	-0.43	0.59
C_{X,δ_e}	-0.0013	0.0079	-0.0013	0.0080
C_{Z,δ_e}	-0.055	0.027	-0.056	0.028
C_{m,δ_e}	-15.10	2.27	-15.17	2.28

Sine maneuvers (Figure 2.11) are used to validate the identified model's ability to respond to elevator inputs. Doublet and singlet maneuvers (Figures 2.12 and 2.13) are used to excite both short and long period dynamics. The main different between the doublet/singlet and the sine wave maneuvers is that after the control signal is given, the aircraft is allowed to freely oscillate at low frequencies. Therefore, these signals allow evaluate how well the identified model captures the long period dynamics (Figures 2.14, 2.15, and 2.16).

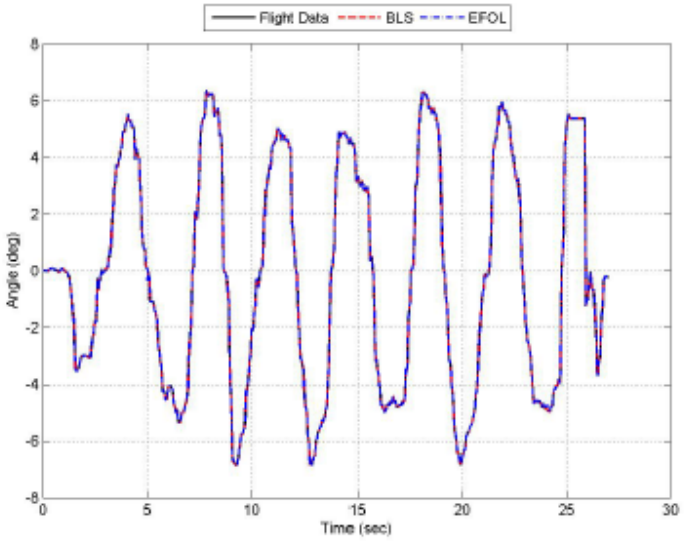

Fig. 8.7: The sine wave elevator command angle.

Figure 2.11: Sine maneuver input [2].

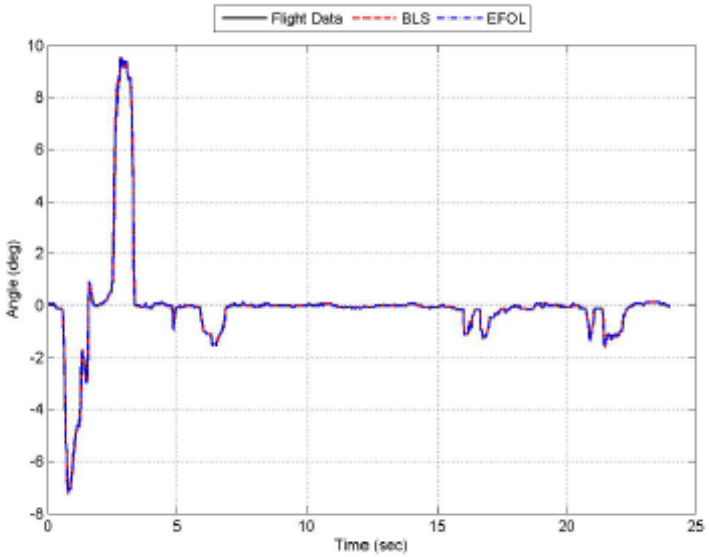

Figure 2.12: Doublet maneuver input [2].

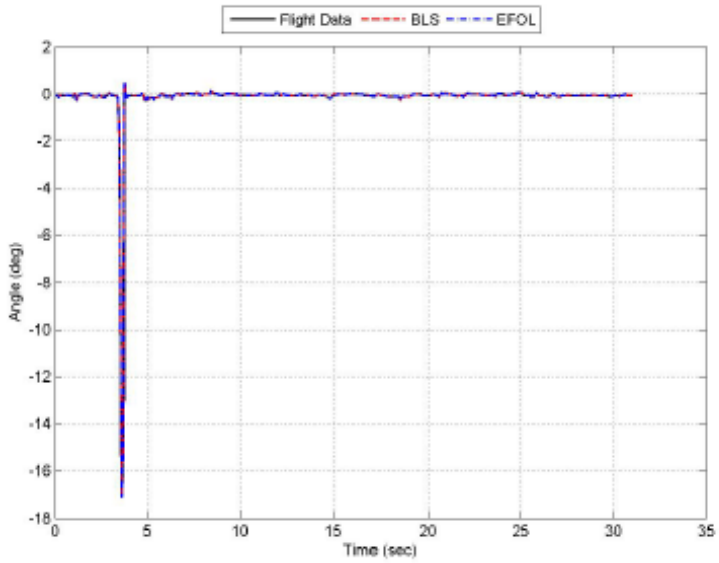

Figure 2.13: Singlet maneuver input [2].

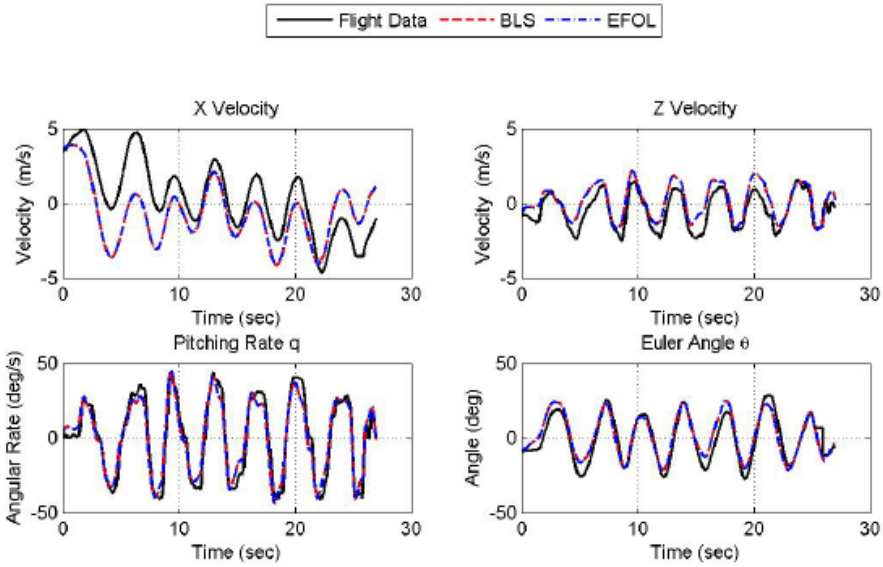

Figure 2.14: The state comparison of flight data to the BLS and BLS with EFOL models using sine wave inputs [2].

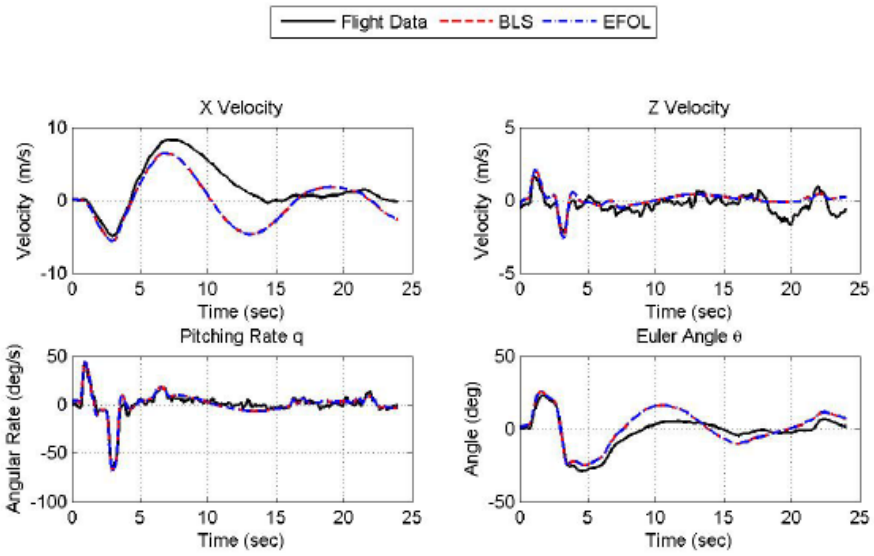

Figure 2.15: The state comparison of flight data to the BLS and BLS with EFOL models using doublet signal inputs [2].

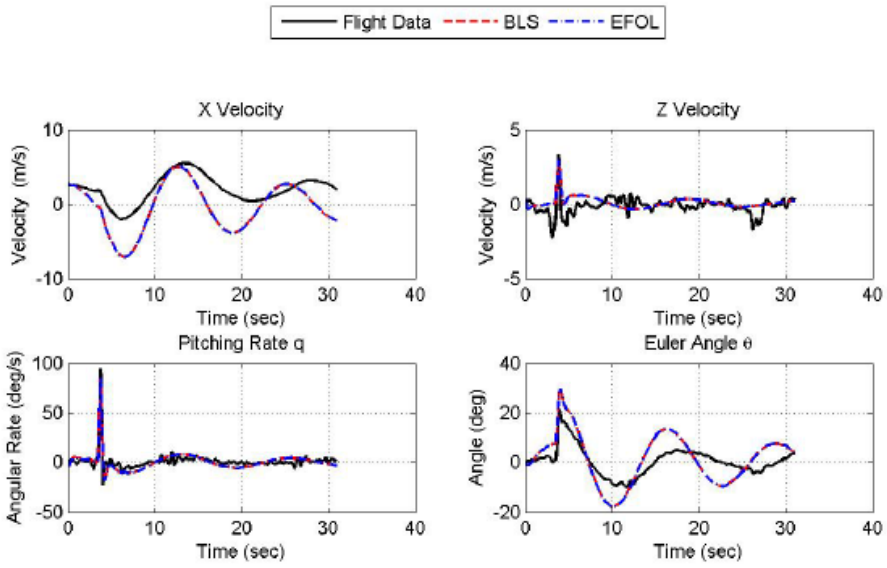

Figure 2.16: The state comparison of flight data to the BLS and BLS with EFOL models using singlet signal inputs [2].

The identified models are able to capture the oscillatory motion of the UAV when the input is a sine wave. However, the models are not able to capture the oscillatory motion

when the input is a doublet or singlet input (Table 2.4). To resolve the issue, either the doublet or singlet data can be used for model identification to increase the amount of training data.

Table 2.4: Mean error values from comparison of flight data to the identified models [2].

Parameters	***Sine wave***		***Doublet***		***Singlet***	
	BLS	***EFOL***	***BLS***	***EFOL***	***BLS***	***EFOL***
$\dot{u}[m/s^2]$	0.6899	0.6902	0.8134	0.8151	0.8905	0.8969
$\dot{w}[m/s^2]$	0.9170	0.9178	1.220	1.222	1.255	1.255
$\dot{\theta}[deg/s]$	5.184	5.202	2.951	2.979	3.661	3.672
$u[m/s]$	1.806	1.811	2.118	2.119	2.519	2.521
$w[m/s]$	0.6400	0.6411	0.4682	0.4686	0.4487	0.4497
$q[deg/s]$	5.184	5.202	2.951	2.979	3.661	3.672
$\theta[deg]$	4.721	4.738	5.236	5.242	5.821	5.861

The presented equation error method is able to identify models with acceptable predictive ability. However, model validation indicates that the derived models are able to capture the dynamics of the UAV only when the input provided is a sinusoidal signal. This is expected as sinusoidal signals of varying frequencies (chirp signals) are used for model derivation. Whereas the models are unable to accurately capture the UAV dynamics when the input signals are not oscillatory (doublet or singlet inputs) even when extra care is taken into eliminating data noise.

2.2.2 Frequency Domain Methods

The time domain methods presented in the previous section and shown in Tables 2.1 and 2.2 can be implemented in the frequency domain by converting the data recorded to

the frequency domain using Fourier transform. Data conversion to frequency domain has advantages such as: fewer data points, which leads to faster computation time. On average, system identification of a UAV consists of identifying the dynamics of nine states (linear accelerations, aerodynamic angles, AoA, side slip angle,etc.) and four control surfaces (elevator, rudder, aileron, and throttle). For a 50 second maneuver sampled at 50 Hz, this leads to $50 \times 50 \times 9 \times 4 = 90,000$ data points to be processed. However, system identification in the frequency domain significantly reduces the number of data points to be processed by performing system identification at discrete frequency values (typically 20 values). The total data points becomes $20 \times 2 \times 9 \times 4 = 1440$. Frequency domain system identification, unlike time domain, does not require the identification of a noise model as noise sources can be handled by the system identification algorithms [53]. Researchers have implemented many system identification methods in the frequency domain (Tables 2.1 and 2.2). CIFER is the most commonly used software for system identification in the frequency domain. The remainder of this section presents the use of CIFER in literature.

Dorobantu et al. [3] use CIFER and wind tunnel tests to identify linear longitudinal and lateral models of a class-1 UAV (Figure 2.17). The longitudinal and lateral model structures are identified analytically using Newton-Euler equations and are linearized by assuming small perturbation theory Equations (2.17 and 2.18). The model structure appearing in the equations are expressed using stability/control derivatives and aircraft inertial and mass measurements.

$$M_{lon}\dot{x} = \acute{A}_{lon}x + \acute{B}_{lon}\delta_{elev}$$

$$M_lon = \begin{bmatrix} m & 0 & 0 & 0 \\ 0 & m & 0 & 0 \\ 0 & 0 & I_y & 0 \\ 0 & 0 & 0 & 1 \end{bmatrix} \acute{A}_{lon} = \begin{bmatrix} X_u & X_w & X_q - mW_e & -mgcos\theta_e \\ Z_u & Z_w & Z_q + mU_e & -mgsin\theta_e \\ M_u & M_w & M_q & 0 \\ 0 & 0 & 1 & 0 \end{bmatrix} \acute{B}_{lon} = \begin{bmatrix} X_{\delta_{elev}} \\ Z_{\delta_{elev}} \\ M_{\delta_{elev}} \\ 0 \end{bmatrix} \tag{2.17}$$

$$M_{lat}\dot{x} = \acute{A}_{lat}x + \acute{B}_{lon} \begin{bmatrix} \delta_{ail} \\ \delta_{rud} \end{bmatrix}$$

$$M_lon = \begin{bmatrix} m & 0 & 0 & 0 \\ 0 & I_x & -I_{xz} & 0 \\ 0 & -I_{xz} & I_z & 0 \\ 0 & 0 & 0 & 1 \end{bmatrix} \acute{A}_{lon} = \begin{bmatrix} Y_v & Y_p + mW_e & Y_r - mU_e & mgcos\theta_e \\ L_v & L_p & L_r & 0 \\ N_n & N_p & N_r & 0 \\ 0 & 1 & tan\theta_e & 0 \end{bmatrix} \tag{2.18}$$

$$\acute{B}_{lon} = \begin{bmatrix} Y_{\delta_{ail}} & Y_{\delta_{rud}} \\ L_{\delta_{ail}} & Y_{\delta_{rud}} \\ N_{\delta_{ail}} & Y_{\delta_{rud}} \\ 0 & 0 \end{bmatrix}$$

Figure 2.17: Ultra Stick 25e flight test vehicle [3].

Initial guess estimates for the stability and control derivatives are required by CIFER to perform system identification. Initial guesses are obtained by performing wind tunnel tests on a scaled model of the aircraft. The scaled aircraft is placed in a wind tunnel on a sting. Tunnel airspeed is kept constant while the aerodynamic forces and moments are measured by a sensor. Three wind tunnel tests are conducted: i) sweeping AoA ; ii) sweeping sideslip angle; and iii) control surface deflections to estimate control derivatives. The values obtained of the scaled model can be used to determine system gain and the frequency range of interest.

Frequency sweep signals are applied to the control surfaces to excite system dynamics (Figure 2.18). The sweep signals begin with a 2-3 seconds of trim flight, then sinusoidal sweep signals are applied with continuously increasing frequency, and then the UAV is flown in trim for another 2-3 seconds. Such sweep inputs allow for identification of trim values and identification of the UAV dynamics in a range of discrete frequency values. In order to guarantee sufficiently large signal to noise ratio, an output data amplitude of 10° is required (Figure 2.18).

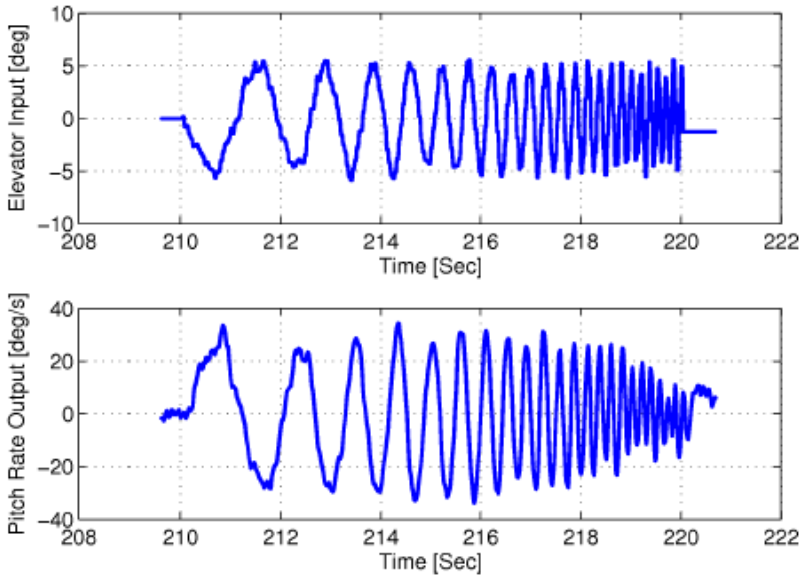

Figure 2.18: Sample of sweep input signal and UAV response [3].

The recorded time-domain data is converted to the frequency domain using chirp Z-transform by CIFER. Frequency spectrum function of the data is calculated and used in CIFER's optimization algorithm. CIFER identifies model parameters by minimizing the cost function (J). The cost function that can be seen in Equation (2.19) is the squared difference of magnitude and phase of the data and the identified model.

$$J = \sum_{l=1}^{N_{TF}} \left(\frac{20}{n_\omega} \times \sum_{\omega_1}^{\omega_{n_\omega}} W_\gamma [W_g (|\hat{T}_c| - |T|)^2 + W_p (\angle \hat{T}_c - \angle \hat{T})^2] \right)_l \quad (2.19)$$

CIFER is used to derive stability and control derivatives that minimize the cost function J and populate the model structures of Equations (2.17 and 2.18). Analyzing the identified models by determining the eigenvalues allows for identifying the longitudinal and lateral dynamic modes (Tables 2.5 and 2.6). Verification of the models is performed by applying doublet inputs to the control surfaces and comparing the response of the UAV to the response of the models (Figure 2.19).

Table 2.5: Longitudinal dynamic modes of the UAV [3].

Mode	Frequency (read/s)	Damping	Time Constant (sec)
Phugoid	0.497	0.724	12.652
Short Period	13.390	0.736	0.452
Actuator	50.266	0.800	0.125
Time Delay	-	-	0.045

Table 2.6: Lateral dynamic modes of the UAV [3].

Mode	Frequency (read/s)	Damping	Time Constant (sec)
Spiral	0.021	-	294.985
Dutch Roll	6.102	0.329	1.030
Roll	14.912	-	0.421

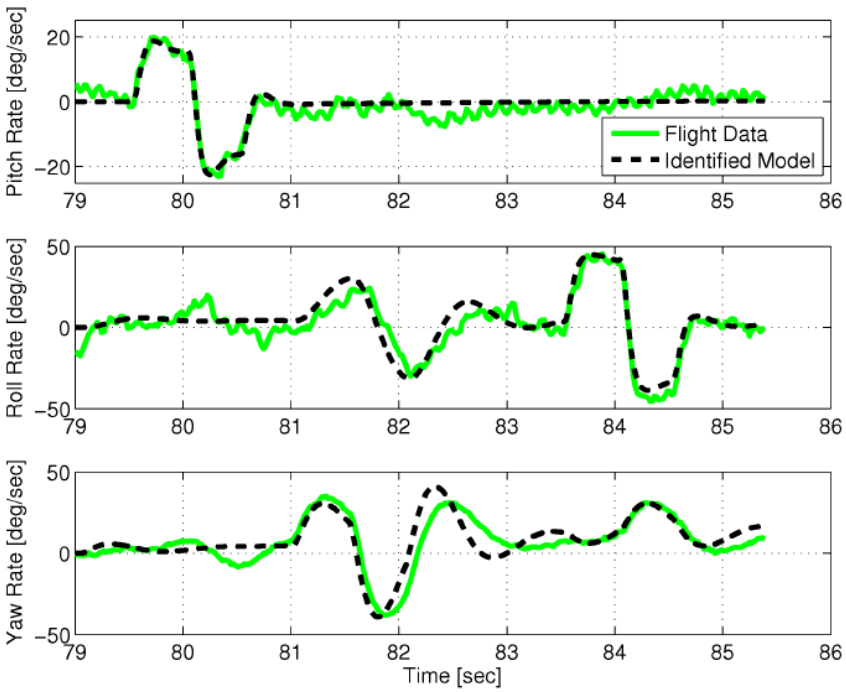

Figure 2.19: Captured flight data vs. model response [3].

Frequency domain system identification using CIFER provides key improvements over time domain methods. Such improvements include the elimination of the requirement to identify a noise model, the ability to directly estimate stability and control derivatives, and reduction of computation time. Dorobantu et al. [3] have shown that CIFER can successfully identify mathematical models with acceptable predictive ability. However, the requirements placed on flight data and the necessity of initial guesses for stability and

control derivatives are the main limitations of CIFER. CIFER requires persistent excitation of dynamics for identification, which limits the identification of lower frequency dynamics.

2.2.3 Neural Network Methods

As described in [4], Artificial Neural Networks (ANN) are a machine learning algorithm inspired by biological neural networks. They are highly interconnected identical processing units which are arranged in an ordered topology. Recent advances in computational power has enabled the implementation of ANN for system identification applications (Tables 2.1 and 2.2). A typical ANN consists of an input layer which has several input neurons, an output layer which has several output neurons, and generally one hidden layer (Figure 2.20). The purpose of the hidden layer is summing the signals of the input layer, scale them in accordance to the assigned weight of the neuron-neuron connection, and passing the resulting signal to a threshold activation function (Figure 2.21).

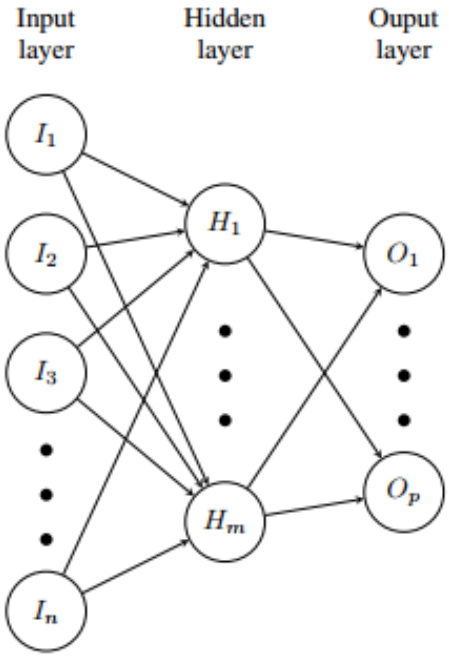

Figure 2.20: ANN layers [4].

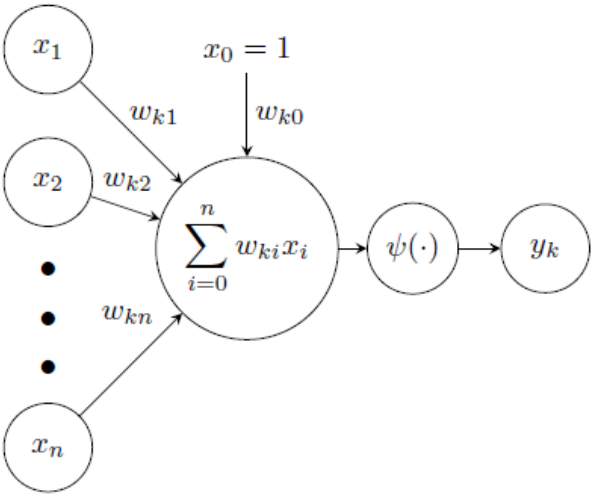

Figure 2.21: The ANN hidden layer sums the input signals, multiplies them by assigned weight values ($w_{k_{0,1,\ldots n}}$), and passes the signal to a threshold activation function ψ [4].

ANN can be used for system identification by identifying the neuron-neuron weights through a process called training. This creates an ANN that resembles the UAV dynamics. Algorithms are implemented to identify the weights from known input (control surfaces) and output (UAV response) flight data.

Harris in [4] uses an ANN method designed by Kirkpatrick in [54] for identifying the dynamic models of the RMRC Anaconda UAV (Figure 2.22). Equation (2.20) shows a standard state-space representation of a UAV model structure. $x(k)$ is the system states, Φ and Γ are the parameters to be identified, and $u(k)$ is the input.

Figure 2.22: RMRC Anaconda UAV [4].

$$\begin{bmatrix} x_1(k+1) \\ x_2(k+1) \end{bmatrix} = \begin{bmatrix} \Phi_{11} & \Phi_{12} \\ \Phi_{21} & \Phi_{22} \end{bmatrix} \begin{bmatrix} x_1(k) \\ x_2(k) \end{bmatrix} + \begin{bmatrix} \Gamma_1 \\ \Gamma_2 \end{bmatrix} u(k) \tag{2.20}$$

An ANN can be created to represent the model in Equation (2.20). To do so, the following have to be taken into consideration:

- The ANN must have no hidden layers, i.e. one input layer and one output layer. This is to guarantee that the weight of the ANN are identical to the Φ and Γ parameters (Figure 2.23).
- The threshold activation function has to be linear in order to not introduce nonlinearities to the model.
- All nodes must have zero bias inputs.

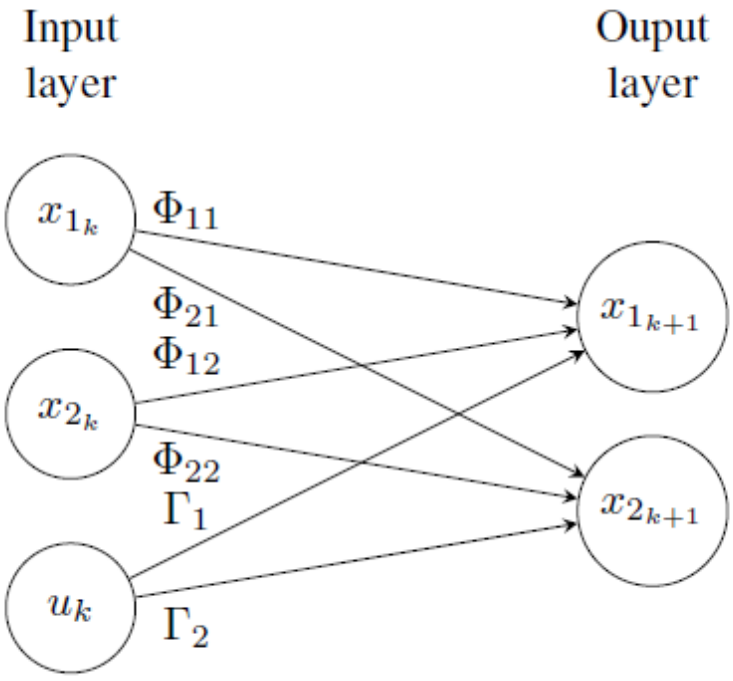

Figure 2.23: ANN without hidden layers [4].

The presented ANN is implemented using the Matlab Neural Network Toolbox [55]. The toolbox takes the control surface and system states time histories as inputs and generates the state-state matrices. However, before the ANN is used to identify the models of the RMRC Anaconda UAV, the ANN is tested by identifying a simulation model of F-16XL experimental jet fighter (Figure 2.9). F-16XL is chosen due its fast dynamics and large number of control surfaces which make it a challenging identification problem. Mathematical model of the F-16XL is separately derived using a well tested Observer/Kalman (OKID) Identification Algorithm.

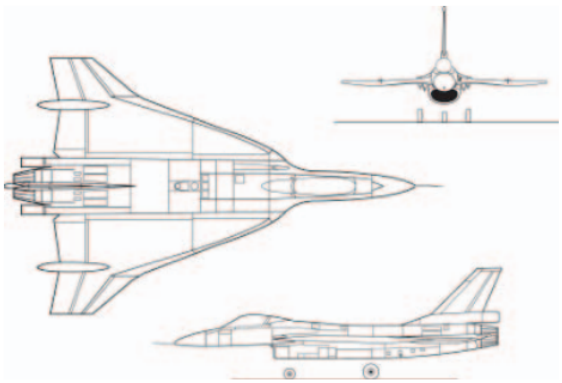

Figure 2.24: 16XL experimental fighter jet [4].

System identification of the F-16XL is done by applying step inputs to every control surface of the aircraft separately to excite the system dynamics. This is done for the longitudinal model and the lateral model. The identified models are then tested using Simulink by comparing the output of the models to the output of the F-16XL and by performing Theil Inequality Coefficient (TIC) analysis. TIC is a normalized measure of the aircraft predictive ability, TIC = 1 indicates the aircraft has no predictive ability while TIC = 0 indicates the aircraft has perfect predictive ability (Figure 2.25 and Table 2.7).

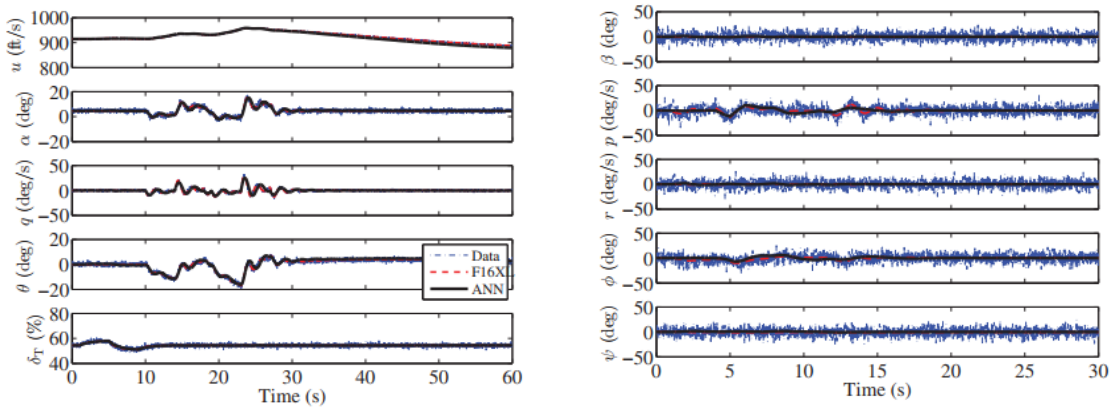

Figure 2.25: Left: Testing the identified longitudinal model vs. simulation data. Right: Testing the identified lateral model vs. simulation data [4].

Table 2.7: F-16XL Theil coefficient values [4].

(a) Longitudinal

Parameter	**TIC**
u	0.2484
α	0.2681
q	0.3805
θ	0.2179
δ_T	0.1996

(b) Lateral

Parameter	**TIC**
β	0.6510
p	0.4518
r	0.6323
ϕ	0.5102
ψ	0.6477

The derived longitudinal model captures the longitudinal dynamics more accurately than the lateral model captures the lateral dynamics (Figure 2.25 and Table 2.7). Harris et al. in [4] set 0.35 as a TIC cutoff. As it can be seen, all but q parameter in the longitudinal model meet the cutoff and none of the parameters in the lateral model meet the cutoff. However, Harris et al. [4] conclude through visual inspection of Figure 2.25 that the identified model exhibits similar enough response to the F-16XL dynamics in order to still be used.

The ANN method is then used to identify the longitudinal and lateral models of the RMRC Anaconda. Step inputs are applied to the RMRC Anaconda control surfaces to excite system dynamics (Figure 2.26). The recorded data is passed through a low pass filter as high frequency noise degrade the ANN algorithm performance. Matlab's Neural Network toolbox is used once more to perform system identification. The identified models are then tested using Simulink by comparing the output of the models to the output of the UAV and by performing Theil Inequality Coefficient analysis (Figure 2.27 and Table 2.8).

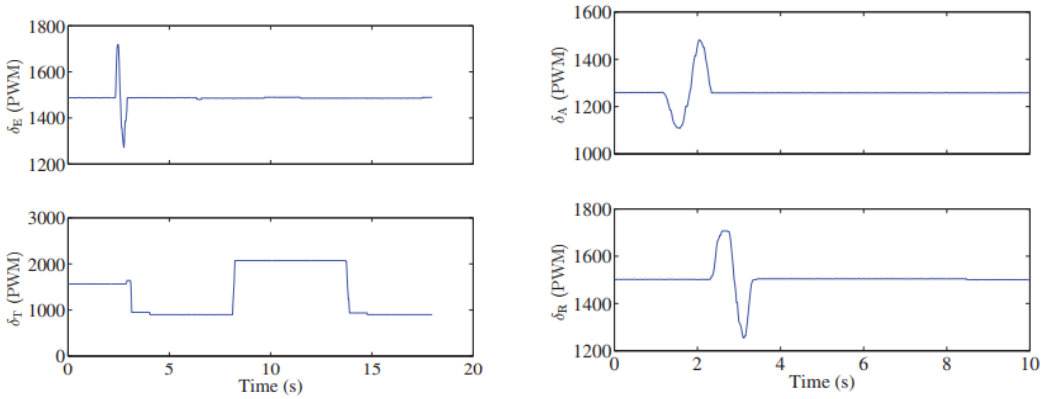

Figure 2.26: Left: Step inputs to excite longitudinal dynamics. Right: Step inputs to excite lateral dynamics [4].

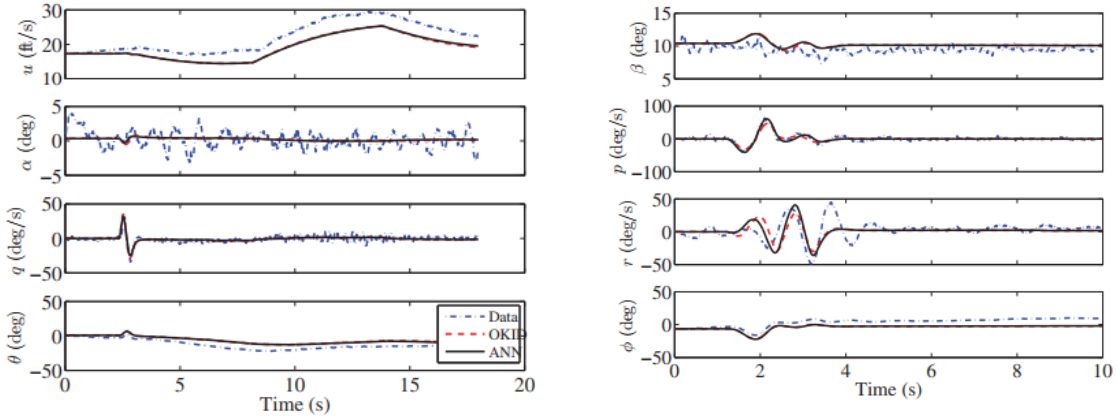

Figure 2.27: Testing the identified longitudinal model vs. flight data. Right: Testing the identified lateral model vs. flight data [4].

Table 2.8: TIC values for RMRC Anaconda [4].

(a) Longitudinal			(b) Lateral		
Parameter	**ANN**	**OKID**	**Parameter**	**TIC**	**OKID**
u	0.4008	0.4032	β	0.5726	0.5682
α	0.6989	0.6985	p	0.3159	0.3533
q	0.4199	0.4125	r	0.4944	0.5391
θ	0.3675	0.3760	ϕ	0.5085	0.5141

Table 2.8 indicates that the identification of angle-of-attack parameter is poor. However, the remaining parameter show acceptable identification results. The TIC values indicate that the ANN algorithm's prediction ability matches the prediction ability of the well tested Observer/Kalman Identification Algorithm.

The presented neural network method accurately identifies the dynamics of the pitch rate of change and roll rate of change variables. However, examination of the TIC values and Figure (2.27) indicates poor model accuracy and predictive ability. This is likely due to the limited duration of data used in the training phase. Training with doublet inputs does not capture the dynamics of the UAV at a range of frequencies. The literature review presented in this chapter has shown that output error and frequency domain methods using CIFER have yielded better results.

2.3 Literature Review Remarks

This chapter presents an overview of the system identification methods used for fixed-wing UAV modeling. A number of studies from the most common approaches are also presented to give detail insights to the system identification methods. A number of observations can be made from the review presented: i) While all method implement an

optimization algorithm (minimization of a cost function), algorithms that require greater time history data tend to produce better models; ii) Equation-error methods can be used to perform parameter estimation successfully, however, validation tests indicated that the model can capture the UAV response only when the input provided has similar properties (constant frequency or oscillatory properties) to the input used during system identification; and iii) The UAV dynamics change with the input frequency, hence, using a doublet input for system identification only captures the dynamics at a discrete frequency value.

The research presented in this thesis aims at deriving mathematical models for autopilot algorithm development and for investigation the effects of CC on UAV stability properties. Equation-error methods has shown that system identification method based on optimization of a cost function can be used for parameter estimation. CIFER implements an optimization algorithm in the frequency domain to perform parameter estimation and to derive mathematical models. Therefore, this research uses CIFER to perform system identification and parameter estimation of the UC^2AV. Parameter estimation is performed in two separate occasions; first, with the CC system turned off; and second, with the CC system turned on. This allows for investigating the effects of CC on UAV stability properties.

Chapter 3

System Identification Procedure

3.1 Introduction

This chapter provides detailed information of the system identification methodology implemented in this thesis. The chapter begins by providing detailed description of the UAV platforms including the CC system. The dynamic equations of motion of a UAV are presented and mathematical models are derived for longitudinal and lateral motion. The effects of CC on the UAV dynamics are also presented. The chapter concludes by presenting the system identification method of approach along with explanation of how the proposed methodology is implemented in simulation environment and flight testing.

3.2 Description of UAV Platforms

System identification is performed on two UAV platforms: the RMRC Anaconda; and the UC^{2}AV. This section provides a description of the two platforms.

3.2.1 RMRC Anaconda

The RMRC Anaconda (Figure 3.1), which is a twin boom inverted V-tail UAV, is chosen as the baseline UAV platform due to its payload capabilities and ample fuselage space for the addition of a CC Air Supply Unit (ASU).

Figure 3.1: Stock RMRC Anaconda UAV.

The RMRC Anaconda has a wing span of 2060 mm, a total weight of 8 lbs, and has a Clark YH airfoil. RMRC Anaconda specifications can be seen in Table 3.1

Table 3.1: RMRC Anaconda specifications [22].

Fuselage			
Length	L	0.8	m
Width	W_{max}	0.11	m
Height	H_{max}	0.16	m
Propeller			
Diameter	D	15	in
Pitch	P	4	in
Number of Blades		2	

3.2.2 UC^{2}AV

The UC^{2}AV platform is created from the RMRC Anaconda by performing the following modifications: i) An ASU unit is added in the fuselage of the RMRC Anaconda along with an air intake inlet; ii) A CCW is manufactured that includes an Air Delivery System (ADS), which consists of tubes used to deliver the air from the ASU to 0.4 mm CC slots located at the trailing edge of the wing. (Figure 3.2)

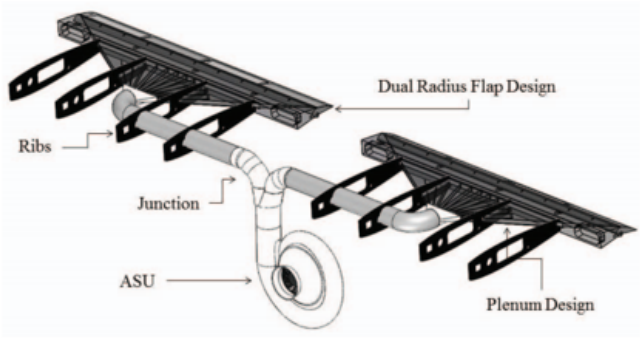

Figure 3.2: The CC system [10].

The ASU is located inside the fuselage and at the center of gravity of the UC^{2}AV. The ASU unit includes a centrifugal compressor that draws air into the CC system through an air intake duct located underneath the fuselage (Figure 3.3).

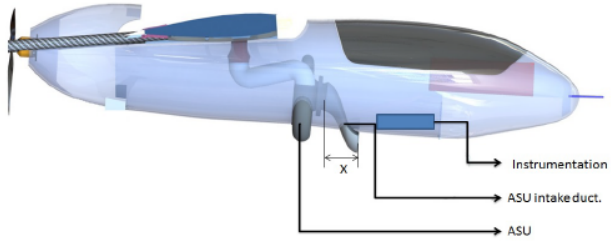

Figure 3.3: The ASU air intake duct is located underneath the fuselage [56].

The UC^{2}AV configuration can be seen in Figure 3.4. Details of the CCW design and implementation of UC^{2}AV can be found in [10, 23].

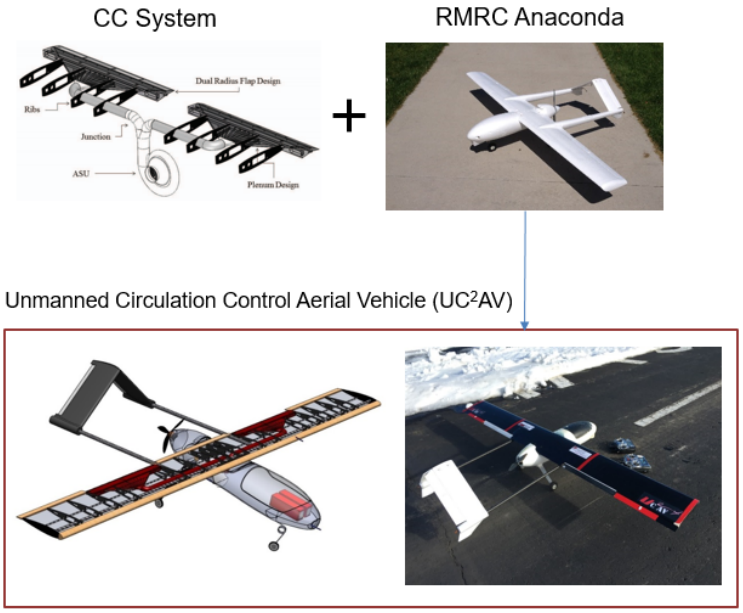

Figure 3.4: The UC^{2}AV platform.

There are a number of important differences between the RMRC Anaconda and the UC^{2}AV (Table 3.2). The UC^{2}AV has one-third aileron surface area of the RMRC Anaconda and is nearly 3 lbs heavier.

Table 3.2: Comparison between RMRC Anaconda and UC^{2}AV

	Wing Span	**Airfoil**	**Total Weight**	**Aileron Area**
RMRC Anaconda	2060 mm	Clark YH	7.70 lbs	240 cm^2
UC^{2}AV	2060 mm	NACA 0015	10.36 lbs	80 cm^2

Identical servo motors and throttle motor are implemented on both UAVs. Ground testing reveals that the servo motors are able to respond to all input signals.

3.3 UAV Flight Dynamics

System identification is the process of representing aerodynamics forces and moments in terms of measurable quantities such as control surface deflection angles, aerodynamic angles (pitch, roll, and yaw), and aircraft linear velocities. These quantities are measured with respect to the earth or body reference frames. Therefore, before proceeding to derivation of mathematical models, the required reference frames have to be defined.

Reference Frames

- Earth Axis x_E, y_E, z_E. The origin of the earth reference frame can be any arbitrary point on the surface of the earth. Positive x_e points towards geographic north, positive y_E points towards east, and z_E points towards the center of the earth. Ignoring the motion of the earth results in making the earth axis identical to the inertial axis which is used when applying Newton's laws.

- Body Axis x_B, y_B, z_E. The origin of the body axis frame is located at the center of gravity of the aircraft. Positive x_B points forward through the nose of the aircraft, positive y_B points in the same direction as the right wing, and positive z_B points downwards from the center of gravity.

The transnational and rotational dynamics of an aircraft can be obtained by treating the aircraft as a rigid body and applying Newton's Laws. A complete derivation of these dynamics equations can be found in [57]. These equations represent the forces acting on the aircraft (X,Y,Z), the moments (L,M,N), aerodynamic angular rates (q,p,r), and the linear velocities (u,v,w) in reference to a fixed coordinate system.

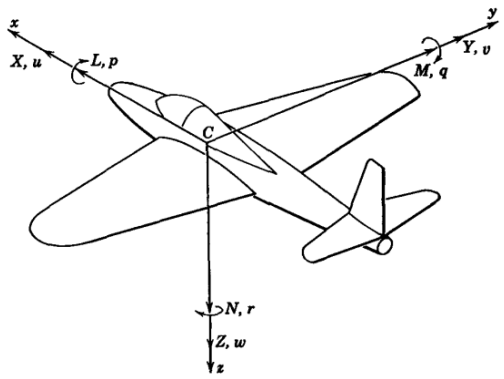

Figure 3.5: The forces, moments, angular rates of change, and the linear velocities of an aircraft [58].

The equations derived in [57] are non-linear. Deriving the non-linear UAV model is a complex process and beyond the scope of this thesis. The non-linear equations are linearized in accordance to the small perturbation theorem which assumes minimal deviation from trim conditions, spinning motor effects are negligible, and wind velocity is zero. These assumptions are valid and applicable to this research as the effects of Circulation Control are present with small perturbation angles, the rotor angular momentum is small, and all flight data is held in calm weather conditions (wind speed $<$ 5 mph). The linearized equations are:

$$X_0 + \Delta X - mg(sin(\theta_0) + \theta cos(\theta_0))) = m\dot{u}$$

$$Y_0 + \Delta Y + mg\phi cos(\theta_0) = m(\dot{v} + u_0 r)$$

$$Z_0 + \Delta Z + mg(cos(\theta_0) - \theta sin(\theta_0) = m(\dot{w} - u_0 q)$$

$$L_0 + \Delta L = I_x\dot{p} - I_{zx}\dot{r}$$

$$M_0 + \Delta M = I_y\dot{q}$$

$$N_0 + \Delta M = -I_{zx}\dot{p} + I_z\dot{r}$$

$$\dot{\theta} = q$$

$$\dot{\phi} = p + rtan(\theta_0), p = \dot{\phi} - \psi sin(\theta_0)$$

$$\dot{\psi} = rsec(\theta_0)$$

Further assumptions are made to simplify the linearized equations. The configuration of the aircraft is assumed to be symmetric. A symmetric configuration implies that the side force Y, rolling moment L, and yawing moment N are zero and that the derivatives of the asymmetric and lateral moments and forces with respect to symmetric and longitudinal parameters are zero. It is also assumed that derivatives with respect to rate of change of motion variables are zero. These assumptions are standard in deriving linear dynamic expressions of aircrafts. These equations are decoupled and presented as longitudinal and lateral dynamics. State-space representations obtained of the decoupled dynamics can be represented in the form:

$$\dot{x} = Ax + Bu$$

where x is the state variable matrix and u is the input control matrix. The state-space representation of the longitudinal and lateral models to be identified are shown below:

$$\begin{bmatrix} \dot{u} \\ \dot{w} \\ \dot{q} \\ \dot{\theta} \end{bmatrix} = \begin{bmatrix} X_u & X_w & 0 & -gcos(\theta_0) \\ Z_u & Z_w & Z_q + mu_0 & -gsin(\theta_0) \\ M_u & M_w & M_q & 0 \\ 0 & 0 & 1 & 0 \end{bmatrix} \begin{bmatrix} u \\ w \\ q \\ \theta \end{bmatrix} + \begin{bmatrix} X_{\delta_e} & X_{\delta_p} \\ Z_{\delta_e} & Z_{\delta_p} \\ M_{\delta_e} & M_{\delta_p} \\ 0 & 0 \end{bmatrix} \begin{bmatrix} \delta_e & \delta_p \end{bmatrix} \tag{3.1}$$

$$\begin{bmatrix} \dot{v} \\ \dot{p} \\ \dot{r} \\ \dot{\phi} \end{bmatrix} = \begin{bmatrix} Y_v & Y_p & Y_r - u_0 & gcos(\theta_0) \\ L_v & L_p & L_r & 0 \\ N_v & N_p & N_r & 0 \\ 0 & 1 & tan(\theta_0) & 0 \end{bmatrix} \begin{bmatrix} v \\ p \\ r \\ \phi \end{bmatrix} + \begin{bmatrix} Y_{\delta_a} & Y_{\delta_r} \\ L_{\delta_a} & L_{\delta_r} \\ N_{\delta_a} & N_{\delta_r} \\ 0 & 0 \end{bmatrix} \begin{bmatrix} \delta_a & \delta_r \end{bmatrix} \tag{3.2}$$

The models above are represented using dimensional stability and control derivatives. The elements appearing in matrix A are the stability derivatives. Stability derivatives are used to determine the effect changes in state variables have on the aerodynamic forces and

moments. They are also a useful measure when studying the static stability of an aircraft as it will be seen in section 3.3.1. Control derivatives which appear in matrix B, can be used to determine the effects changes of the control surfaces (such as elevator deflection angle) have on aerodynamic forces and moments.

3.3.1 Aircraft Stability Properties

Aerodynamic stability is defined by the ability of the aircraft to return to trim after deviating from trim due to natural disturbances (weather disturbances) or control inputs. There are two general types of aircraft stability: static stability and dynamic stability [58].

Static Stability:

An aircraft is said to be statically stable if its initial response to natural disturbances (weather related) counter the disturbance making the aircraft return to its original state. A statically stable aircraft is designed in such a way that aerodynamic forces and moments act in the appropriate directions to return the aircraft to longitudinal and lateral trim [58].

Longitudinal Static Stability

Analysis of longitudinal static stability of a Circulation Control UAV is one of the objectives of this research. Static stability is an important measure that influences the pilots ability to fly an aircraft. Most aircraft are designed to be statically stable, however, many highly dynamic aircraft are statically unstable and difficult to fly without the assistance of an autopilot system [58].

Longitudinal static stability is mostly determined through the location of center of gravity x_{cg} and the aerodynamic neutral point or aerodynamic center point x_{ac}. The aerodynamic neutral point is defined as the point where the pitching moment is constant for a range of angles of attack and the point at which the lift forces act. Both x_{cg} and x_{ac} are measured from the leading edge of an aircraft. These two values are used to define a pa-

rameter known as the static margin which is the difference between x_{cg} and x_{ac} normalized over the mean chord length $\bar{c}$ (Figure 3.6) [58].

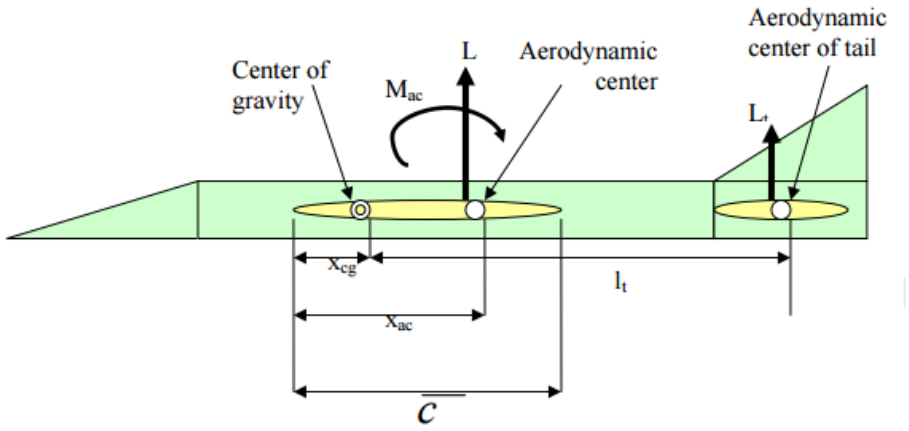

Figure 3.6: Side cross-section view of an aircraft depicting a statically stable aircraft where static margin > 0 [59].

Static margins greater than 0 indicate that the center of gravity is located at the nose of the aircraft and is ahead of the aerodynamic center which implies static stability. However, too large static margins will make the aircraft "nose heavy" and unresponsive to pilot inputs.

Longitudinal static stability can be represented with Pitching Moment Stability derivative (C_m) and AoA. Suppose an aircraft in trim flight experiences turbulences that deviate it from trim AoA. A statically stable aircraft will experience a pitching moment in the opposite direction to AoA that returns the aircraft to trim [58]. The behavior is labeled as positive pitch stiffness and is depicted in curve *a* of Figure 3.7. A statically unstable aircraft on the other hand will experience a pitching moment in the same direction of AoA that deviates the aircraft further from trim. This behavior is labeled as negative pitch stiffness and is depicted in curve *b* of Figure 3.7 [59].

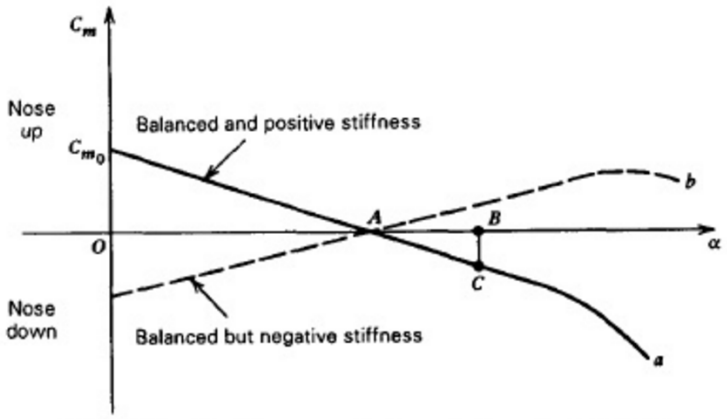

Figure 3.7: C_m Pitching moment of an aircraft about CG [59].

Lateral Static Stability

An aircraft is said to be laterally statically stable if increases in the sideslip angle (β) result in a counter acting yawing moment and side force that restore the aircraft to the original state. This behavior can be labeled positive sideslip stiffness. As in longitudinal stability, lateral static stability can be determined using the rolling moment due to sideslip angle stability derivative (L_β); $L_\beta < 0$ implies lateral static stability [59].

Dynamic Stability

Dynamic stability is defined by the ability of an aircraft to return to trim flight after deviating from it due to pilot inputs. The response of the UAV to the inputs are over-damped and that the amplitude of the resulting oscillatory motion will diverge to trim values without requiring pilot intervention [59].

Longitudinal Dynamic Stability

Longitudinal dynamic stability can be determined through studying the eigenvalues (λ) of Equation (3.1). If $\lambda < 0$ or $Re\{\lambda\} < 0$; the aircraft is dynamically stable. For most aircraft that are designed to be dynamically stable, the eigen values will be two pairs of complex numbers. One pair will have low frequency response and will appear near the origin when plotted on the real and imaginary axis while the other will have long frequency

response and will appear further from the origin (Figure 3.8). These frequency responses are the modes of a dynamically stable aircraft. The low frequency response is called the phugoid mode while the long frequency response is called the short period mode [59].

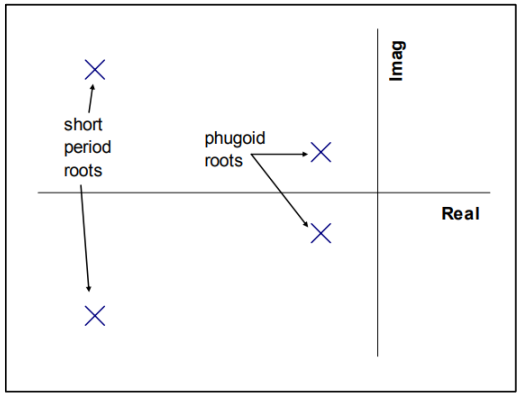

Figure 3.8: The phugoid and short period modes of a dynamically stable aircraft [59].

Lateral Dynamic Stability The lateral dynamic stability can be studied by determining the eigen values of Equation (3.2). A laterally stable aircraft has three lateral modes (Figure 3.9); i) The Spiral mode: is the tendency of an aircraft to roll while in trim flight causing a downward spiral motion; ii) The Dutch Roll mode: is a coupled yawing and rolling mode that causes an oscillatory motion around trim (Figure 3.10); and iii) The Roll mode: is caused by aileron inputs.

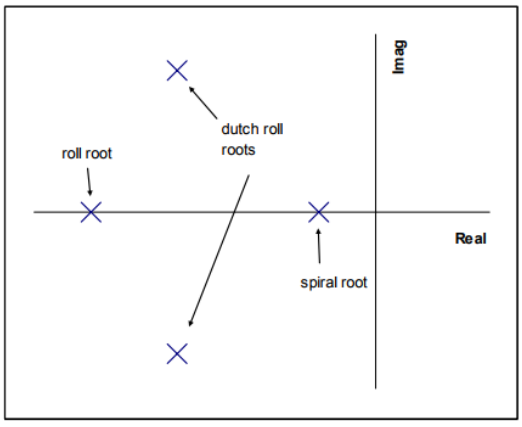

Figure 3.9: The lateral dynamic modes [59].

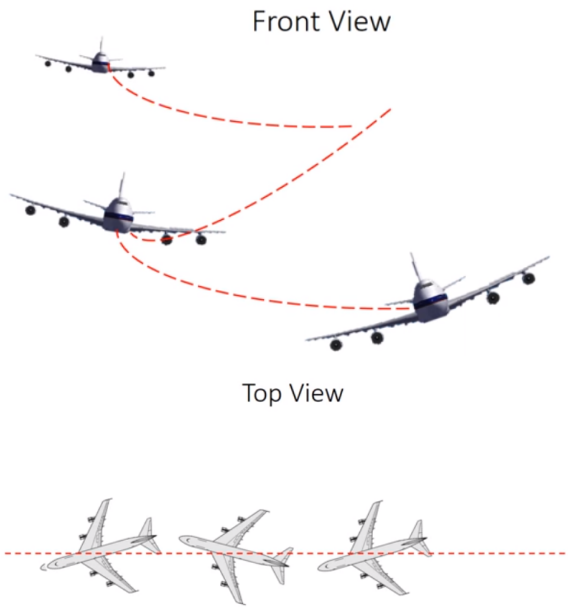

Figure 3.10: Front and top views of the Dutch Roll mode showcasing the rolling and yawing moments [58].

3.3.2 Circulation Control Dynamics

Little is known about the effects of Circulation Control on the dynamics of an aircraft. Research shows the introduction of a nose down pitching moment [60]. Experiments performed at DU^{2}SRI have proven the pitching moment effect of CC (Figure 3.11) . To showcase this effect, the UC^{2}AV is flown in trim conditions when CC is turned on. Two vital observations are made, i) a nose down pitching moment effect, and; ii) no significant effects in the lateral dynamics.

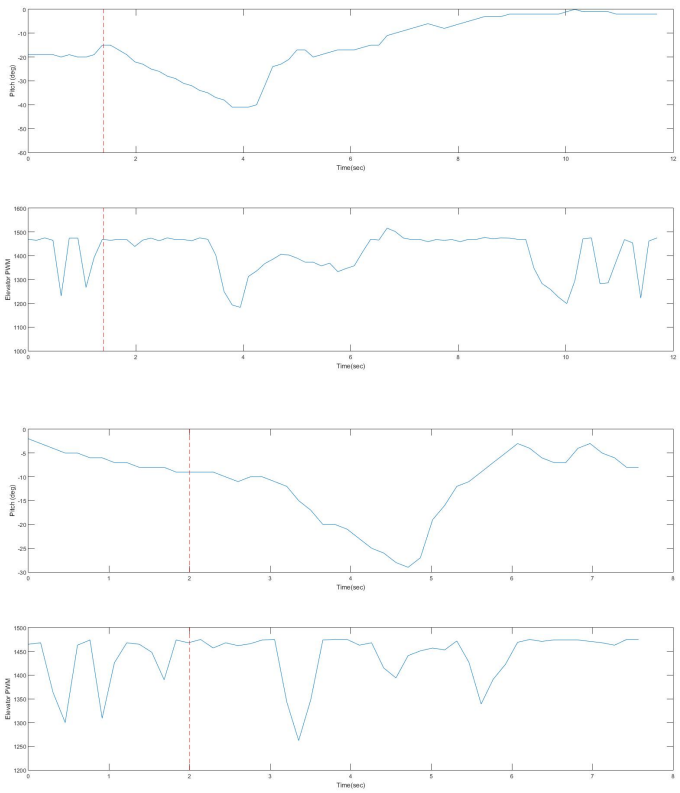

Figure 3.11: CC is turned on at time = 1.5s (top) and at 2s (bottom) while the remaining control surfaces are in trim conditions. The UC^{2}AV experiences a pitch down moment until the pilot manually recovers it by applying an elevator input and turning CC-off.

Initial flight tests indicate that CC causes a nose down pitching moment effect. Weather conditions and forces introduced by the centrifugal compressor on-board and pilot's inputs, might also effect UAV's behavior. It can be concluded that of the three moments the UC^{2}AV experiences (L, M, N), only the longitudinal moment M is affected by CC. Therefore, the pitching moment effect can be studied by analyzing the longitudinal dynamics. More specifically, it can be studied by analyzing the dimensional stability and control derivatives that the pitching moment (M) is dependent upon.

3.4 System Identification Methodology

This section presents the system identification algorithm implemented in this thesis. It begins by presenting an overview of the method of approach explaining the requirements placed on the input signals designed to excite system dynamics, the system identification algorithm, and the model verification performed to analyze model accuracy. The section then presents the simulation testing environment setup and concludes by presenting the avionics system, signal processing procedures, and the limitations that arise during flight testing.

3.4.1 Method Overview

System identification is performed on the baseline RMRC Anaconda UAV and the modified UC^{2}AV (CC-off and CC-on) in simulation environment (X-Plane Flight Simulation Software) and with flight testing (Figure 3.12). Simulation system identification is performed to verify the proposed method and obtain simulation-based mathematical models of the UAVs. Flight tests are held to perform system identification using real flight data to identify mathematical models that capture CC dynamics (since CC dynamics cannot be simulated in the flight simulation software) and to allow comparison with the simulation models. The CC-off and CC-on mathematical models are used to determine the effects of CC on the UAV dynamics.

Derivation of the mathematical models of the UAVs is done in three steps, Data Collection, System Identification, and Model Verification. Frequency sweep (chirp) signals are applied to the aircraft's control surfaces (elevator, aileron, and throttle) to excite system dynamics. Throttle is maintained at 60% of full power while elevator and aileron sweeps are performed. The applied inputs and UAV response to the inputs are recorded and used for system identification. CIFER, which is a system identification software package based

on frequency domain methods, is used for performing system identification. The mathematical models are obtained by examining the response of the aircraft to frequency sweep inputs. Doublet inputs are applied to the control surfaces individually and the response of the aircraft is recorded. Verification of the models is done by comparing the response of the aircraft to doublet inputs to the response of the mathematical models to identical doublet inputs. Root mean square error and Theil Inequality Coefficient (TIC), which is a parameter used to identify the predictive ability of the models, calculations are performed to analyze the accuracy of the models.

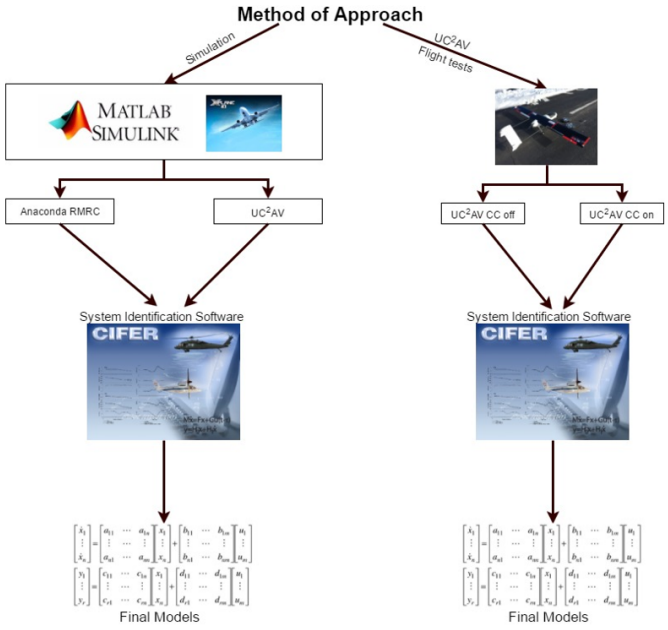

Figure 3.12: Breakdown of the method of approach.

Frequency Sweep and Doublet Inputs

Frequency sweep inputs are applied to the control surfaces of the UAVs to capture the aerodynamic characteristics. The frequency sweeps must excite the dynamics in the frequency range of interest. The frequency range is defined as [53]:

$$0.5w_{bandwidth} < w < 2.5w_{180} \tag{3.3}$$

A pilot performs the sweeps following the provided guidelines below. The guidelines are designed to produce high quality frequency sweeps that can derive accurate models [53] (Figure 3.13):

- Frequency sweeps are implemented on control surface individually (on axis) while maintaining the remaining surfaces (off axis) in trim conditions. This guarantees that the response is due to the input applied to the sweeping surface and that there is minimum correlation with the other control surfaces.

- The aircraft response must be roughly symmetric with the trim conditions. Weather conditions and the UAV's aerodynamic characteristics might lead the aircraft to drift preventing symmetric responses. This is compensated for by applying pulse inputs on the off axes correcting the drift.

- The sweeps begin and end in approximately 3 seconds of trim flight.

- After the first 3 seconds of flight in trim conditions, two frequency sweeps are performed at the lowest frequency of interest.

- The frequency of the sweeps gradually increases to the highest frequency of interest. Afterwards, a 3 second flight in trim conditions is performed.

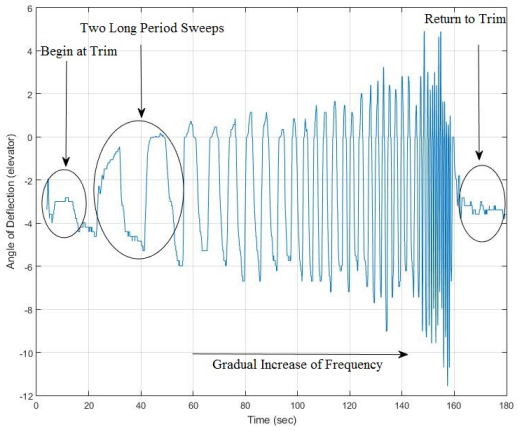

Figure 3.13: Frequency sweep signal implemented on the elevator.

The total record length of each sweep is $4.5T_{max}$(where $T_{max} = \frac{1}{f_{min}}$ is defined by Equation (3.3)). The sweeps are performed three times for each control surface. This guarantees sufficient data for system identification. The magnitude of control surface input is within $\pm 20 - 30\%$ of maximum surface deflection. This guarantees that the response is within the range defined by the small perturbation theorem and hence is decoupled and linear. The angular response of the longitudinal dynamics is within $\pm 20°$. Doublet input signals are applied on each control surface individually for model verification. The response of the mathematical models to the doublet inputs are compared to the response of the UAVs to the same input.

Data Collection

The data required for system identification is acquired by applying sweep and doublet inputs on the elevator, aileron, and throttle control surfaces and by recording the response of the aircraft to the inputs. The pitch angle θ, pitch rate of change q, forward velocity u, and vertical velocity w response of the UAVs are recorded for longitudinal model identification. The roll ϕ, roll rate p, yaw rate r, and lateral velocity v are recorded for lateral model identification.

To collect the data necessary for simulation system identification, a Simulink code is written to communicate with X-Plane software (Section 3.4.2). Whereas an avionics system is developed for real-time data logging of flight tests (Section 3.4.3)

System Identification

The longitudinal and lateral models shown in Equation (3.1 and 3.2) are identified for both aircraft along with the stability and control derivatives using CIFER. To reduce identification error, the data collected is segmented to 5 overlapping Hanning windows. The minimum window size for the lower frequency dynamics is 3 seconds while the minimum size for the higher frequencies is 15 seconds. These are found using the guidelines derived by Tischler [53]. The guidelines are presented here:

For the lower frequencies, $T = 5/(\zeta * \omega_{max})$ and higher frequencies $T = 60 * \pi/\omega_{max}$

CIFER performs chirp z-transform frequency domain analysis conditioning of the result to multiple inputs (off axis) present during the sweeps and optimizing the results across the multiple spectral windows and calculates a frequency-response. The frequency-response is used to calculate a coherence function (γ^2_{xy}), which is given by Equation (3.4), that is an indication of the fraction of output spectrum that is linearly related to the input spectrum. The coherence function is used as a measure to determine the quality of the sweep signals. Low coherence values are an indication that the response of aircraft are not due to the input sweep signals but other parameters such as non-linear system dynamics and wind gusts. Tischler has shown, through experimental studies, that coherence values $>$ 0.6 yield accurate models [53].

$$\gamma_{xy}^2 = \frac{|G_{xy}(f)|^2}{|G_{xx}(f)||G_{yy}(f)|} \tag{3.4}$$

Where $G_{xx}(f)$,$G_{yy}(f)$,and $G_{xy}(f)$ are the input spectral function, output spectral function, and cross spectral function receptively. They are represented as:

$$\begin{cases} G_{xx}(f) = \dfrac{2}{T} \times X(f)^2 \\ G_{yy}(f) = \frac{2}{T} \times Y(f)^2 \\ G_{xy}(f) = \dfrac{2}{T} \times X(f) \times Y(f) \end{cases} \tag{3.5}$$

A coherence value is calculated for each frequency sweep. Frequency response analysis is completed once every coherence value is greater than 0.6.

CIFER implements an optimization algorithm that minimizes the error between the magnitude and phase of the model to be identified and of the calculated frequency-response of the recorded data. The primary outcome is identification of matrices A and B appearing in Equations (3.1 and 3.2) that produce the frequency response matrix $T(s)$ that matches the frequency response of flight data $\hat{T}_c$. A quadratic cost function is defined and minimized for every transfer function n_{TF}. Tischler determined experimentally that average cost values less than 100 with no individual cost value exceeding 200 yield accurate models [53]. The standard cost function is:

$$J = \sum_{l=1}^{n_{TF}} \left(\frac{20}{n_\omega} \times \sum_{\omega_1}^{\omega_{n_\omega}} W_\gamma [W_g(|\hat{T}_c| - |T|)^2 + W_p(\angle\hat{T}_c - \angle T)^2] \right)_l \tag{3.6}$$

Three weights are presented in the cost function. These are:

- W_γ: Is a coherence weighting function. It is implemented to place more value in frequency response ranges where the coherence is high. It is defined as $W_\gamma = [1.58(1 - e^{-\gamma_{xy}^2})]^2$
- W_g and W_p are magnitude and phase weights. By convention, these are set to $W_g = 1$ and $W_p = 0.01745$ [53].

CIFER's DERVID function is used to identify state-spaces models of the aircraft. In addition to cost values, which are used as an indication of how well the model fits the frequency response of the data, two additional parameters are provided (Equation (3.7)). These are the Cramér-Rao bound calculations, which are the minimum expected standard deviation of an estimated parameter and are used for accuracy analysis, and insensitivity percentage, which indicates the effect of a parameter on the cost values. A high insensitivity percentage indicates that a parameter has little effect on the cost values. Tischler determined that Cramér-Rao bounds and percentages and insensitivity percentages that are within the following standards yield accurate models [53]:

- Cramér-Rao bound and $CR\% \leq 20\%$
- Insensitivity $I \leq 10\%$

$$\begin{aligned} CR_i &= \sqrt{(H^{-1})_{ii}} \\ where \quad H &= \frac{\delta J}{\delta\Theta\delta\Theta^T} \\ I_i &= \frac{1}{\sqrt{H_{ii}}} \end{aligned} \tag{3.7}$$

Parameters with insensitivity percentages greater than 10% are eliminated from the model following the steps shown in Figure 3.14.

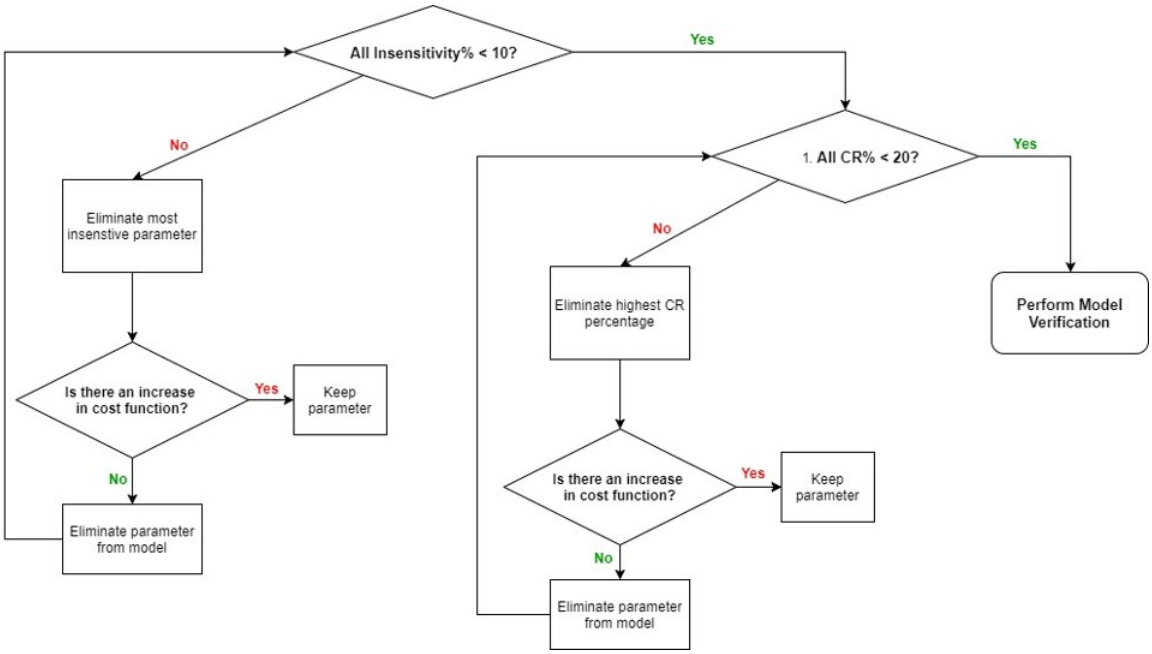

Figure 3.14: The process of eliminating stability and control derivatives with large CR and insensitivity percentages.

A final overview of the system identification process is shown in Figure 3.15.

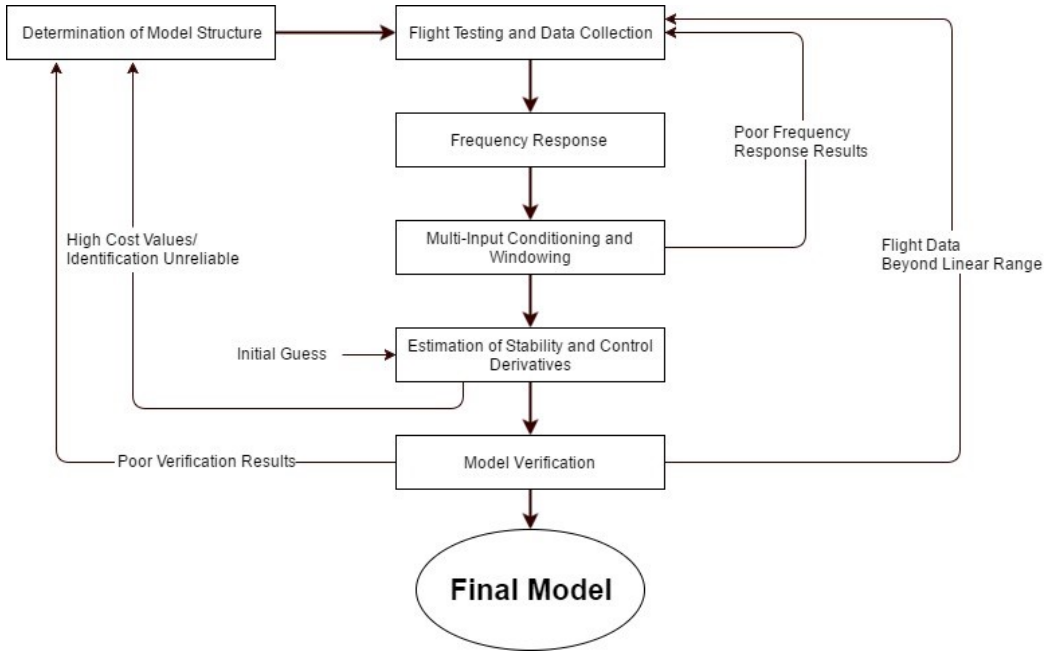

Figure 3.15: An overview of the system identification procedure indicating the CIFER algorithm.

Model Verification

Doublet input signals are applied to the control surfaces of the aircraft. The models obtained with the DERVID function are verified using CIFER's VERIFY function. The step input applied to the elevator surface is provided as an input to the model while throttle is kept constant. The response of the UAV and the output of the models are compared. The comparison is used as verification of the model. Prior to performing the comparison, CIFER estimates and corrects any biases or reference shifts that account for untrimmed reference flight, unaccounted for secondary control inputs, or weather related disturbances. Once these are calculated, the root mean square J_{rms} of the model response and flight data is calculated. Along with J_{rms}, CIFER provides calculations for the Theil inequality coefficient (TIC) which a normalized criterion used to assess the predictive ability of a model (Equation (3.8)). TIC = 0 indicates that the model has perfect predictive capability while TIC = 1 means the model has no predictive capability. As a standard, $J_{rms} \leq 0.5$ to 1.0 and TIC ≤ 0.25 to 0.30 are considered acceptable [53].

$$TIC = \frac{\sqrt{[1/n_t n_0] \sum_{i=1}^{n} [(y_{data} - y)^T W (y_{data} - y)]}}{\sqrt{[1/n_t n_0] \sum_{i=1}^{n_t} [y^T W y]} + \sqrt{[1/n_t n_0] \sum_{i=1}^{n_t} [y_{data}^T W y_{data}]}} \tag{3.8}$$

3.4.2 Implementation in Simulation Environment

X-Plane models of the RMRC Anaconda and UC^{2}AV are created using JavaFoil, Airfoil Maker, and Plane Maker (Figure 3.17). JavaFoil is used to model the airfoil aerodynamic properties and dimensions at the appropriate Reynold's number. The UC^{2}AV airfoil properties can be found in [10]. Segmenting the RMRC Anaconda wing and measuring the airfoil dimensions (maximum thickness location) revealed that the RMRC Anaconda has a Clark YH airfoil (Figure 3.16). The modeled airfoils are converted to X-Plane using X-Plane's airfoil Maker. Plane Maker is used to model the weight and dimensions of the UAV parts

(fuselage, wings, landing gear...etc.), the location of center of gravity, motor specifications (horse power, maximum rpm...etc.), and control surface dimensions (control surface width, maximum deflection angles, location on wings...etc.).

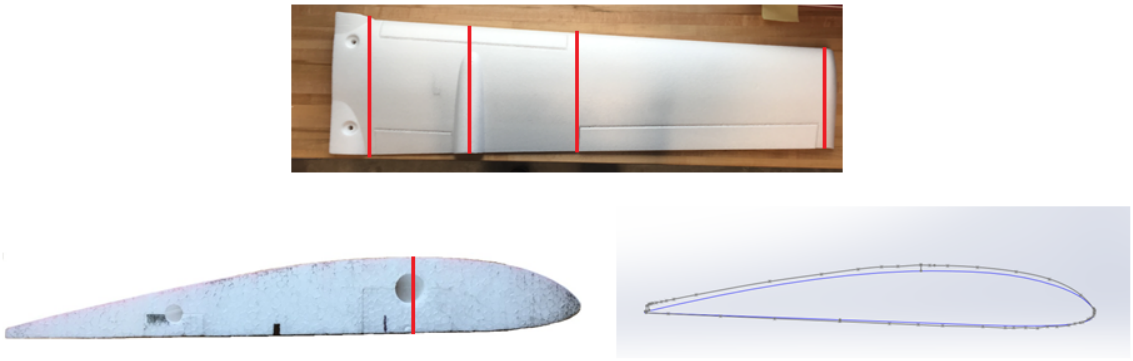

Figure 3.16: Top: the wing is segmented to five pieces to analyze airfoil properties. Bottom left: an airfoil segment shows the location of maximum airfoil thickness. Bottom right: Clark YH airfoil (maximum thickness = 11.9%) has the best match with the RMRC Anaconda airfoil (maximum thickness = 12.2%).

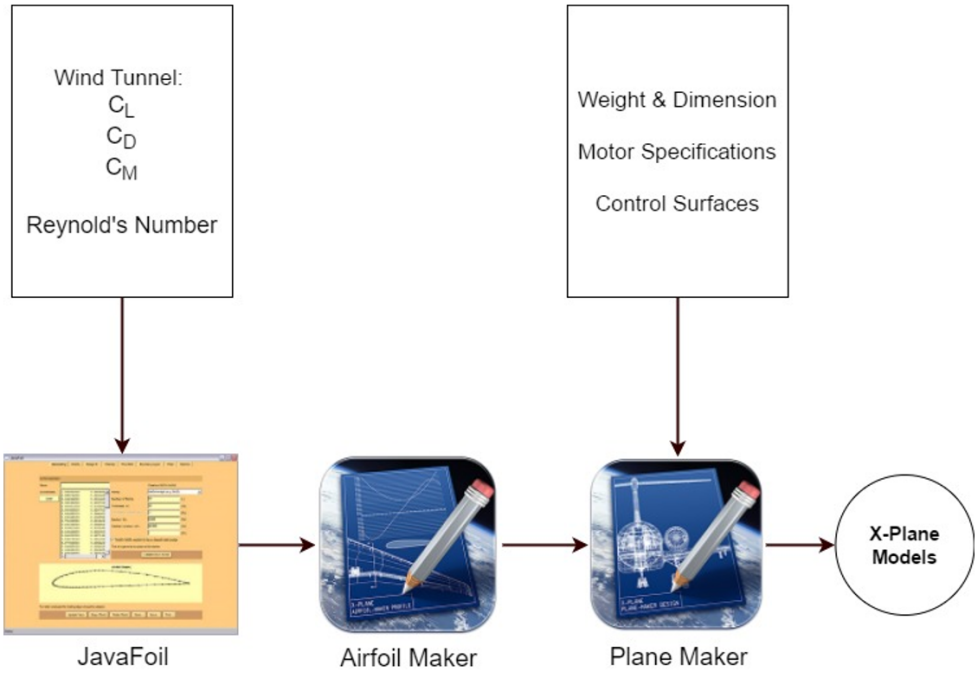

Figure 3.17: Steps for creating UAV X-Plane models. The coefficients of lift C_L, drag D_D, and moment C_M are modeled by X-Plane

A Simulink code is written to communicate with X-Plane via UDP protocol. The data generated by X-Plane (pilot inputs and UAV response) is packeted and sent to Simulink. The packeted data is in decimal code and single precision floating point format (Figure 3.18). The Simulink code unpacks and converts the data to decimal values [61]. The values are also plotted in real-time to provide immediate pilot feedback (Figure 3.19). It is important to note that Simulink's simulation time is dependent on the complexity of the code and the speed of computer. The time array produced by Simulink can be inaccurate leading to incorrect data time stamping. To resolve the issue, tic and toc Matlab functions are used.

Figure 3.18: A UDP packet sent by X-Plane to Simulink. Bytes 1-4 contain the Header, byte 5 is a software internal use byte, bytes 6-10 contain the data label, and bytes 11-41 contain the estimated aerodynamic variables.

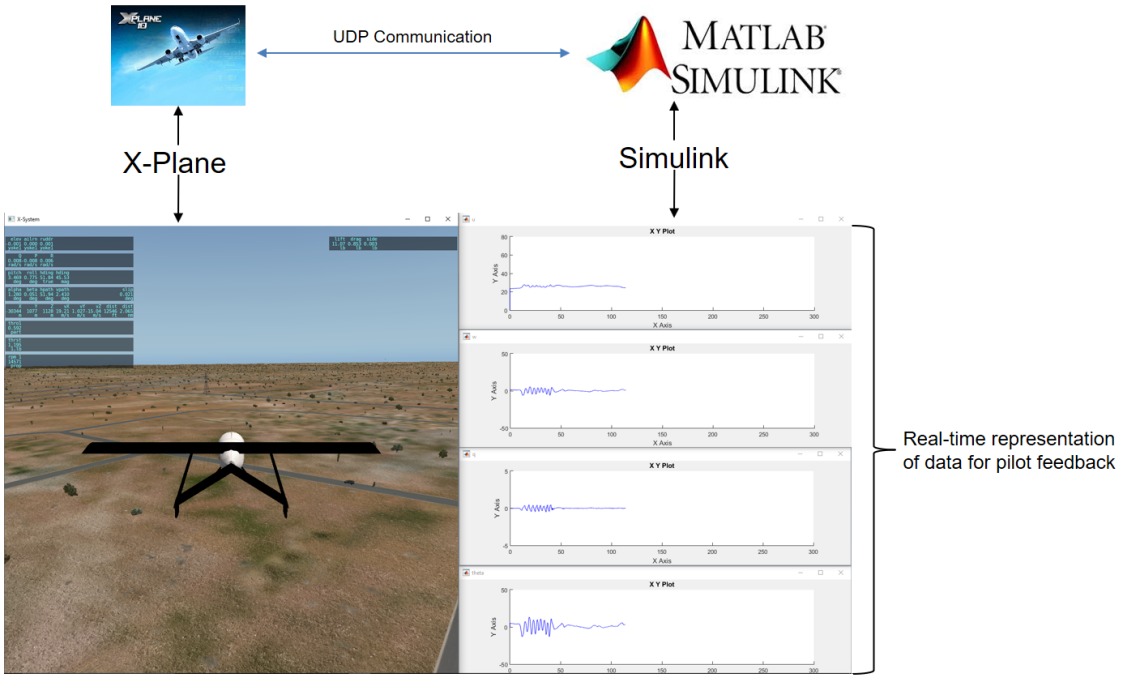

Figure 3.19: Real-time visualization of the recorded data.

The designed frequency sweeps used for system identification and doublet input signals used for model verification are applied to the aircraft using the Interlink Elite Controller. Sweep inputs and UAV response to the inputs are recorded using Simulink and Matlab. The recorded data is imported to CIFER for system identification. Doublet inputs and UAV response to the inputs are recorded and imported to CIFER for model verification (Figure 3.20).

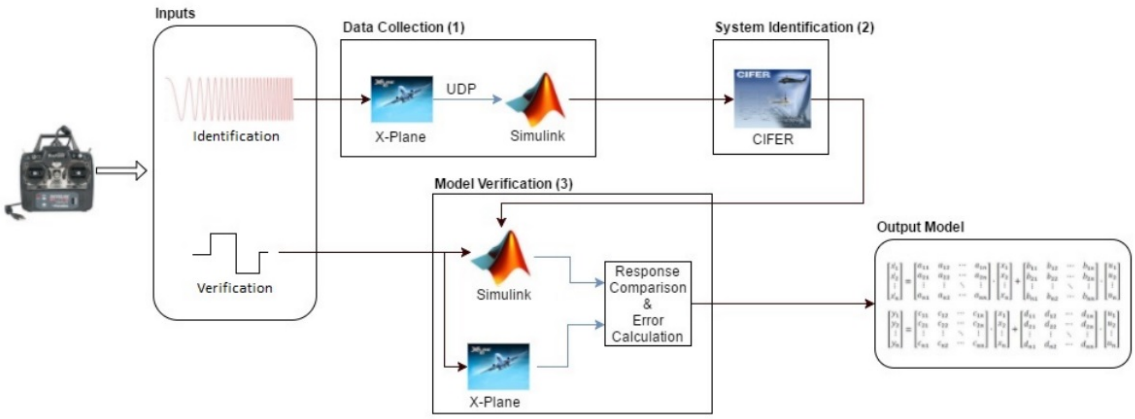

Figure 3.20: The simulation method of approach.

3.4.3 Implementation on Aircraft and Flight Testing

Avionic System

An avionic system is setup for data collection during flight testing (Figure 3.21). A trained pilot is stationed on the ground and controls the UAV through an RC transmitter. The sensory system includes an IMU that records the aerodynamic angles and linear accelerations, a GPS unit that records latitude, longitude and altitude coordinates, and a pitot tube that measures air speed. The data recorded by the sensors is transmitted to Arduino microcontrollers and stored on an on-board SD card. The pilot inputs are also sent to an Xbee transmitter for real-time plotting. The pilot PWM inputs are transmitted to another

Xbee sensor on the ground. An Arduino Mega is used to parse the incoming pilot input data and plot it on a laptop.

The pilot performs the sweep maneuvers at discrete frequency values four times. This guarantees sufficient data for system identification. Signal processing analysis reveals the quality of the sweeps and the best sweep maneuvers are selected from the four datasets for each frequency value. The flight engineer is stationed by the ground control station (GCS) and provides the pilot with real-time feedback by examining the data presented on the GCS.

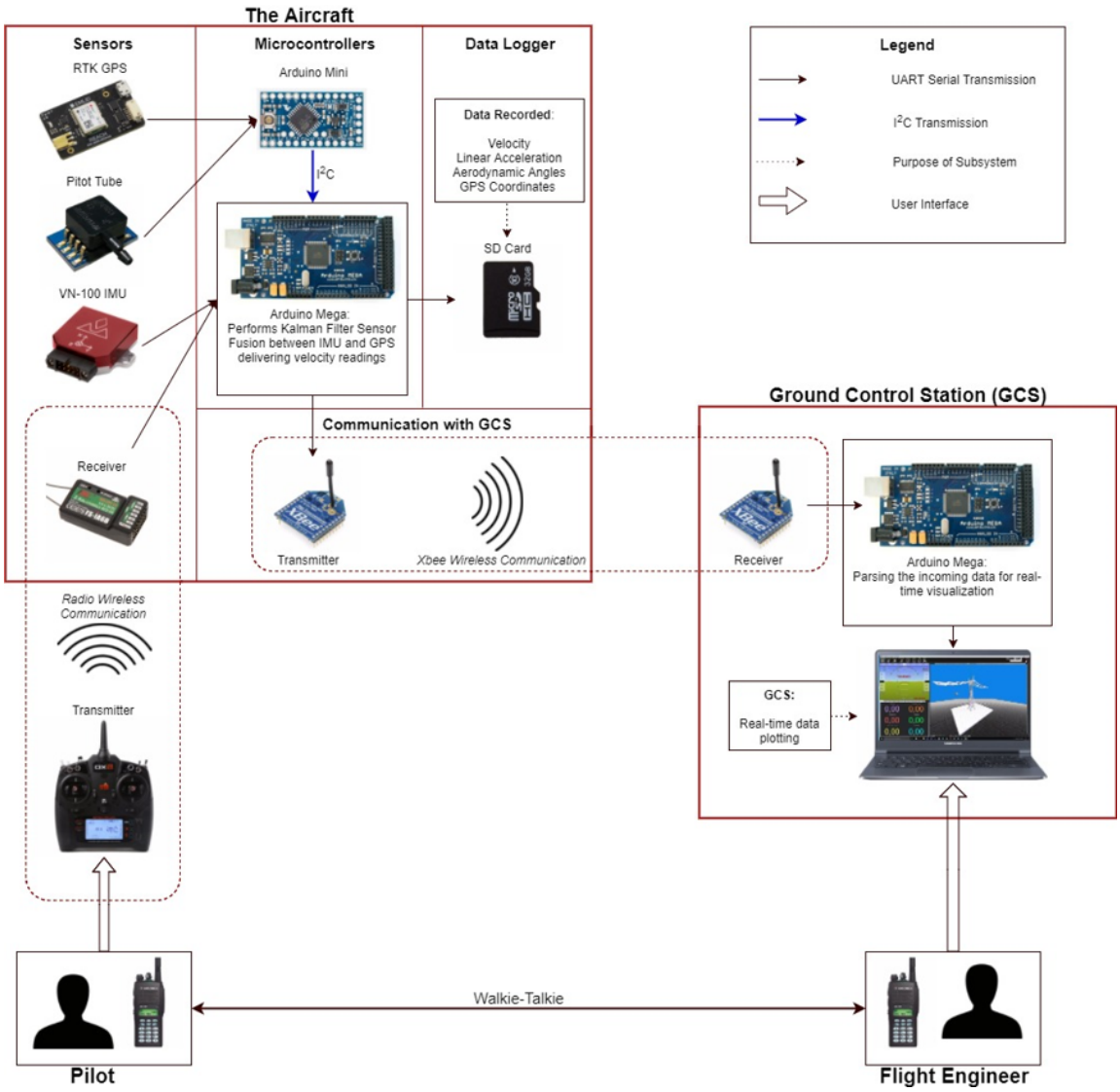

Figure 3.21: The avionic system on board the UAVs.

Signal Processing

In order to capture the models shown in Equations (3.1 and 3.2), all the variables presented in the models need to be recorded during flight data. Table 3.3 summarizes the signal processing procedure for each sensor. It is worth noting that the VN-100 IMU is incapable of capturing highly dynamic lateral maneuvers without implementation of sensor fusion algorithm. An upgrade in the IMU and the GPS sensors should improve the quality of the captured data.

Table 3.3: The sensory system.

Unit	Sensor	Sampling Frequency	Data Recorded	Signal Processing
GPS	3D Robotics	5 Hz	Latitude, longitude, and altitude	Data is convereted to UTM coordinates, then to body axis frame. Linear velocity of the UAV is calculated in the body axis frame. Sensor fusion is performed with IMU readings.
Pitot Tube	DIY drones	5 Hz	Airspeed	Calculated of forward velocity. Used as a reference for sensor fusion algorithm.
IMU	VN-100	100 Hz	Aerodynamic angles and linear accelerations	Aerodynamic angles are recorded. Linear accelerations are referenced to the body frame and are used in sensor fusion with GPS readings.
RC Receiver	Spectrum	20 Hz	PWM Inputs	Inputs are upsampled to 50 Hz.

Equation (3.9) show the process of converting latitude (ϕ), longitude (λ), and altitude (h) to earth reference frame velocities (u_{nv}, v_{nv}, and w_{nv}). For more detail on the conversion parameters and their derivation, see [62]. The estimated velocity values are then converted to the body reference frame using the rotational matrix shown in Equation (3.10).

$$
\begin{aligned}
R_{Ea} &= 6,378,137.0\ m \\
f &= \frac{1}{298.257223563} \\
R_{Eb} &= R_{Ea}(1-f) \\
e &= \frac{\sqrt{R_{Ea}^2 - R_{Eb}^2}}{R_{Ea}} = 0.08181919 \\
M_E &= \frac{R_{Ea}(1-e^2)}{(1-e^2 sin^2\phi)^{(3/2)}} \\
N_E &= \frac{R_{Ea}}{\sqrt{1-e^2 sin^2\phi}} \\
v_{nv} &= \dot{\lambda}(N_E + h)cos\phi \\
u_{nv} &= \dot{\phi}(M_E + h) \\
w_{nv} &= -\dot{h}
\end{aligned}
\tag{3.9}
$$

$$
R_{b/nv} = \begin{bmatrix} c_\theta c_\psi & c_\theta s_\psi & -s_\theta \\ s_\phi s_\theta c_\psi - c_\phi s_\psi & s_\phi s_\theta s_\psi + c_\phi c_\psi & s_\phi c_\theta \\ c_\phi s_\theta c_\psi + s_\phi s_\psi & c_\phi s_\theta s_\psi - s_\phi c_\psi & c_\phi c_\theta \end{bmatrix} \tag{3.10}
$$

In order to improve the accuracy of the velocity readings, the calculated GPS values are fused with the IMU accelerometer readings. Since the accelerometer readings are not free of signal noise, integrating acceleration readings will only yield accurate velocity values for roughly 2 seconds. The noise present in the readings will cause integration error build up making the velocity values diverge with time (Figure 3.22). There is little change in altitude and lateral position of the UAV at high frequency sweeps maneuvers. Examination of the data has shown that the GPS resolution is not sufficient to estimate UAV velocity in such scenarios. A Kalman filter sensor fusion algorithm is implemented to overcome these issues (Figure 3.23).

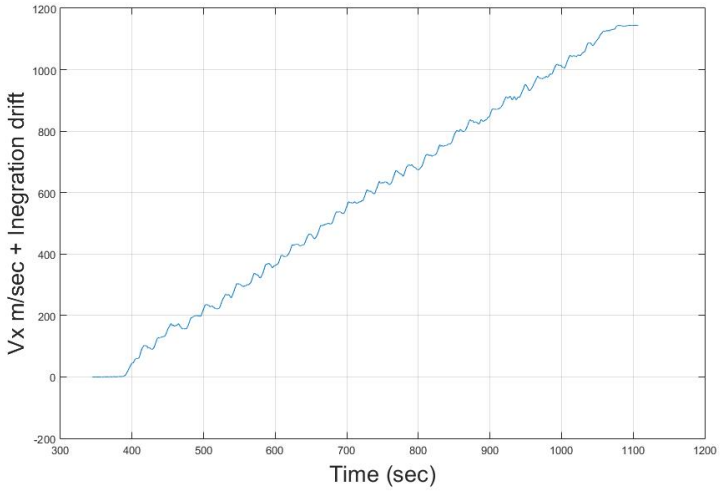

Figure 3.22: Integration of acceleration readings will result in integration drift making the velocity readings incorrect.

The sensor fusion algorithm combines the velocity readings obtained from GPS calculations Equation (3.9) and the IMU accelerometer using Kalman filter equations (Equation (3.12)). The Kalman filter equations include a gain variable K. It can be seen from examining Equation (3.12) that setting $K = 0$ will result velocity calculation using IMU accelerometer data alone. Setting $K = 1$ will result in velocity calculation using GPS data alone. The implemented algorithm sets $K = 1$ every 0.2 seconds (GPS sampling frequency). This resolves integration drift issues. The algorithm also fuses the IMU readings with the linearly interpolated GPS readings for frequencies $>$ 5 Hz. The gain values are calculated using Equation (3.11).

$$\begin{aligned} K_k &= P_k^+ R_K^{-1} \\ P_k^+ &= (I - K_k) P_k^- \end{aligned} \tag{3.11}$$

$$
\begin{aligned}
\hat{v^+_{x_k}} &= \hat{\Delta ta^-_{x_{k-1}}} + \hat{v^+_{x_{k-1}}} + K_k[u_{GPS} - \hat{\Delta ta^-_{x_{k-1}}} - \hat{v^+_{x_{k-1}}}] \\
\hat{v^+_{y_k}} &= \hat{\Delta ta^-_{y_{k-1}}} + \hat{v^+_{y_{k-1}}} + K_k[v_{GPS} - \hat{\Delta ta^-_{y_{k-1}}} - \hat{v^+_{y_{k-1}}}] \\
\hat{v^+_{z_k}} &= \hat{\Delta ta^-_{z_{k-1}}} + \hat{v^+_{z_{k-1}}} + K_k[w_{GPS} - \hat{\Delta ta^-_{z_{k-1}}} - \hat{v^+_{z_{k-1}}}]
\end{aligned}
\tag{3.12}
$$

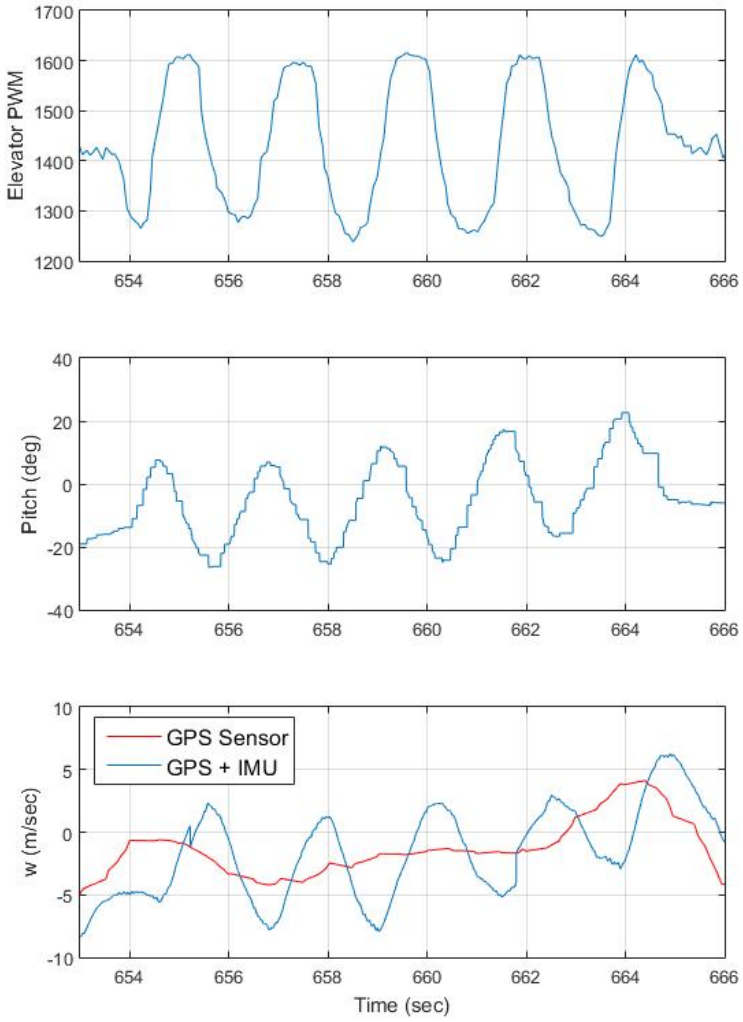

Figure 3.23: An elevator sweep example shows that the GPS is incapable of capturing the vertical velocity w without sensor fusion due to poor resolution.

Flight Testing Frequency Range

The guidelines shown in Figure 3.13 and discussed in Section 3.4.1 need to be followed to guarantee accurate system identification. The guidelines state that the sweeps must begin with 3 seconds trim flight, include two long period sweeps, linearly increase frequency, and end in 3 second trim flight (Figure 3.13). CIFER also requires persistent excitation of the UAV dynamics to guarantee sufficient data for system identification. Time history files with a record length equal or greater than $5 \times T_{max}$, where T_{max} is the period of the minimum frequency of interest, are said to be persistently excited. These guidelines can be easily followed in simulation environments. However, due to limited radio communication range, a maximum of 20 seconds of level flight can be achieved by the pilot. Given the trim flight and CIFER's persistent excitation requirements, the minimum identifiable frequency is roughly $\frac{1}{\frac{14}{5}} = 0.35$ Hz.

Chapter 4

Simulation Results and Analysis

This chapter presents the mathematical models obtained through system identification of X-Plane flight simulation software models. Longitudinal and lateral models of the RMRC Anaconda and the UC^{2}AV (CC-off) are presented. Verification experiments are held to test the predictive ability and accuracy of the derived models

4.1 RMRC Anaconda Aircraft

The longitudinal model is identified by applying elevator sweeps and capturing the forward velocity (u), vertical velocity (w), pitch angle (θ), and pitch rate of change (q) responses. The lateral model is identified by applying aileron sweeps and capturing the lateral velocity (v), roll rate of change (p), and roll angle (ϕ). The yaw rate of change variable (r) seen in Equation (3.2) was omitted from the lateral model as rudder input sweeps are required to capture the yaw dynamics.

4.1.1 Longitudinal Model

Simulation Model Derivation

Following the guidelines presented in Section 3.4.1, frequency sweep inputs are applied to the elevator (Figure 4.1) while the throttle is maintained at 60% of full power. Aileron inputs are limited to small pulse inputs that guarantee decoupling of UAV dynamics. The frequency range of the sweep inputs is approximately between 0.05 Hz to 1.2 Hz. The aircraft's forward velocity (u), vertical velocity (w), pitch rate (q), and pitch (θ) are recorded (Figure 4.2).

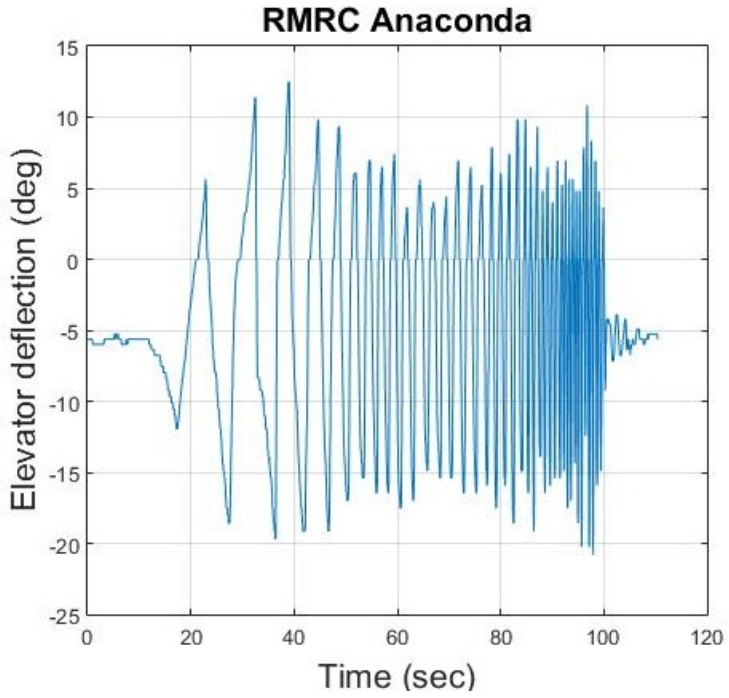

Figure 4.1: Elevator sweep signal applied to excite UAV dynamics.

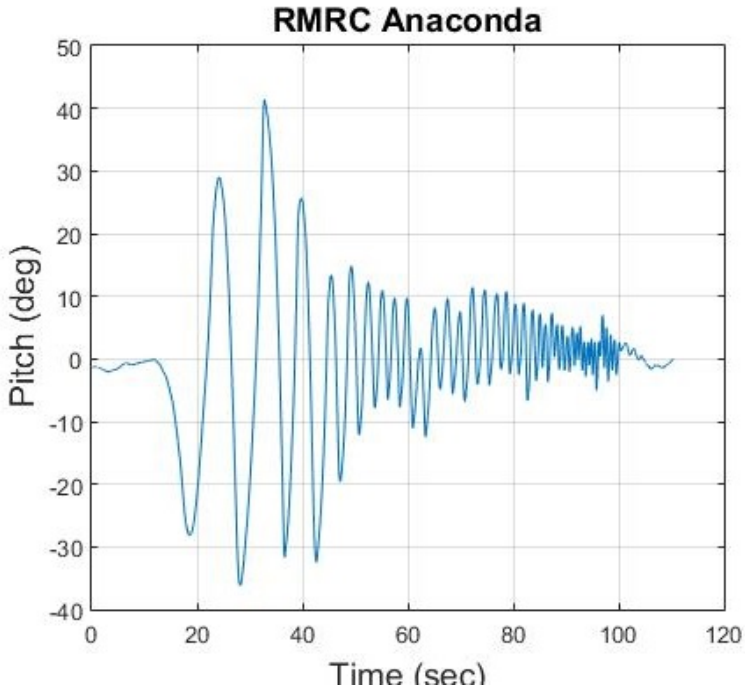

Figure 4.2: Pitch angle response to the elevator sweep.

CIFER is used to convert the data from the time domain to the frequency domain by performing chirp z-transform and then calculate a coherence function for every identified parameter (Equation (3.4)), perform multiple input conditioning to account for aileron inputs, and perform data windowing to reduce error. Coherence values greater than 0.6 are required to obtain accurate models [53]. Table 4.1 and Figure 4.3 highlight the frequency ranges that possess coherence ranges > 0.6.

Table 4.1: Frequency ranges of model variables with acceptable coherence values.

	RMRC Anaconda (Hz)
u	0.05-0.17
w	entire range
q	entire range
θ	entire range

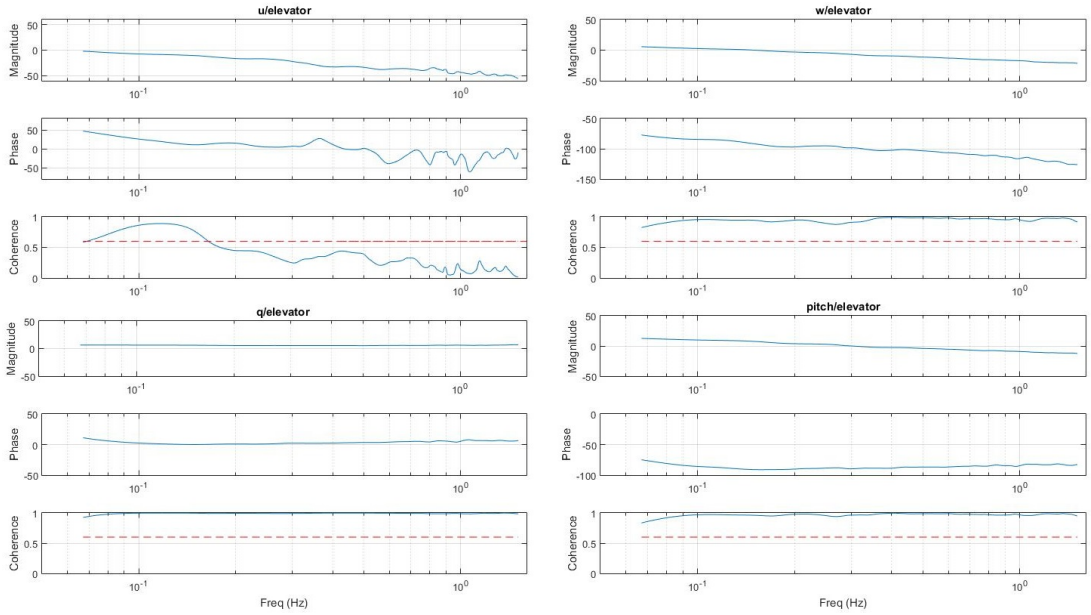

Figure 4.3: Magnitude, phase, and coherence plots for every identified variable of the simulation RMRC Anaconda.

The coherence values are greater than 0.6 for the entire frequency range of every identified parameter with the exception of u. Low coherence for u is expected at higher frequencies as u remains constant while performing elevator sweeps. This indicates a lack of correlation between elevator control surface and u at high frequencies. However, there still exist sufficient data to model u at lower frequencies.

CIFER's DERVID function is used next to identify the dynamic models. To do so, the longitudinal model structure presented in Equation (3.1) is chosen for identification. However, the model in Equation (3.1) is decomposed to the canonical form (Equation 4.1). The canonical form is desired as it allows the direct identification of the stability and control derivatives by factoring the known mass and inertia variables out of the mathematical models.

$$M\dot{x} = Fx + Gu \tag{4.1}$$

In Equation (4.1), M is the inertial matrix of longitudinal dynamics, x is the state variables matrix $x = [u\ w\ q\ \theta]^T$, and u is the input matrix. Matrix F contains the stability derivatives and matrix G contains the control derivatives. Matrices M, F and G are defined as:

$$M = \begin{bmatrix} m & 0 & 0 & 0 \\ 0 & m & 0 & 0 \\ 0 & 0 & I_y & 0 \\ 0 & 0 & 0 & 1 \end{bmatrix}, F = \begin{bmatrix} X_u & X_w & X_q & -gcos(\theta_0) \\ Z_u & Z_w & Z_q & -gsin(\theta_0) \\ M_u & M_w & M_q & 0 \\ 0 & 0 & 1 & 0 \end{bmatrix}, G = \begin{bmatrix} X_{\delta_e} \\ Z_{\delta_e} \\ M_{\delta_e} \\ 0 \end{bmatrix} \quad (4.2)$$

For accurate model identification, initial values of the stability derivatives are provided to CIFER. Initial values of the stability derivatives can be determined by calculating the natural damping frequency and damping ratio of the phugoid and the short period dynamic modes. The phugoid mode is a low frequency stable lightly damped longitudinal UAV dynamic mode while the short period mode is a high frequency heavily damped longitudinal UAV dynamic mode (see Section 3.3.1). Applying a step input to the elevator results in a lightly damped oscillatory UAV motion (phugoid mode) while applying an impulse input results in a heavily damped oscillatory motion (short period mode) (Figure 4.4). Calculation of the period and logarithmic decrement (δ) of the oscillatory motion is used to identify the natural frequency (ω_n) and damping ratio (ζ) of the UAV (Equation (4.3)).

$$\delta = \frac{1}{n} ln \frac{x(t)}{x(t+nT)} \quad \zeta = \frac{1}{\sqrt{1 + (\frac{2\pi}{\delta})^2}} \quad \omega_n = \frac{\frac{2\pi}{T}}{\sqrt{1-\zeta^2}} \quad (4.3)$$

where $x(t)$ is the signal amplitude at time t and $x(t + nT)$ is the amplitude after n periods ($n \leq$ number of peaks).

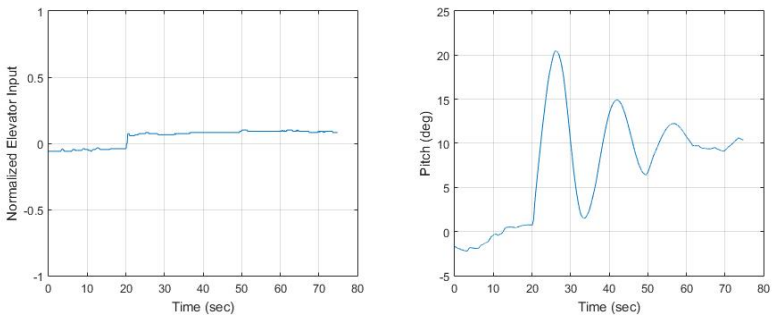

Figure 4.4: The phugoid mode can be simulated by applying elevator step input.

CIFER's numeric optimization algorithm tunes the initial guesses by minimizing the cost function J (Equation (3.6)) and arrives at the final values (Table 4.3). Table 4.2 indicates that all cost values are within the accepted standards discussed in Section 3.4.1. In addition to cost value analysis, Cramér Rao percentage and bound, and insensitivity analysis are performed to further validate the derived stability and control derivatives. Table (4.3) indicates that all parameters except u meet the standards discussed in chapter three (Insensitivity ≤ 10 and CR ≤ 20). This is likely due to the low coherence values at high frequencies, which limit the amount of data available for system identification. Table 4.3 also shows M_w and $M_q \leq 0$, which implies static stability (Section 3.3.1).

Table 4.2: Cost values after CIFER optimization.

	RMRC Anaconda
u	36.950
w	131.431
q	53.31
θ	59.006
Average cost	70.174

Table 4.3: RMRC Anaconda stability and control derivatives.

Parameter	**Value**	**CR bound**	**CR%**	**Insen %**
X_u	-9.675	4.529	46.81	6.217
X_w	108.800	7.311	6.722	0.223
X_q	-24.820	3.749	15.100	0.449
Z_u	-1.348	0.257	18.960	1.731
Z_w	3.415	0.219	6.405	0.312
Z_q	-19.280	0.069	0.362	0.023
M_u	3.415	0.862	25.240	5.018
M_w	-1.912	0.660	34.540	4.346
M_q	-4.156	0.968	23.290	0.720
X_{δ_e}	42.940	7.269	16.930	0.505
M_{δ_e}	7.288	1.869	25.650	0.782

Equation (4.4) displays the final RMRC Anaconda longitudinal model. The longitudinal dynamic stability can be determined through the eigenvalue of Equation (4.4). The results indicate that RMRC Anaconda has three stable poles corresponding to three dynamic modes (Table 4.4).

$$\dot{x} = \begin{bmatrix} -2.4188 & 27.1906 & -6.2057 & -9.9465 \\ -0.3370 & 0.8538 & 0.1806 & -0.343 \\ 8.5371 & -4.7791 & -10.3898 & 0 \\ 0 & 0 & 1.0027 & 0 \end{bmatrix} \begin{bmatrix} u \\ w \\ q \\ \theta \end{bmatrix} + \begin{bmatrix} 10.7338 \\ 0.3597 \\ 18.2190 \\ 0 \end{bmatrix} \begin{bmatrix} \delta_e \end{bmatrix} \quad (4.4)$$

Table 4.4: The dynamic modes of the RMRC Anaconda.

	Eigenvalues	f_n (Hz)	ζ	τ
Mode 1	-0.332	NA	NA	3 sec
Mode 2	-0.908	NA	NA	1 sec
Third Oscillatory Mode	-5.357$\pm j$5.908	1.27	0.672	NA

Simulation Model Validation

A verification process is necessary before any conclusions can be made regarding the accuracy of the identified models. Doublet inputs that were not used in the system identification process are applied to the elevators of the RMRC Anaconda in X-Plane (Figure 4.5). The off-axis control surfaces (aileron, rudder, and throttle) are maintained at trim. The response of the aircraft in X-Plane is recorded and compared to the response of the derived models. CIFER is used to calculate unmodeled disturbance biases and reference shifts and to calculate the root mean square error between the model and X-Plane and the Theil inequality coefficient to be used as a measure of the predictive ability of the models.

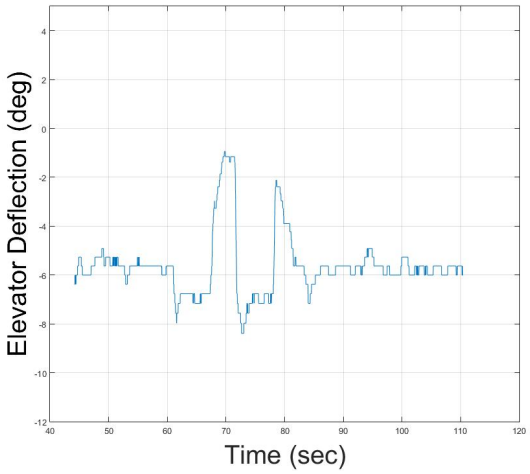

Figure 4.5: Doublet inputs applied to the simulation RMRC Anaconda.

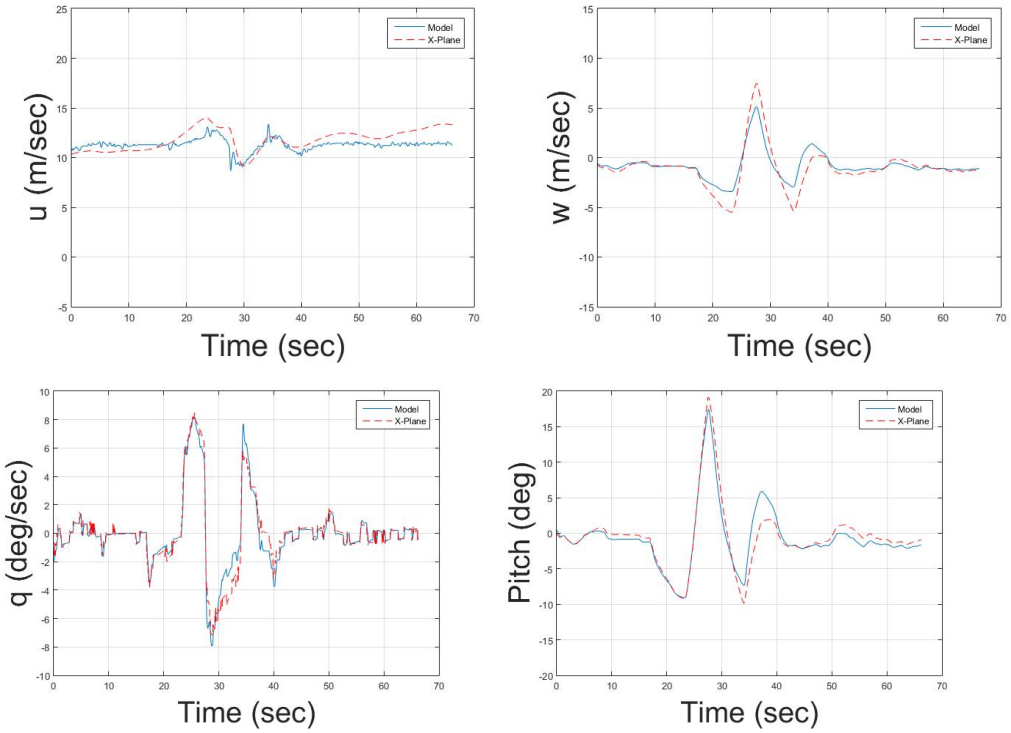

Figure 4.6: The response the RMRC Anaconda model vs. response of X-Plane.

Calculation of the biases and shifts improves the accuracy of the model (Table 4.5). The TIC value of the model indicates excellent model predictive ability. It can be seen from Figure 4.6 and Table 4.5 that the model does not match X-Plane data at higher amplitudes. This is due to the unmodeled non-linear dynamics present during flight.

Table 4.5: J_{rms} and TIC before and after calculation of biases and shifts for the RMRC Anaconda model.

	J_{rms}	TIC
Before calculation of biases and shifts	1.795	0.268
After calculation of biases and shifts	1.309	0.188

4.1.2 Lateral Model

Simulation Model Derivation

Frequency sweep inputs are applied to the aileron (Figure 4.7) while the throttle is maintained at 60% of full power. Elevator inputs are limited to small pulse inputs that guarantee decoupling of UAV dynamics. The frequency range of the sweep inputs is approximately between 0.05 Hz to 1.2 Hz.The UAV lateral velocity (v), roll rate (p), and roll (ϕ) are recorded (Figure 4.8).

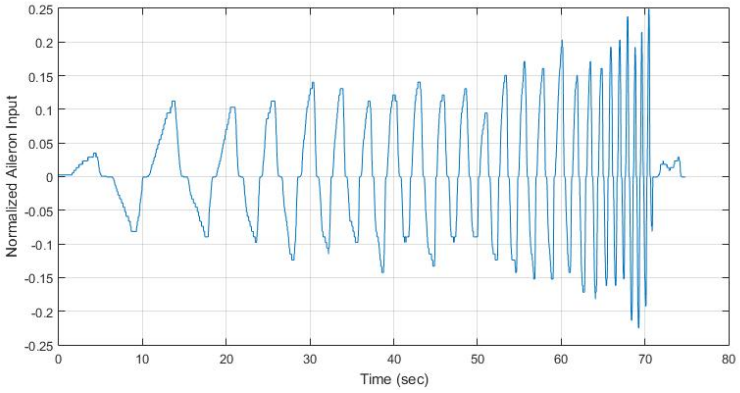

Figure 4.7: X-Plane aileron input signal.

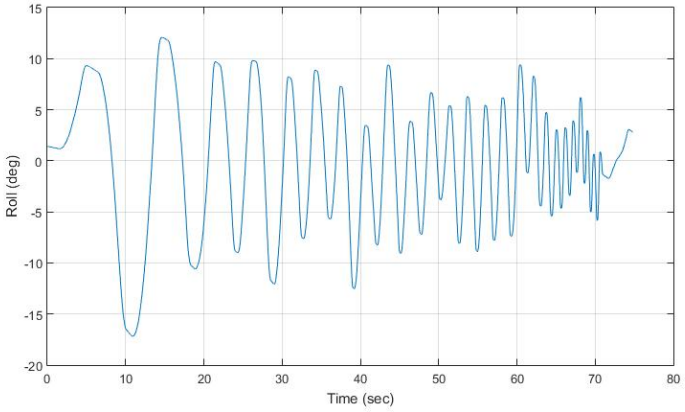

Figure 4.8: Roll angle of simulation RMRC Anaconda.

Identical steps are taken as the longitudinal model to calculate coherence values, multiple input conditioning, and perform data windowing by CIFER. Figure (4.9) indicates that the coherence values for all identified parameters are greater than 0.6 for the entire frequency range.

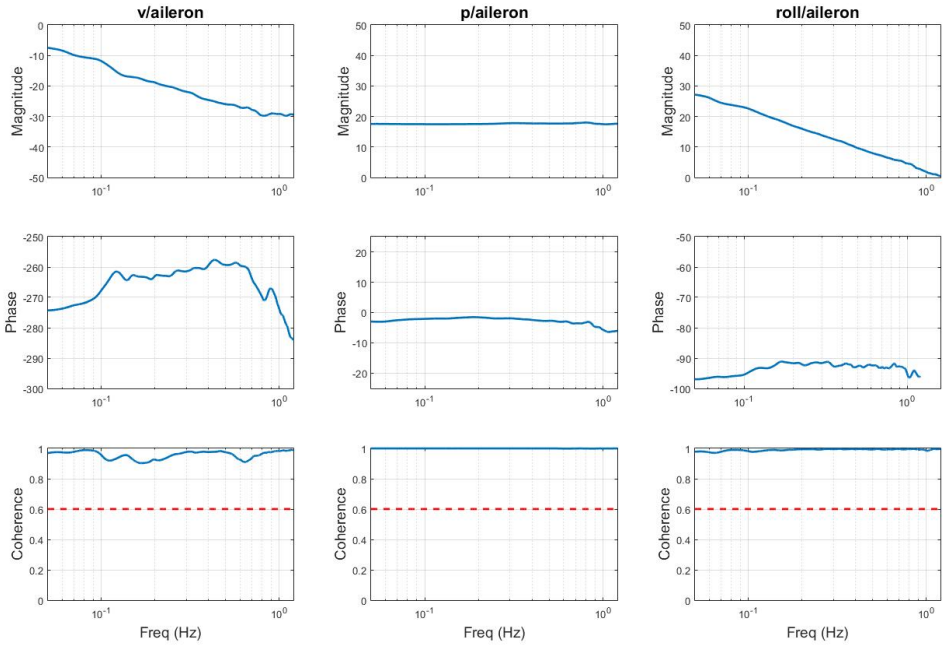

Figure 4.9: Simulated frequency response of RMRC Anaconda lateral motion.

The lateral model structure presented in Equation (3.2) is chosen for identification. To allow the direct identification of the stability and control derivatives, the model is decomposed to its canonical form (Equation (4.5))

$$M = \begin{bmatrix} m & 0 & 0 \\ 0 & I_x & 0 \\ 0 & 0 & 1 \end{bmatrix}, F = \begin{bmatrix} Y_v & Y_p & -gcos(\theta_0) \\ L_v & L_p & 0 \\ 0 & 1 & 0 \end{bmatrix}, G = \begin{bmatrix} Y_{\delta_a} \\ L_{\delta_a} \\ 0 \end{bmatrix} \tag{4.5}$$

CIFER's optimization algorithm is used to calculate final stability and control derivatives and derive the mathematical values. The cost values for the identified parameters are well within the accepted standards (Table 4.6). Cramér Rao and insensitivity values are also within the accepted percentages. The results obtained indicate a small delay in aircraft response (represented as τ in Table 4.7). The cost function is highly sensitive to τ ($Insen = 2.916$), therefore it was not omitted from the model. The RMRC Anaconda lateral mode is shown in Equation (4.6).

Table 4.6: Cost values of lateral dynamics after CIFER optimization.

	RMRC Anaconda
v	21.37
p	8.46
ϕ	12.19
Average cost	14.01

Table 4.7: Lateral RMRC Anaconda stability and control derivatives

Parameter	**Value**	**CR bound**	**CR %**	**Insen %**
Y_v	-12.1400	1.5410	12.70	3.040
Y_p	-0.1479	0.0181	12.23	1.556
L_p	-1.2800	0.2559	19.99	1.090
Y_{ail}	0.3895	0.1420	36.44	4.750
L_{ail}	10.9800	1.7840	16.26	0.9681
τ	-0.0998	0.0194	19.44	2.916

$$\dot{x} = \begin{bmatrix} -3.0350 & -0.0370 & -0.0332 \\ -0.8750 & -8.0013 & 0 \\ 0 & 1 & 0 \end{bmatrix} \begin{bmatrix} v \\ p \\ \phi \end{bmatrix} + \begin{bmatrix} 0.0974 \\ 68.5999 \\ 0 \end{bmatrix} \begin{bmatrix} \delta_a \end{bmatrix} \quad (4.6)$$

The eigenvalues of the identified model indicate that the UAV has two stable dynamic modes (Table 4.8). Due to the omission of rudder control surface from the model, the damping ratio and natural frequency of the dynamic modes were not captured.

Table 4.8: The lateral dynamic modes of the RMRC Anaconda.

	Eigenvalues	f_n (Hz)	ζ	τ
Mode 1	-3.0396	NA	NA	0.3 sec
Mode 2	-7.9955	NA	NA	0.1 sec

Simulation Model Validation

Doublet inputs that were not used in the system identification process are applied to the elevators of the RMRC Anaconda in X-Plane (Figure 4.10). The off-axis control surfaces (aileron, rudder, and throttle) are maintained at trim. The response of the aircraft in X-Plane is recorded and compared to the response of the derived models (Figure 4.11). CIFER is used to calculate unmodeled disturbance biases and reference shifts and to calculate the root mean square error between the model and X-Plane and the Theil inequality coefficient to be used as a measure of the predictive ability of the models (Figure 4.10).

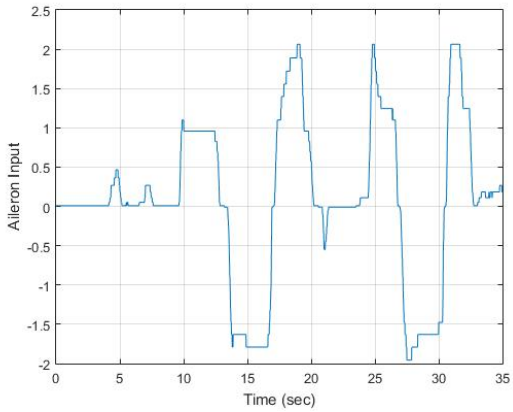

Figure 4.10: Aileron doublet input.

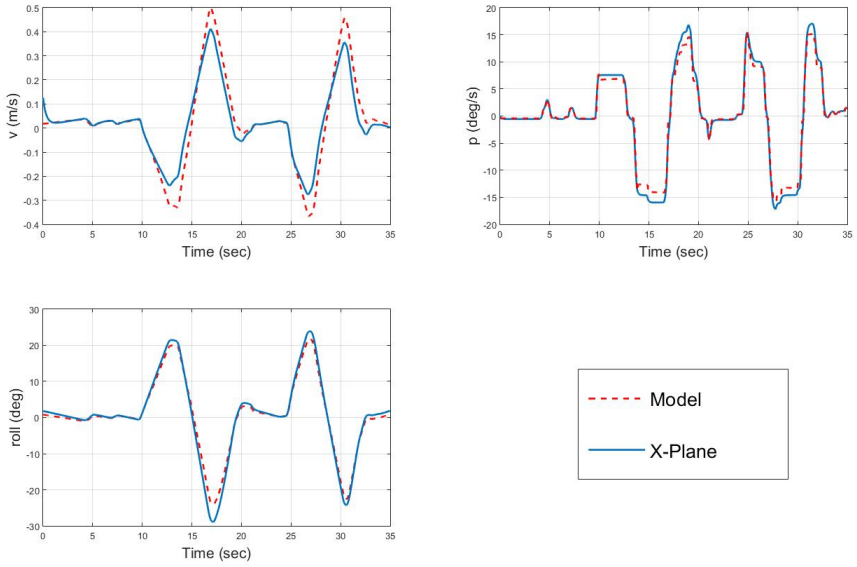

Figure 4.11: Lateral X-Plane model response vs mathematical model response of the RMRC Anaconda.

Table 4.9: J_{rms} and TIC before and after calculation of biases and shifts for the RMRC Anaconda lateral model.

	J_{rms}	TIC
Before calculation of biases and shifts	1.755	0.112
After calculation of biases and shifts	1.040	0.066

The final J_{rms} TIC values are well within the minimum acceptable values. This validates the accuracy and predictive ability of the derived models.

4.2 UC^{2}AV Aircraft

The UC^{2}AV longitudinal and lateral model structures are identical to RMRC Anaconda (Equations 3.1 and 3.2). Elevator sweeps are applied and the forward velocity (u), vertical velocity (w), pitch angle (θ), and pitch rate of change (q) responses are recorded. The data are used to identify the longitudinal model. The lateral model is identified by applying aileron sweeps and capturing the lateral velocity (v), roll rate of change (p), and roll angle (ϕ). As in the previous section, the yaw rate of change variable (r) seen in Equation (3.2) was omitted from the lateral model as rudder input sweeps are required to capture the yaw dynamics.

4.2.1 Longitudinal Model

Simulation Model Derivation

The guidelines discussed in Section 3.4.1 are followed to excite system dynamics and decouple the longitudinal and lateral motion. The UC^{2}AV model derivation process is identical to RMRC Anaconda model derivation. Figure 4.12 presents an example of an elevator sweep implemented while figure 4.13 presents the response of the UC^{2}AV to the sweep input.

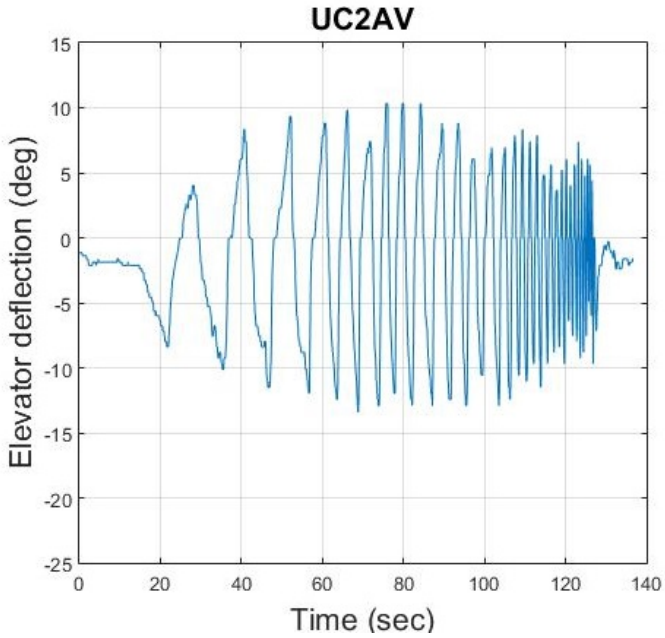

Figure 4.12: Elevator sweep signal applied to excite UAV dynamics.

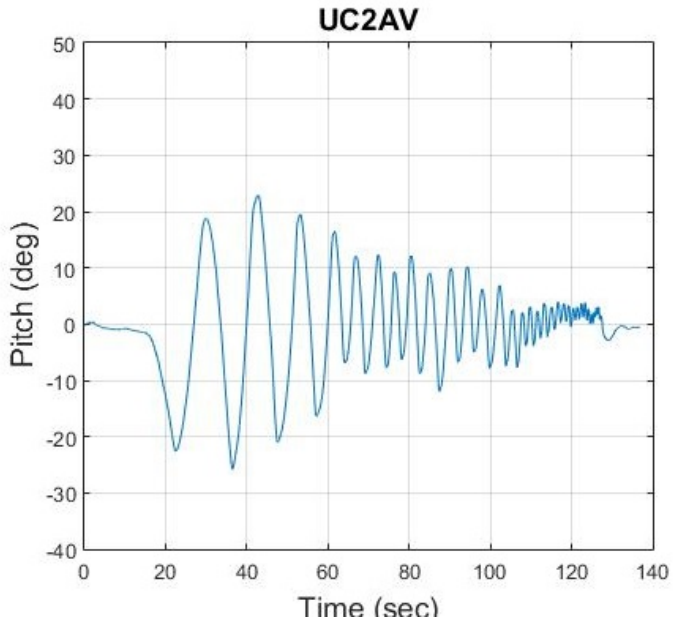

Figure 4.13: Pitch angle response of the UC^{2}AV.

The longitudinal model to be identified (Equation 3.1) is converted to the canonical form to allow direct identification of the stability and control derivatives. The recorded data are imported to CIFER which performs chirp z-transform to calculate a coherence function

for each parameter (Figure 4.14 and Table 4.10). It can be seen that the u acceptable coherence range has slightly increased when compared to the RMRC Anaconda. This is likely due to the additional weight of the UC^{2}AV which decreases the response time of u to elevator inputs.

Table 4.10: Frequency ranges of model variables with acceptable coherence values.

	UC^{2}AV (Hz)
u	0.05-0.20
w	entire range
q	entire range
θ	entire range

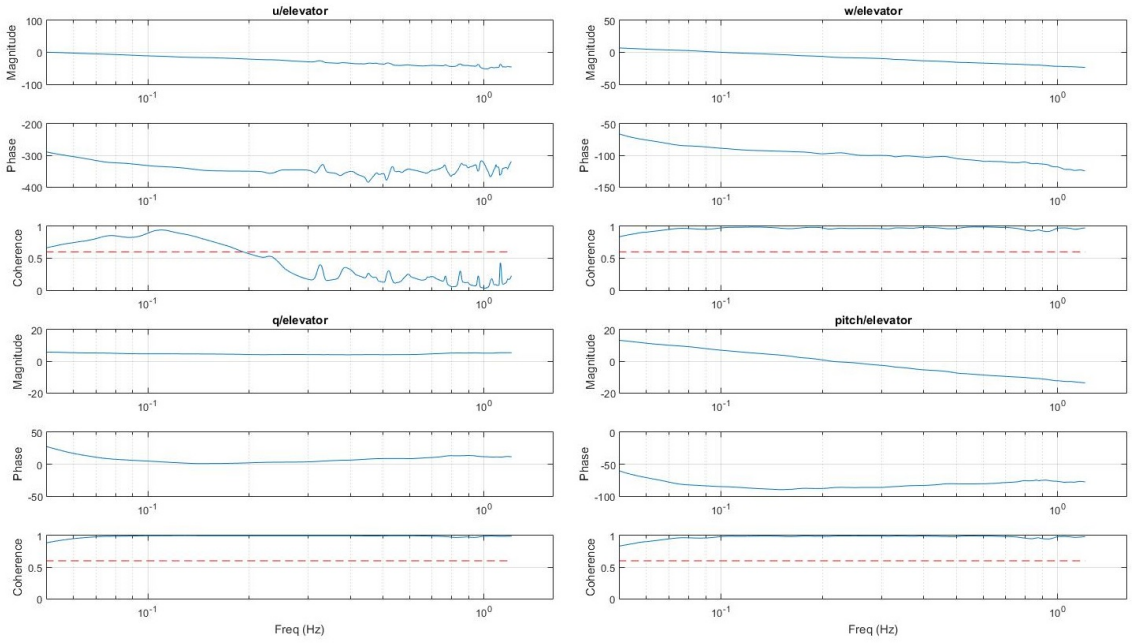

Figure 4.14: Magnitude, phase, and coherence plots for every identified variable of the UC^{2}AV.

CIFER's DERVID function is used to derive a model by optimizing the cost function, estimate stability and control derivatives, and calculate Cramér Rao percentages and bound

and insensitivity percentages. Table 4.12 indicate that all parameters meet the CIFER standard except X_u, this is likely due to the limited amount of data available for identifying u dynamics. M_q and $M_w \leq 0$ which implies static stability.

Table 4.11: Cost values after CIFER optimization.

	UC^{2}AV
u	40.697
w	50.519
q	62.513
θ	66.409
Average cost	55.034

Table 4.12: UC^{2}AV stability and control derivatives.

Parameter	**Value**	**CR bound**	**CR%**	**Insen %**
X_u	-6.856	5.625	82.040	7.433
X_w	92.610	5.166	5.578	0.171
X_q	-35.480	8.300	23.400	0.218
Z_u	-1.609	0.370	23.010	1.235
Z_w	3.192	0.171	5.345	0.229
Z_q	-18.110	0.093	0.511	0.024
M_u	4.333	0.774	17.860	2.108
M_w	-1.917	0.463	24.160	1.503
M_q	-5.780	0.895	15.470	0.233
X_{δ_e}	51.970	12.370	23.790	0.223
M_{δ_e}	8.176	1.396	17.070	0.248

The UC^{2}AV longitudinal model is shown in Equation (4.7). The eigenvalues of the derived model indicate that the UC^{2}AV has two stable longitudinal dynamic modes (Table 4.13).

$$\dot{x} = \begin{pmatrix} -1.3711 & 18.5218 & -7.0951 & -7.9572 \\ -0.3218 & 0.6385 & 0.3771 & -0.2744 \\ 10.3166 & -4.5636 & -13.7626 & 0 \\ 0 & 0 & 1.0000 & 0 \end{pmatrix} \begin{pmatrix} u \\ w \\ q \\ \theta \end{pmatrix} + \begin{pmatrix} 10.3949 \\ 0.0564 \\ 19.4674 \\ 0 \end{pmatrix} \begin{pmatrix} \delta_e \end{pmatrix} \tag{4.7}$$

Table 4.13: The dynamic modes of the UC^{2}AV.

	Eigenvalues	f_n (Hz)	ζ	τ
Mode 1	-0.260$\pm j$0.230	0.055	0.745	NA
Mode 2	-6.987$\pm j$5.819	1.447	0.768	NA

Simulation Model Validation

The UC^{2}AV model derivation process is identical to the RMRC Anaconda model derivation. This section presents the response of the model verses the response of UC^{2}AV in X-Plane to identical doublet inputs (Figures 4.15 and 4.16. Root mean square and TIC values are also presented (Table 4.14).

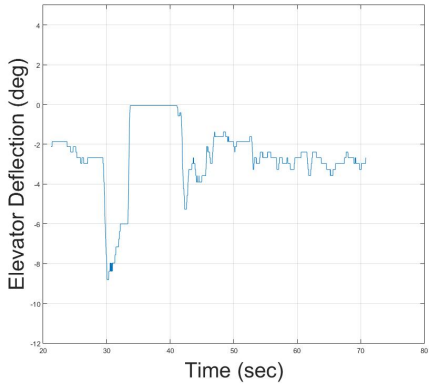

Figure 4.15: Doublet input applied to the UC^{2}AV.

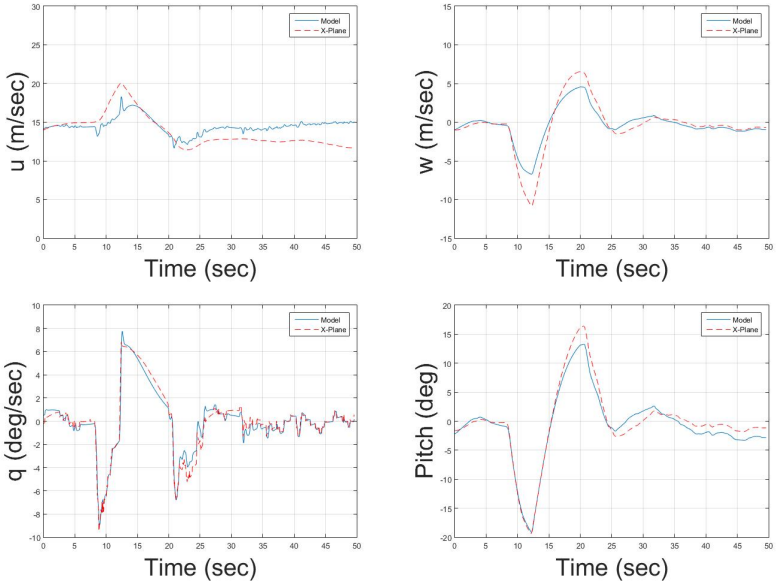

Figure 4.16: The response the UC^{2}AV model vs. response of X-Plane.

Table 4.14: J_{rms} and TIC before and after calculation of biases and shifts for the UC^{2}AV model.

	J_{rms}	TIC
Before calculation of biases and shifts	1.272	0.145
After calculation of biases and shifts	1.092	0.125

The final J_{rms} and TIC values are within the accepted standards which indicates acceptable model accuracy and predictive ability. The identified model does not capture the large amplitude responses of the UC^{2}AV (Figure 4.16). This is likely due to the unmodeled nonlinear dynamics.

4.2.2 Lateral Model

Simulation Model Derivation

Aileron sweep inputs are applied to excite the lateral system dynamics (Figures 4.17 and 4.18). The aileron sweeps begin at a frequency of 0.05 Hz and linearly progress to a frequency of 1.2 Hz. The UAV's lateral velocity (v), roll rate (p), and roll (ϕ) are recorded.

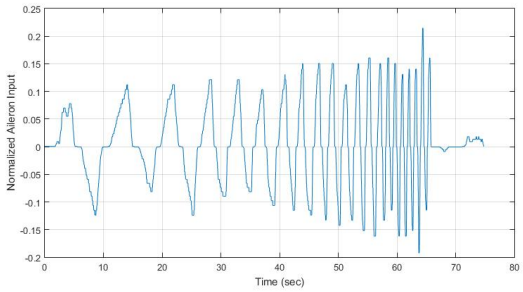

Figure 4.17: Sweep input applied to the UC^{2}AV.

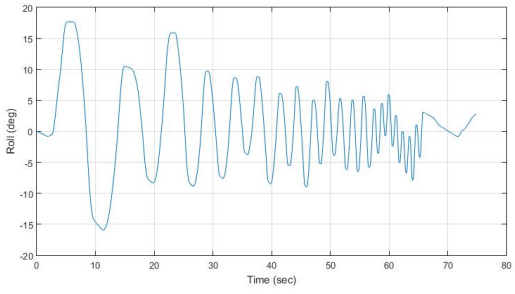

Figure 4.18: Roll response to sweep signal.

Coherence values are calculated for each identified parameter (Figure 4.19). Coherence values for all identified parameters are greater than the minimum 0.6 for the entire frequency range.

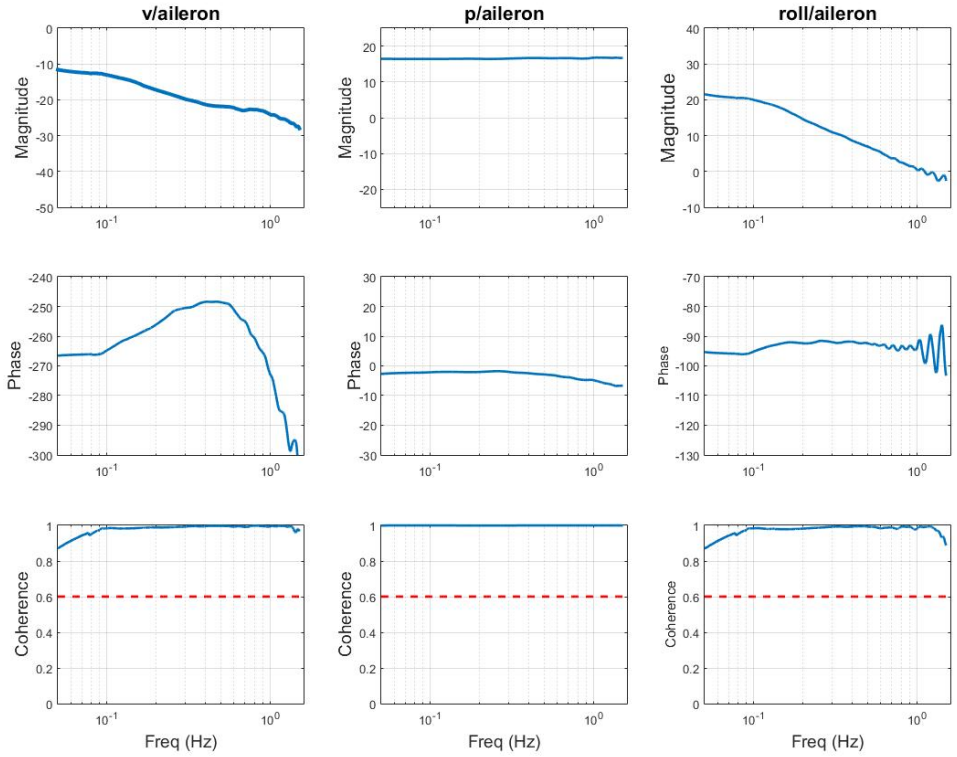

Figure 4.19: Magnitude, phase and coherence plots for all the identified lateral variables of the UC^{2}AV.

CIFER optimizes the defined cost function and derives the mathematical model. The final cost values for every identified parameter is presented in Table 4.15. Cramér Rao percentages and bound and insensitivity percentages for every stability and control derivative is presented in Table 4.16. The final cost, Cramér Rao, and insensitivity values are within the accepted range. CIFER identifies a delay in UAV response modeled by the parameter τ. The delay is not omitted from the final identified model due to its low insensitivity percentage (Table 4.16). The UC^{2}AV lateral model is shown in Equation (4.8).

Table 4.15: Cost values of lateral UC^{2}AV dynamics after CIFER optimization.

	UC^{2}AV
v	59.59
p	11.36
ϕ	82.17
Average cost	51.04

Table 4.16: Lateral UC^{2}AV stability and control derivatives

Parameter	**Value**	**CR bound**	**CR %**	**Insen %**
Y_v	-21.1700	1.3490	6.37	2.064
Y_p	-0.4300	0.0662	15.40	1.863
L_p	-1.6910	0.4819	28.49	1.014
Y_{ail}	1.0850	0.4254	39.21	4.707
L_{ail}	11.0100	2.9540	26.84	0.9797
τ	-0.0669	0.0245	36.53	6.357

$$\dot{x} = \begin{pmatrix} -5.2929 & -0.1075 & -0.0968 \\ 0.8750 & -10.5693 & 0 \\ 0 & 1 & 0 \end{pmatrix} \begin{pmatrix} v \\ p \\ \phi \end{pmatrix} + \begin{pmatrix} 0.2713 \\ 68.7891 \\ 0 \end{pmatrix} \begin{pmatrix} \delta_a \end{pmatrix} \tag{4.8}$$

The eigenvalues of the model indicate two stable dynamic modes. Due to the omission of the rudder control surface from the model, damping ratios and natural frequencies of the modes were not captured.

Table 4.17: The lateral dynamic modes of the UC^{2}AV.

	Eigenvalues	f_n (Hz)	ζ	τ
Mode 1	-5.31	NA	NA	0.2
Mode 2	-10.55	NA	NA	0.1

Simulation Model Validation

Lateral model validation process is identical to longitudinal model validation. Doublet inputs are applied to the aileron while the response is recorded in X-Plane. This section presents the response of the model verse response of in X-Plane (Figures 4.20 and 4.21) and root mean square error and TIC values (Table 4.18).

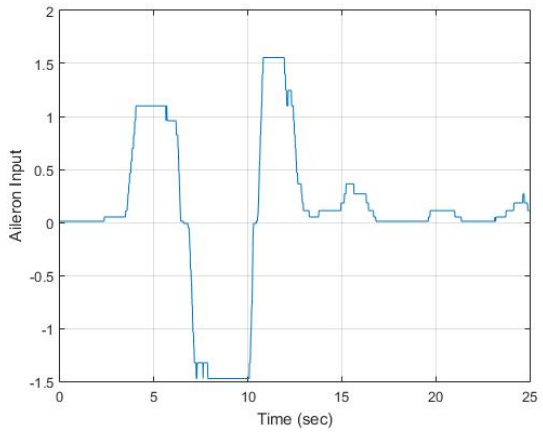

Figure 4.20: Doublet input applied to the UC^{2}AV.

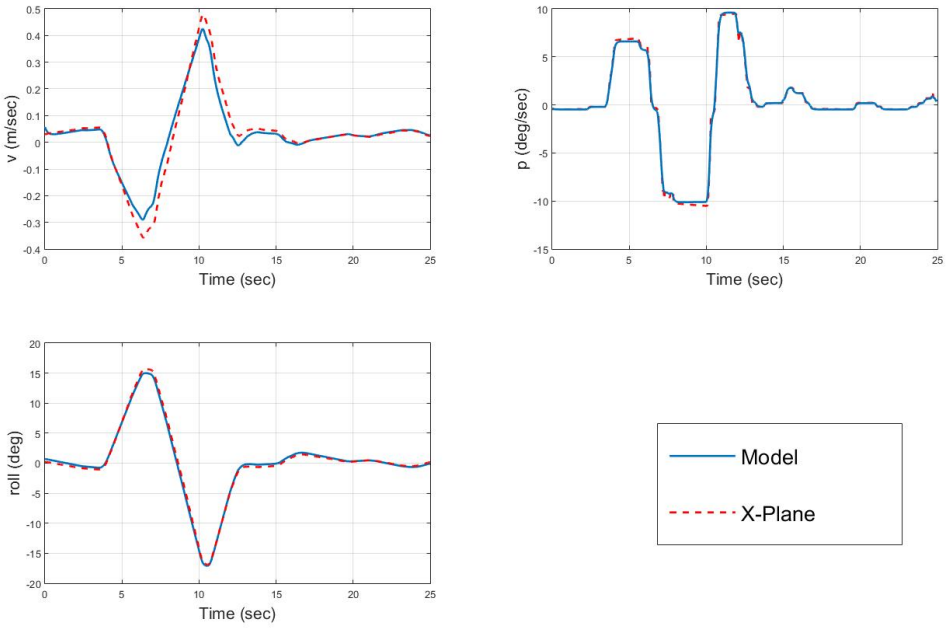

Figure 4.21: X-Plane response vs mathematical model response.

Table 4.18: J_{rms} and TIC before and after calculation of biases and shifts for the UC^{2}AV model.

	J_{rms}	TIC
Before calculation of biases and shifts	2.065	0.177
After calculation of biases and shifts	0.308	0.027

The final J_{rms} TIC values are well within the minimum acceptable values (Table 4.18). This validates the accuracy and predictive ability of the derived models.

The J_{rms} and TIC values indicate accurate simulation model identification. To guarantee static and dynamic stability, the location of gravity of both UAVs are placed at the front end (the nose of the UAV). The location of center of gravity is also modeled in X-Plane's Plane Maker software. Parameter estimation of both UAVs and analysis of dynamic modes

indicate that both UAVs are dynamically and statically stable. The simulation results obtained match the known UAV properties. This verifies the proposed system identification method.

Chapter 5

Flight Data Results and Analysis

This chapter presents the mathematical models obtained through flight testing. Three sets of models are derived, these are: 1) RMRC Anaconda longitudinal and lateral models; 2) CC-off UC^{2}AV longitudinal and lateral models; and 3) CC-on UC^{2}AV longitudinal and lateral models.

5.1 RMRC Anaconda Aircraft

The longitudinal model is identified by applying elevator sweeps and capturing the forward velocity (u), vertical velocity (w), pitch angle (θ), and pitch rate of change (q) responses. However, due to limited identifiable frequency range, the velocity u was not identified and was omitted from the final model. The lateral model is identified by applying aileron sweeps and capturing the lateral velocity (v), roll rate of change (p), and roll angle (ϕ). The yaw rate of change variable (r) seen in Equation (3.2) was omitted from the lateral model as rudder input sweeps are required to capture the yaw dynamics.

5.1.1 Longitudinal Model

Model Derivation

Due to the limited radio communication range, it is difficult to perform a single frequency sweep beginning at the minimum frequency of interest and progressing to the maximum frequency of interest. Instead, sweep maneuvers are performed at discrete frequency values. The collected data is concatenated in CIFER. Figure 5.1 presents an example of a sweep maneuver performed at roughly 0.7 Hz and Figure 5.2 presents the RMRC Anaconda response. The data recorded by the avionic system is imported to Matlab to perform signal processing then to CIFER to perform system identification.

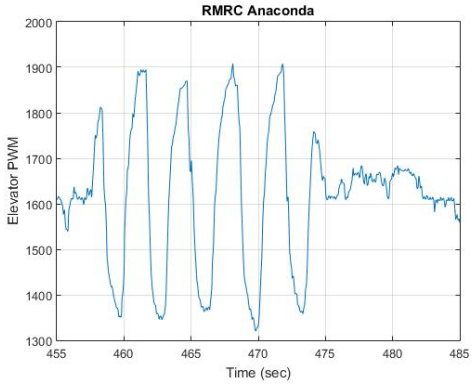

Figure 5.1: RMRC Anaconda elevator PWM input signal.

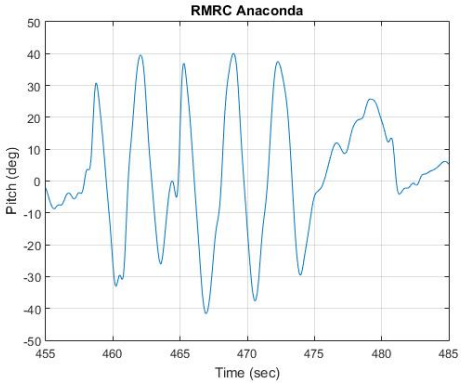

Figure 5.2: RMRC Anaconda pitch angle.

The signal processing procedure begins by parsing the stored data, calculating linear velocities from accelerometer and GPS data by performing sensor fusion and signal interpolation. Since multiple sweeps are performed at discrete frequency values, the data sets that best match the sweep requirements discussed in Chapter 3 are used for system identification (Figure 5.3).

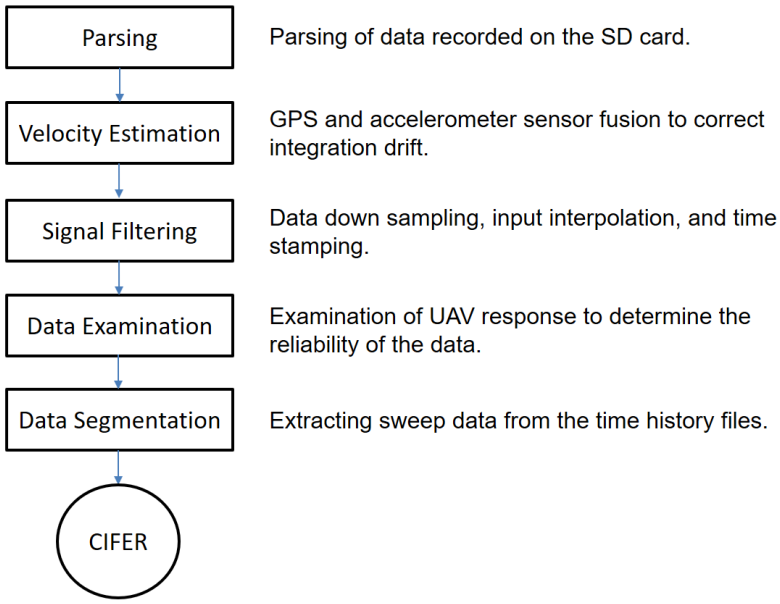

Figure 5.3: Signal processing procedure.

Figure 5.4 presents the frequency response data for each parameter. It can be seen that the u coherence values are consistently less than 0.6. The u parameter is dynamically present at low frequencies, as shown in the simulation tests (Table 4.1). Due to persistent excitation requirements (discussed in section 3.4.3), it is difficult to identify dynamics below 0.35 Hz. Therefore, the parameter u was omitted from the model. Throttle sweeps were performed to investigate the relationship between u and throttle inputs. Throttle sweeps at frequencies > 0.35 did not produce high coherence values (Figure 5.5). Therefore, throttle inputs are not included in the final model.

Table 5.1: Frequency ranges of longitudinal RMRC Anaconda model variables with acceptable coherence values.

	RMRC Anaconda (Hz)
u	NA
w	0.45-0.70
q	0.35-0.80
θ	0.35-0.80

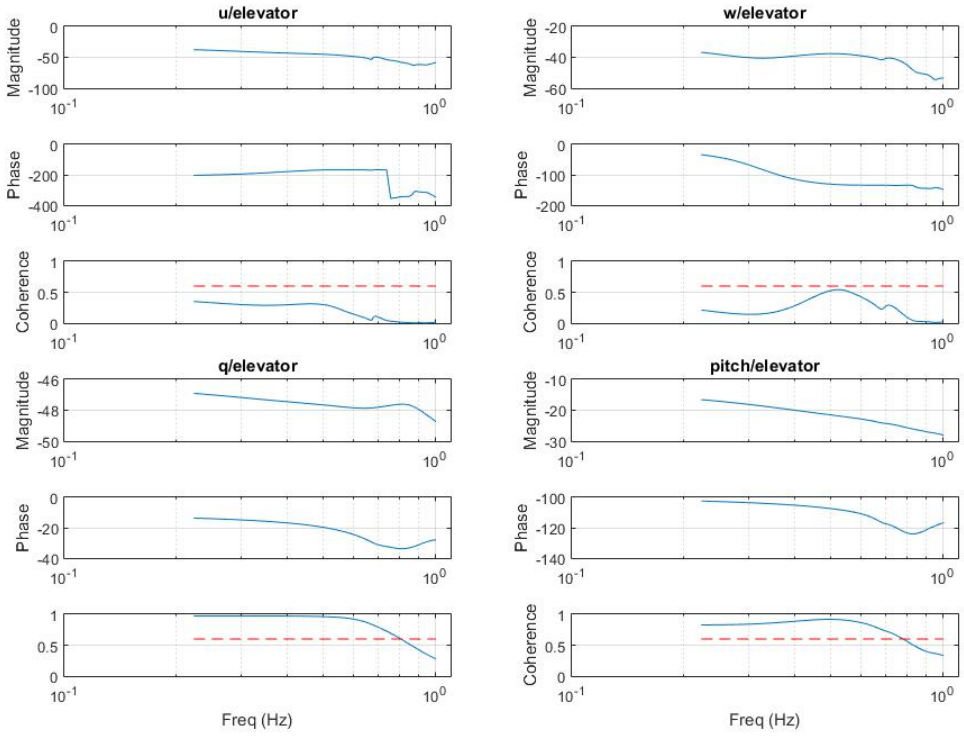

Figure 5.4: RMRC Anaconda longitudinal frequency response due to elevator sweeps.

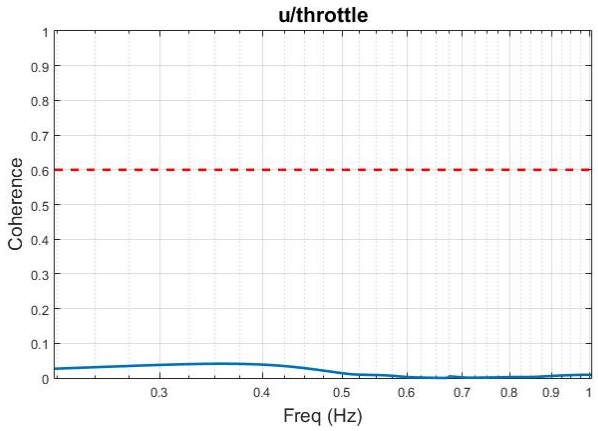

Figure 5.5: There are small changes in u due to throttle sweeps at frequencies > 0.35 which result in low coherence values.

The mathematical model is decomposed to its canonical form to allow direct identification of the stability and control derivatives. CIFER cost optimization function is implemented to derive the mathematical model. Table 5.2 presents the final cost values while Table 5.3 presents the stability and control derivatives.

Table 5.2: Longitudinal RMRC Anaconda cost values after CIFER optimization.

	RMRC Anaconda
w	5.139
q	11.788
θ	19.713
Average cost	12.214

The minimum acceptable standards for accurate models is to have average cost value less than 100 while no individual parameter cost value exceeds 200. CIFER optimization produces low cost values that are well within the minimum requirements.

Table 5.3: RMRC Anaconda longitudinal stability and control derivatives.

Parameter	**Value**	**CR bound**	**CR%**	**Insen %**
Z_w	-5.533	1.017	18.380	8.190
Z_q	-7.000	2.991	42.720	19.130
M_w	-0.766	0.469	61.260	12.230
M_q	-12.590	11.260	89.440	2.047
M_{δ_e}	0.051	0.047	91.860	2.175
τ	0.137	0.0136	9.981	3.131

Cramér Rao and insensitivity analysis reveal that while stability derivatives meet the insensitivity requirements (less than 10%) the Cramér Rao percentages and bounds do not meet the requirements (less than 20%). This reduces the reliability of the results for parameter estimation. However, the validation experiments reveal that the derived models accurately capture the UAV dynamics. Table 5.4 presents the RMRC Anaconda longitudinal dynamic modes. The final RMRC longitudinal model is shown below:

$$\dot{x} = \begin{pmatrix} -1.3833 & 3.2499 & 0.3424 \\ -1.9155 & -31.4760 & 0 \\ 0 & 1 & 0 \end{pmatrix} \begin{pmatrix} w \\ q \\ \theta \end{pmatrix} + \begin{pmatrix} 0.0217 \\ 0.1279 \\ 0.2755 \end{pmatrix} \begin{pmatrix} \delta_e \end{pmatrix} \tag{5.1}$$

Table 5.4: Longitudinal dynamic modes of the RMRC Anaconda.

	Eigenvalues	f_n (Hz)	ζ	τ
Mode 1	-0.0132	NA	NA	75.75 sec
Mode 2	-1.5776	NA	NA	0.64
Mode 3	-31.2684	NA	NA	0.03

Model Validation

Doublets inputs (Figure 5.6) that were not used in the system identification process are used to validate the models. Doublet inputs are applied to the elevator. The RMRC Anaconda response and inputs are recorded by the avionic system. Identical steps as shown in Figure 5.3 are taken to process the data recorded. Identical doublet inputs are used to simulate the derived mathematical model. Thiel Inequality Coefficient (TIC) and root mean square analysis (J_{rms}) reveal the accuracy of the models (Table 5.5). The response of the model and RMRC Anaconda to the doublet inputs are shown in Figure 5.7.

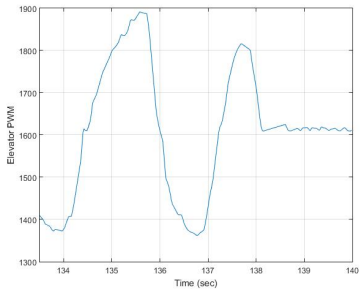

Figure 5.6: RMRC Anaconda elevator inputs used for verification.

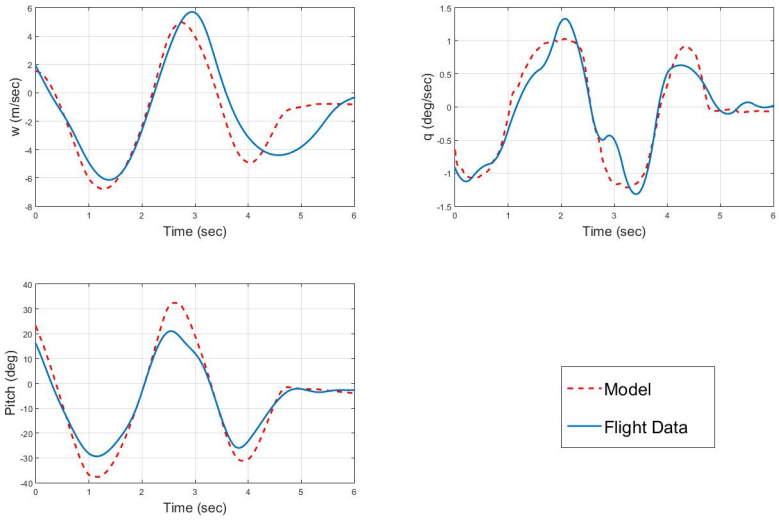

Figure 5.7: The RMRC Anaconda and longitudinal model response.

Table 5.5: J_{rms} and TIC before and after calculation of biases and shifts for the RMRC Anaconda model.

	J_{rms}	TIC
Before calculation of biases and shifts	91.76	0.89
After calculation of biases and shifts	3.20	0.16

The final TIC and J_{rms} values indicate acceptable identification accuracy. While J_{rms} is greater than the minimum standard, this is likely due to untrimmed flight conditions and asymmetric pilot inputs.

The RMRC Anaconda model obtained presents the static and dynamic stability properties of the UAV. The stability derivatives and dynamic modes of the model reveal that the UAV is both statically and dynamically stable. This is expected as the center of gravity is located at the nose of the UAV which is generally required to guarantee stability. Results show that low frequency throttle sweeps do not significantly (coherence < 0.6) effect the forward velocity u of the RMRC Anaconda and was therefore omitted from the model. An identical motor is used in the UC^{2}AV. Since the UC^{2}AV is roughly 4 lbs heavier than the RMRC Anaconda, it is extremely unlikely that throttle sweeps will result in significant changes of the forward velocity u of the UC^{2}AV. Therefore, throttle sweeps were not performed while performing UC^{2}AV system identification.

5.1.2 Lateral Model

Model Derivation

Sweep inputs are applied to the aileron while the elevator is maintained at trim values. The RMRC Anaconda response is recorded and processed following the same procedure as longitudinal sweeps (Figures 5.8 and 5.9).

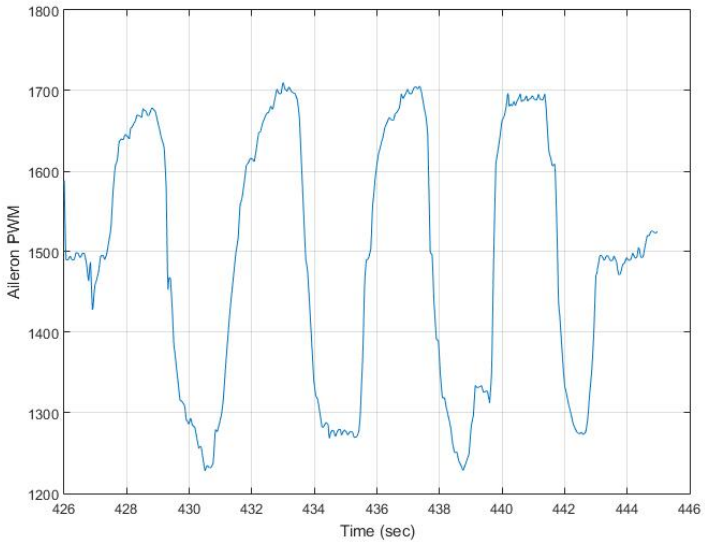

Figure 5.8: The RMRC Anaconda aileron sweep.

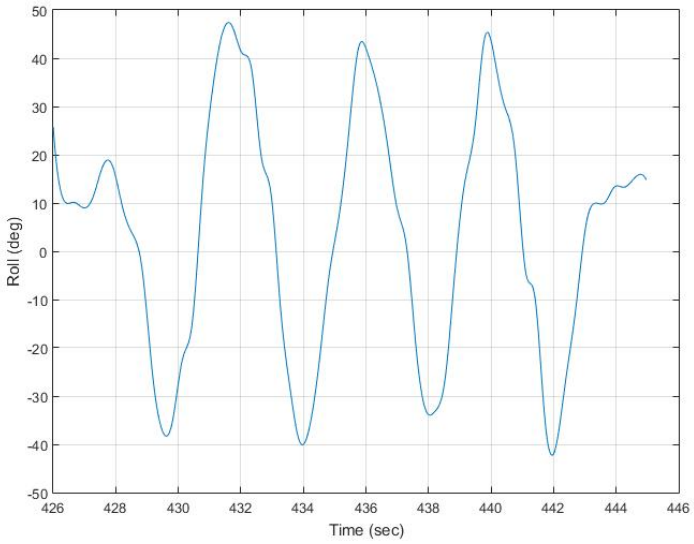

Figure 5.9: RMRC Anaconda roll response due to aileron sweep.

The processed data is imported to CIFER to calculate coherence values and perform cost optimization. Table 5.6 and Figure 5.10 reveal the frequency response and the frequency range with acceptable coherence values. The coherence values for lateral velocity

v is inversely proportional to frequency. This is expected as the change in lateral velocity due to aileron inputs reduces at high frequencies.

Table 5.6: Frequency ranges of model variables with acceptable coherence values.

	RMRC Anaconda (Hz)
v	0.35-0.45
p	0.35-0.90
ϕ	0.35-0.90

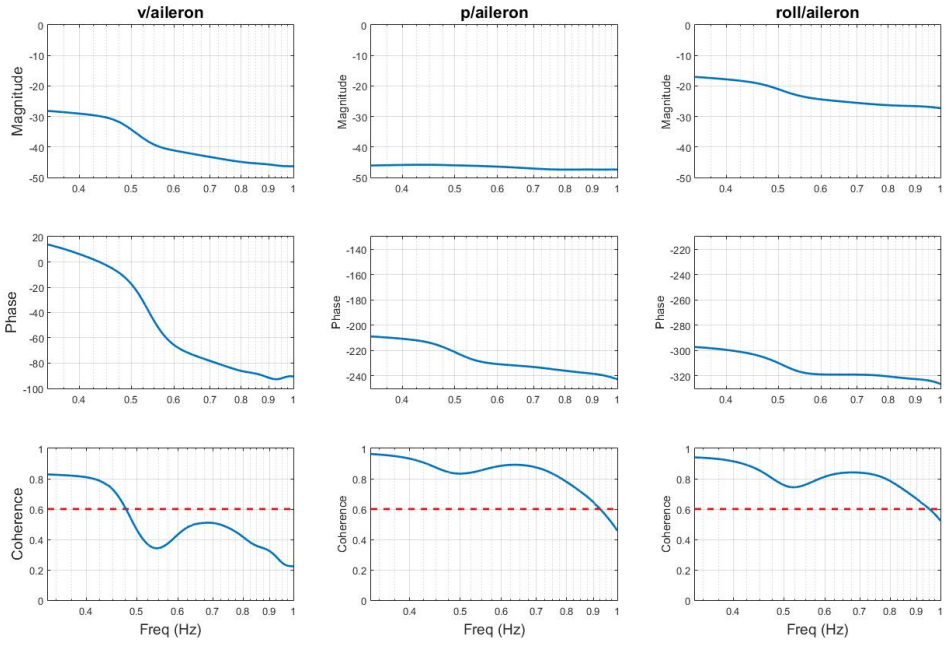

Figure 5.10: Lateral frequency response of the RMRC Anaconda.

The final cost values meet the standards and are shown in Table 5.7. The derived stability and control derivatives are shown in Table 5.8. Table 5.9 indicates the lateral dynamic modes of the RMRC Anaconda. Equation (5.2) presents the final lateral model. The lateral model reveals that the UAV is laterally dynamically stable (eigenvalues < 0).

Table 5.7: Lateral RMRC Anaconda cost values after CIFER optimization.

	RMRC Anaconda
v	74.743
p	20.069
ϕ	32.945
Average cost	42.586

Table 5.8: RMRC Anaconda lateral stability and control derivatives.

Parameter	**Value**	**CR bound**	**CR%**	**Insen %**
Y_p	-39.25	7.857	20.020	1.810
Y_v	-0.167	0.074	44.170	4.142
L_p	-7.831	0.465	5.939	0.281
Y_{δ_a}	-3.088	0.178	5.818	0.314
L_{δ_a}	-0.034	0.003	10.170	0.285
τ	0.183	0.009	4.959	2.158

$$\dot{x} = \begin{pmatrix} -9.8119 & -197.0404 & 2.8083 \\ -0.4780 & -22.3747 & 0 \\ 0 & 1 & 0 \end{pmatrix} \begin{pmatrix} v \\ p \\ \phi \end{pmatrix} + \begin{pmatrix} -0.7720 \\ -0.0971 \\ -0.2520 \end{pmatrix} \begin{pmatrix} \delta_a \end{pmatrix} \tag{5.2}$$

Table 5.9: The lateral dynamic modes of the RMRC Anaconda.

	Eigenvalues	f_n (Hz)	ζ	τ sec
Mode 1	-0.0107	NA	NA	93.45
Mode 2	-4.520	NA	NA	0.22
Mode 3	-27.656	NA	NA	0.04

Model Validation

Doublets inputs (Figure 5.11) are applied to the aileron while the remaining control surfaces are maintained at trim. The response of the RMRC Anaconda and the model is compared by performing TIC and root mean square analysis (Figure 5.12 and Table 5.10).

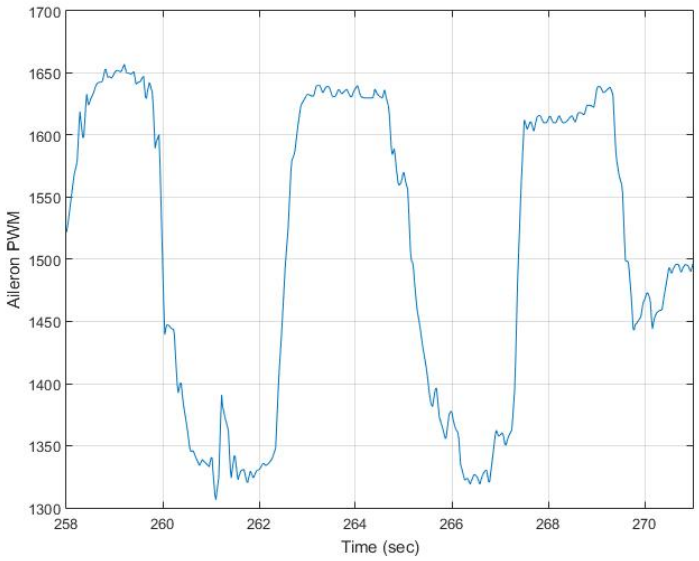

Figure 5.11: Aileron doublet inputs used for model validation.

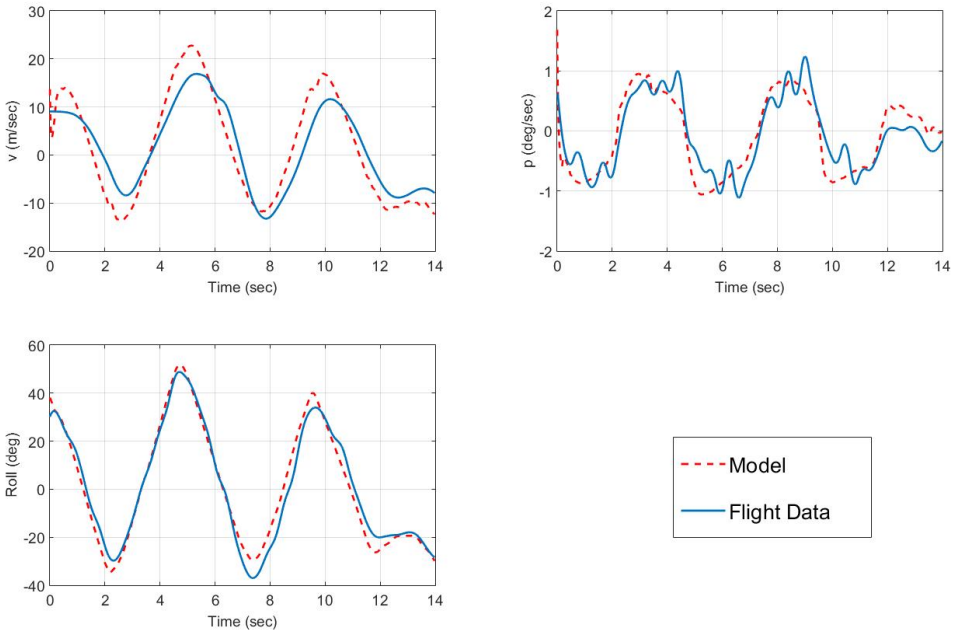

Figure 5.12: RMRC Anaconda response vs. lateral model.

Table 5.10: J_{rms} and TIC before and after calculation of biases and shifts for the RMRC Anaconda lateral model.

	J_{rms}	TIC
Before calculation of biases and shifts	145.000	0.952
After calculation of biases and shifts	3.699	0.087

The final TIC and J_{rms} values indicate acceptable identification results. While the model has excellent predictive ability (as indicated by the TIC value), J_{rms} is greater than the minimum standard. However, this is likely due to asymmetric RMRC Anaconda roll response which results in a non sinusoidal roll rate response.

5.1.3 Remarks

The observations made after performing system identification using flight data are below:

- The stability derivatives of the UAV imply longitudinal static stability. This is expected as the center of gravity is located at the nose of the UAV. Eigenvalues of the models obtained indicate that the UAV possesses both longitudinal and lateral dynamic stability.

- The Cramér Rao bounds and percentages obtained, which are the expected standard deviation of an identified stability or control derivative, have increased when compared to simulation results. Due to limited radio communication range, a single frequency sweep beginning at the minimum frequency of interest and progressing to the maximum frequency of interest could not be performed. This is resolved by performing multiple sweeps at discrete frequency values. This results in multiple short duration (no more than 10 seconds) time history files which is the likely cause of the drop in Cramér Rao bounds and percentages. It was also noted that including more time history data improves the Cramér Rao values.

- Reduction in the acceptable coherence range of the lateral velocity v is observed. Simulation flight tests reveal that while the change in v due to high frequency aileron sweeps is significantly less compared to low frequency sweeps, there still is a sufficient change in v to result in coherence values > 0.6. Flight testing reveals that there is little change in v due to high frequency aileron sweeps resulting in coherence values < 0.6.

- Validation experiments show that the models accurately capture the RMRC Anaconda.

5.2 UC^{2}AV Aircraft

System identification is performed for the UC^{2}AV to capture the longitudinal and lateral models. System identification is performed two times, first, the CC system is turned off, and second, the CC system is turned on and is blowing at maximum capacity.

5.2.1 Circulation Control Off

Longitudinal Model

Model Derivation

Elevator sweeps (Figure 5.13 and 5.14) are performed at discrete frequency values. The avionic system and signal processing procedure is identical to the RMRC Anaconda system and procedure.

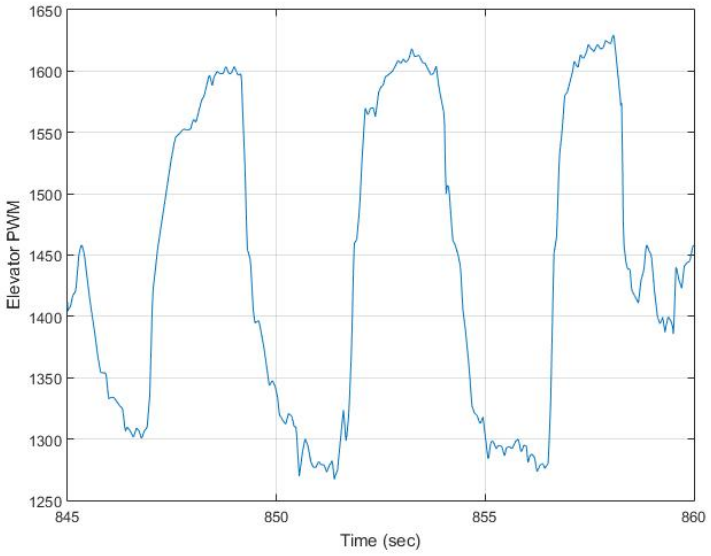

Figure 5.13: UC^{2}AV elevator sweep.

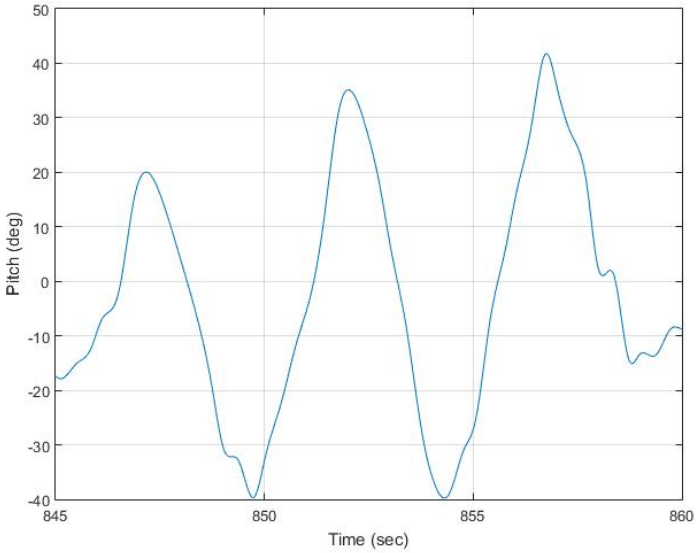

Figure 5.14: UC^{2}AV pitch response.

Table 5.11: Frequency ranges of longitudinal UC^{2}AV (CC-off) model variables with acceptable coherence values.

	UC^{2}AV (Hz)
w	0.35-0.65
q	0.35-0.75
θ	0.35-0.75

The acceptable coherence range has decreased compared to the RMRC Anaconda. The additional weight of the UC^{2}AV and the unchanged motor power makes the UC^{2}AV less responsive to pilot inputs and is the likely cause of the reduction in coherence.

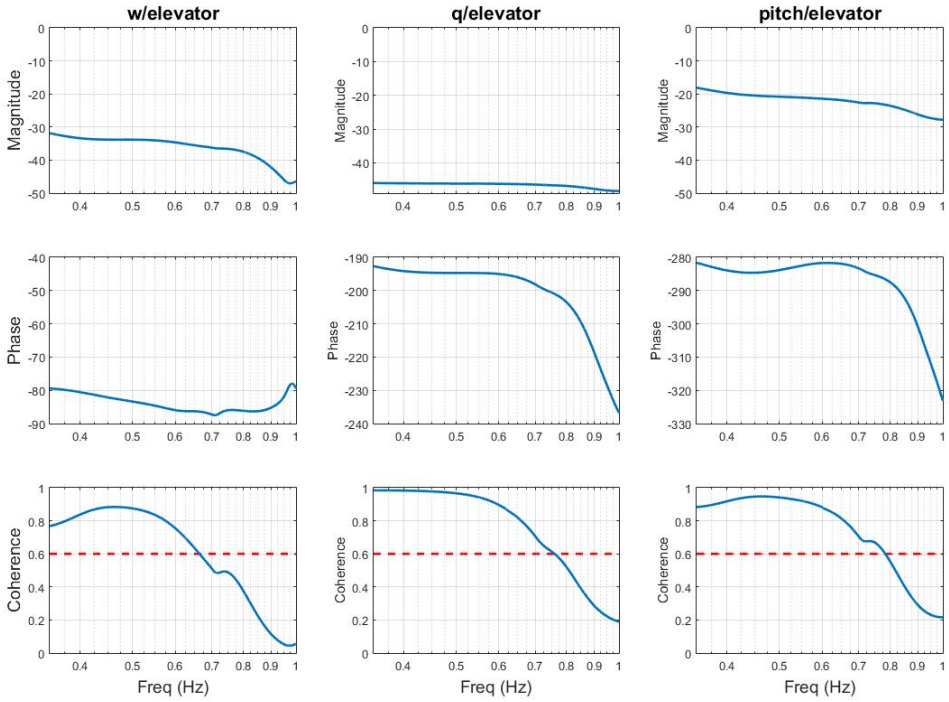

Figure 5.15: Longitudinal UC^{2}AV frequency response (CC-off).

CIFER performs frequency domain analysis to identify the frequency ranges with acceptable coherence values (Table 5.11) and performs cost optimization to derive the mathematical models and the stability and control derivatives (Table 5.12 and 5.13).

Table 5.12: UC^{2}AV (CC-off) longitudinal cost values after CIFER optimization.

	UC^{2}AV
w	7.078
q	19.209
θ	49.864
Average cost	25.384

Table 5.13: UC^{2}AV longitudinal (CC-off) stability and control derivatives.

Parameter	**Value**	**CR bound**	**CR%**	**Insen %**
Z_q	-116.600	10.690	9.174	1.005
M_w	0.203	0.029	14.180	3.404
M_q	-2.374	0.237	9.980	1.014
Z_{δ_e}	-0.401	0.049	12.400	1.552
M_{δ_e}	-0.011	0.003	11.670	1.141

The longitudinal dynamic modes are presented in Table 5.14. The derived stability derivative and the dynamic modes identified reveal that the UC^{2}AV (CC-off) is both statically and dynamically stable. The final UC^{2}AV CC-off model is shown below:

$$\dot{x} = \begin{pmatrix} 0.0481 & -23.3137 & 0 \\ 0.4063 & -4.7489 & 0 \\ 0 & 1 & 0 \end{pmatrix} \begin{pmatrix} w \\ q \\ \theta \end{pmatrix} + \begin{pmatrix} -0.0802 \\ -0.0229 \\ -0.3443 \end{pmatrix} \begin{pmatrix} \delta_e \end{pmatrix} \tag{5.3}$$

Table 5.14: The longitudinal dynamic modes of the UC^{2}AV (CC off).

	Eigenvalues	f_n (Hz)	ζ	τ sec
Mode	-2.350 ± 1.928	0.773	0.483	NA

Model Validation

Doublet inputs are applied to the elevator for model validation (Figure 5.16). The response of the model is compared to the response of the UC^{2}AV. TIC and J_{rms} values indicate acceptable model results.

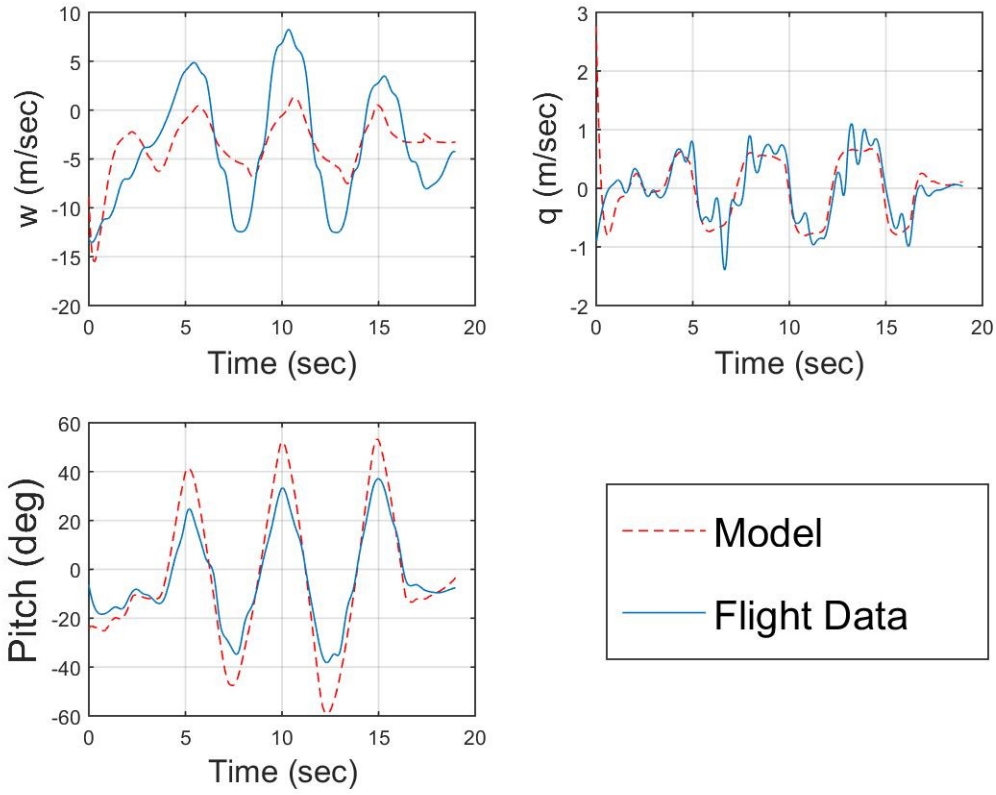

Figure 5.16: UC^{2}AV response vs. model response

Table 5.15: J_{rms} and TIC before and after calculation of biases and shifts for the UC^{2}AV model.

	J_{rms}	TIC
Before calculation of biases and shifts	18.187	0.551
After calculation of biases and shifts	4.599	0.184

The final model has acceptable predictive ability as indicated by the final TIC value. However, the model does not capture the the vertical velocity w accurately. This is likely due to poor sweep signal quality. Further flight testing should improve the accuracy of the model.

Lateral Model

Model Derivation

Aileron sweeps are applied to identify the lateral dynamics model (Figure 5.17 and 5.18). The response of the UC^{2}AV is recorded and processed using the same procedure as the previous models.

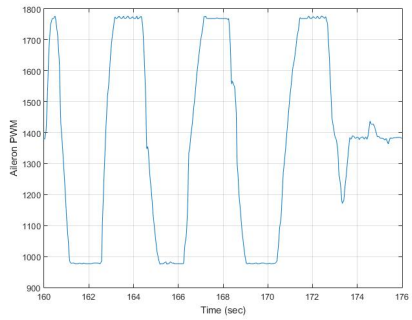

Figure 5.17: UC^{2}AV aileron sweeps.

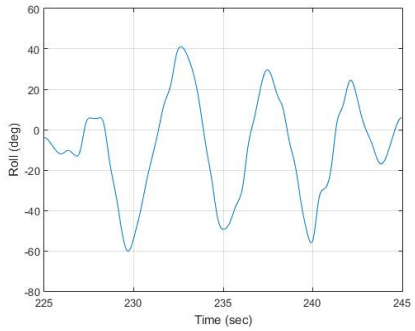

Figure 5.18: UC^{2}AV roll response to aileron sweeps.

Table 5.16: UC^{2}AV (CC-off) lateral frequency ranges of model variables with acceptable coherence values.

	UC^{2}AV (Hz)
v	0.35-0.45
p	0.35-0.55
ϕ	0.35-0.55

The values obtained indicate a significant decrease in acceptable coherence range of the UC^{2}AV compared to the RMRC Anaconda. The noted decrease is greater than the decrease of the longitudinal coherence values. There are two reasons for this observation: i) the additional weight makes the UC^{2}AV laterally less response to pilot input; and ii) the UC^{2}AV has a significantly smaller aileron surface (RMRC Anaconda: 48 x 5 cm, UC^{2}AV: 32 x 2.5 cm). This reduces the lateral dynamic maneuverability of the UC^{2}AV.

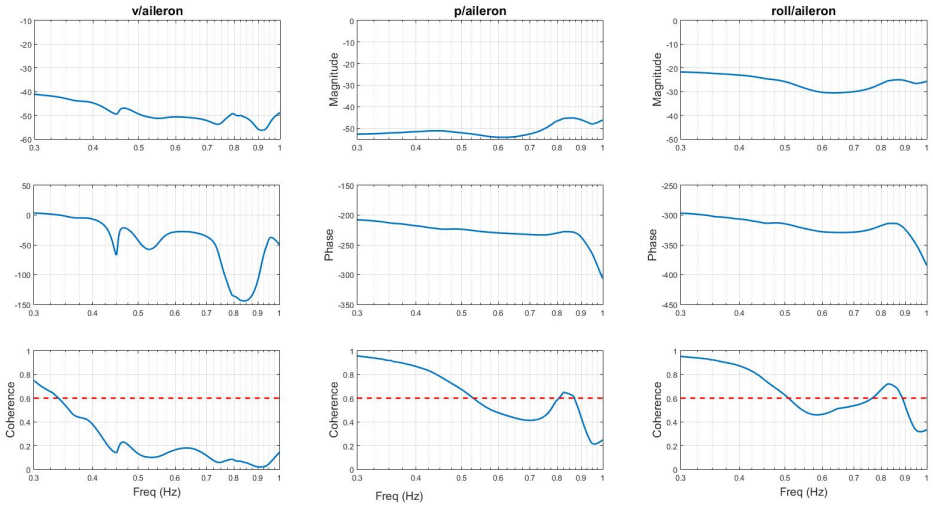

Figure 5.19: UC^{2}AV (CC-off) lateral frequency response.

CIFER calculates the coherence values for the frequency ranges. As in the case of the RMRC Anaconda, the v coherence values drop below the minimum 0.6 for frequencies greater than 0.45 Hz (Figure 5.19 and Table 5.17).

Table 5.17: Cost values after CIFER optimization.

	UC^{2}AV
v	30.128
p	61.655
ϕ	110.293
Average cost	67.359

Table 5.18: UC^{2}AV lateral stability and control derivatives.

Parameter	**Value**	**CR bound**	**CR%**	**Insen %**
Y_w	-288.3	45.290	15.710	2.223
L_q	-9.992	5.924	59.290	1.817
Y_{δ_a}	4.528	0.461	10.190	1.425
L_{δ_a}	-0.025	0.015	60.110	1.843
τ	0.208	0.017	8.219	2.985

Table 5.18 show the stability and control derivatives while Table 5.19 show the lateral dynamic modes. The dynamic modes indicate that the UC^{2}AV (CC-off) is laterally dynamically stable. The final model is shown below:

$$\dot{x} = \begin{pmatrix} -57.659 & 157.6775 & 2.246 \\ -0.1364 & -22.2047 & 0 \\ 0 & 1 & 0 \end{pmatrix} \begin{pmatrix} v \\ p \\ \phi \end{pmatrix} + \begin{pmatrix} 0.9056 \\ -0.0548 \\ -0.1385 \end{pmatrix} \begin{pmatrix} \delta_a \end{pmatrix} \tag{5.4}$$

Table 5.19: The lateral dynamic modes of the UC^{2}AV.

	Eigenvalues	f_n (Hz)	ζ	τ sec
Mode 1	-22.822	NA	NA	0.044
Mode 2	-57.042	NA	NA	0.017

Model Validation

Aileron doublet inputs (Figure 5.20) are applied and the UC^{2}AV response recorded (Figure 5.21). TIC and root mean square analysis reveal accurate model identification (Table 5.20).

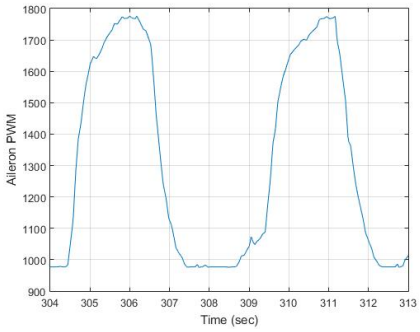

Figure 5.20: UC^{2}AV aileron doublet inputs (CC-off).

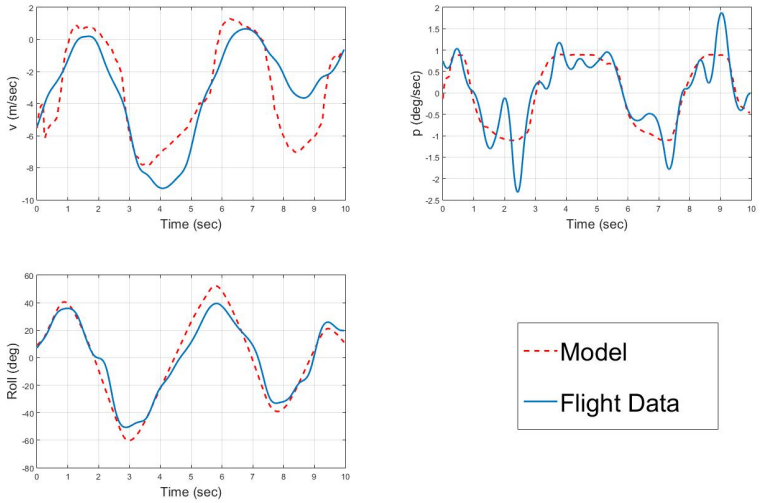

Figure 5.21: UC^{2}AV lateral model response (CC-off) vs. flight data.

Table 5.20: J_{rms} and TIC before and after calculation of biases and shifts for the UC^{2}AV CC-off lateral model.

	J_{rms}	TIC
Before calculation of biases and shifts	59.681	0.629
After calculation of biases and shifts	4.550	0.104

Although the final J_{rms} value is slightly greater than the minimum accepted standard, the model produces acceptable J_{rms} and TIC values. The final J_{rms} value is likely due to asymmetric roll rate response.

5.2.2 Circulation Control ON

Longitudinal Model

Model Derivation

Elevator sweeps are applied and the response of the UC^{2}AV recorded (Figures 5.22 and 5.23) while the CC system is turned on.

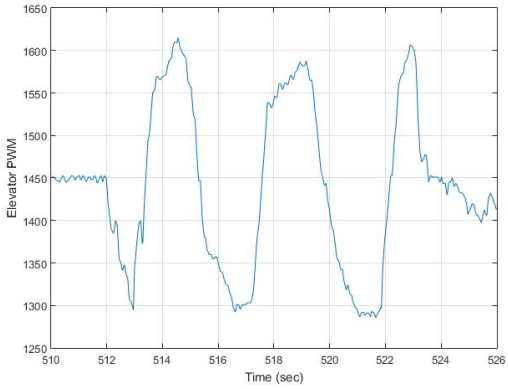

Figure 5.22: UC^{2}AV elevator sweep (CC-on).

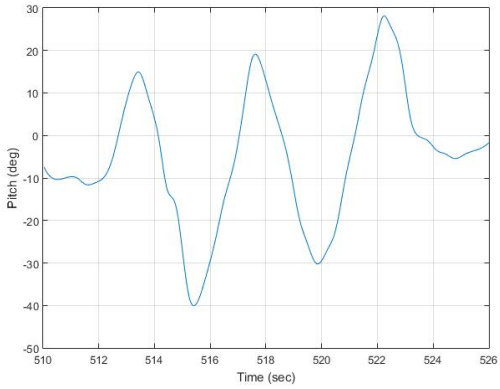

Figure 5.23: UC^{2}AV pitch response (CC-on).

Coherence values for each parameter are calculated (Table 5.21 and Figure 5.24). CIFER cost optimization function drives the mathematical models. The final cost values are presented in Table 5.22.

Table 5.21: Frequency ranges of model variables with acceptable coherence values.

	UC^{2}AV (Hz)
w	0.35-0.60
q	0.35-0.65
θ	0.35-0.75

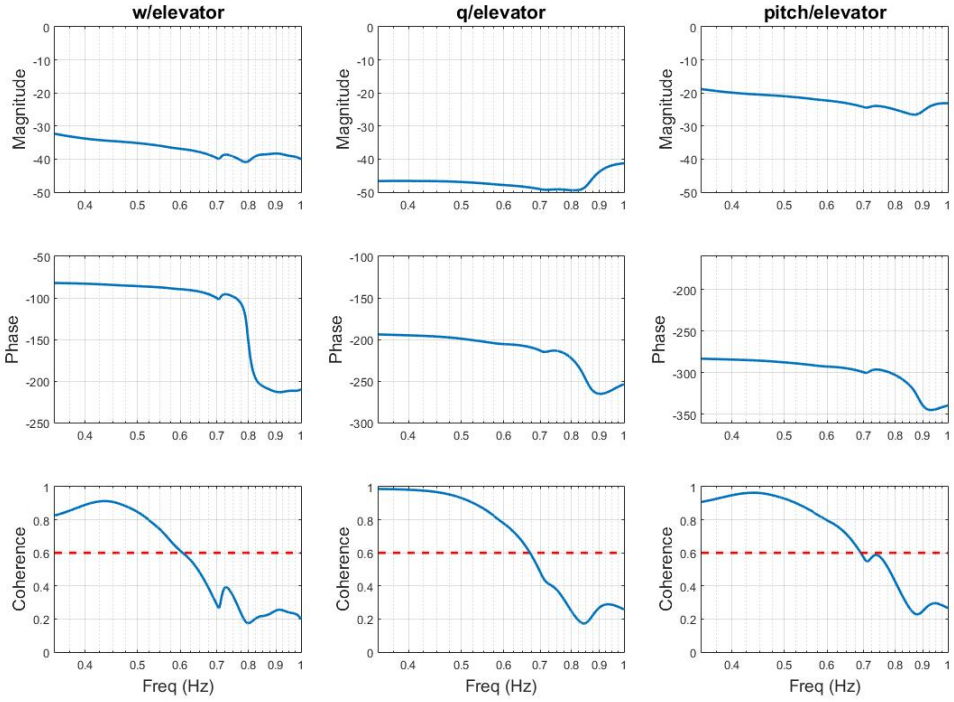

Figure 5.24: Longitudinal UC^{2}AV frequency response (CC-on).

It is noted that there is a small decrease in acceptable coherence range compared to UC^{2}AV (CC-off). It is difficult to identify the cause of this decrease because the acceptable coherence range reduction is relatively small (less than 1 Hz). Such a small reduction is too small to highlight the cause and could be caused by poor data quality. It is also noted that while the induced pitching moment causes changes in trim values, elevator sweeps produce similar peak to peak pitch amplitude values (CC-off and CC-on).

Table 5.22: Cost values after CIFER optimization.

	UC^{2}AV
w	45.874
q	92.407
θ	32.221
Average cost	56.834

Table 5.23 shows the final stability and control derivatives. It can be seen that $M_q < 0$ indicates the UC^{2}AV remains statically stable.

Table 5.23: Longitudinal UC^{2}AV (CC-on) stability and control derivatives.

Parameter	**Value**	**CR bound**	**CR%**	**Insen %**
Z_w	-0.216	3.9750	1840.000	177.00
Z_q	-2.858	32.8500	1149.000	53.92
M_w	-0.025	0.1934	785.600	82.39
M_q	-3.286	1.5430	46.950	2.39
Z_{δ_e}	0.243	0.0960	39.550	2.62
M_{δ_e}	-0.016	0.0004	28.360	2.11

Table 5.24 shows the dynamic modes of the UC^{2}AV. It can be seen that the modes are dynamically stable. The final longitudinal CC-on model is shown below:

$$\dot{x} = \begin{pmatrix} -0.0432 & -0.5716 & 0.2655 \\ -0.0492 & -6.5725 & 0 \\ 0 & 1 & 0 \end{pmatrix} \begin{pmatrix} w \\ q \\ \theta \end{pmatrix} + \begin{pmatrix} 0.0486 \\ -0.0316 \\ -0.3044 \end{pmatrix} \begin{pmatrix} \delta_e \end{pmatrix} \tag{5.5}$$

Table 5.24: The longitudinal dynamic modes of the UC^{2}AV (CC-on).

	Eigenvalues	f_n (Hz)	ζ	τ sec
Mode 1	-0.0192 ± 0.0402	0.0071	0.433	NA
Mode 2	-6.577	NA	NA	0.152

Model Validation

Doublet inputs are applied to the elevator and the response recorded (Figures 5.25 and 5.25).

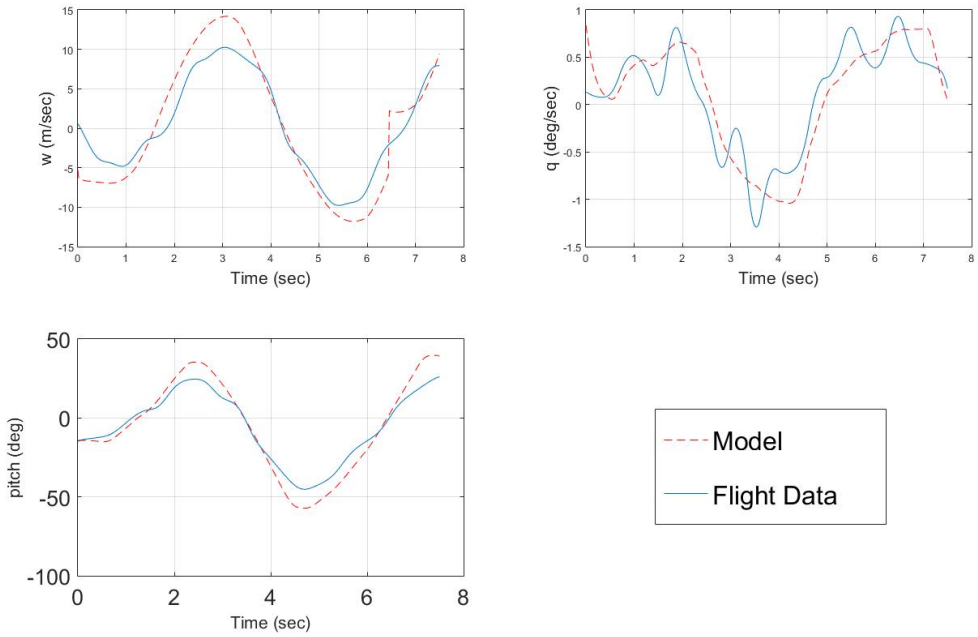

Figure 5.25: Longitudinal UC^{2}AV response (CC-on) vs. model response.

Table 5.25: J_{rms} and TIC before and after calculation of biases and shifts for the UC^{2}AV CC-on lateral model.

	J_{rms}	TIC
Before calculation of biases and shifts	26.132	0.609
After calculation of biases and shifts	4.934	0.158

The final J_{rms} does not meet the minimum standard requirement. This caused by poor doublet inputs that produce non-sinusoidal pitch rate response which in turn causes high J_{rms} values as can be seen in Figure 5.25. The final TIC value indicates that the model has acceptable predictive ability. It is also worth noting that the model accurately captures the pitch response of the UC^{2}AV (Figure 5.25). This implies that the negative pitching moment effect is appropriately modeled.

Lateral Model

Model Derivation

Aileron sweep inputs are applied and the response recorded (Figures 5.26 and 5.27) while the CC system is turned on. Table 5.26 and Figure 5.28 present the frequency ranges with acceptable coherence values.

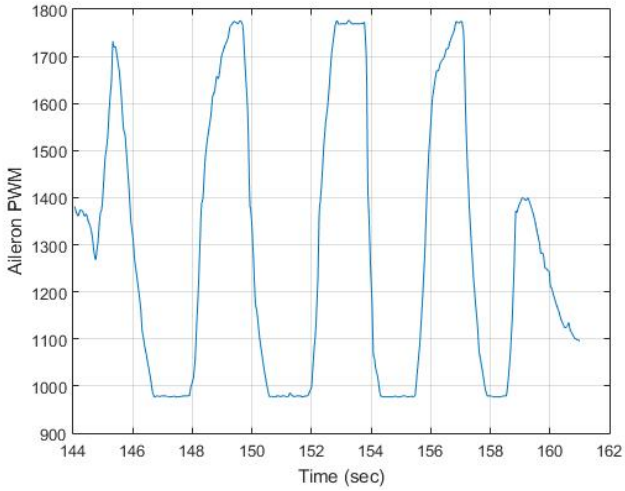

Figure 5.26: UC^{2}AV aileron sweeps (CC-on).

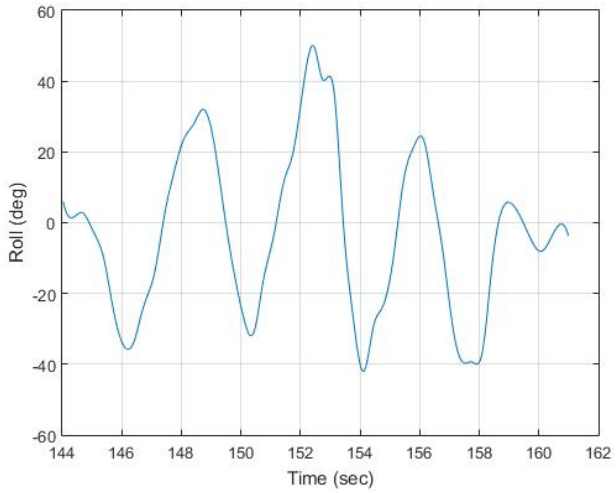

Figure 5.27: UC^{2}AV roll response to aileron sweeps (CC-on).

Table 5.26: Frequency ranges of model variables with acceptable coherence values.

	UC^{2}AV (Hz)
v	0.35-0.60
p	0.35-0.70
ϕ	0.35-0.70

There is a significant increase in lateral coherence values of UC^{2}AV (CC-on) compared to CC-off. As discussed, the UC^{2}AV implements small ailerons that cause a loss in lateral dynamic maneuverability. UC^{2}AV (CC-on) coherence values suggest that CC makes the UC^{2}AV more responsive to pilot inputs at higher frequencies. It is also worth noting that while the acceptable coherence range of roll and roll rate of the RMRC Anaconda is greater than UC^{2}AV (CC-on), the acceptable coherence range of lateral velocity v of the UC^{2}AV is greater than RMRC Anaconda by 2 Hz.

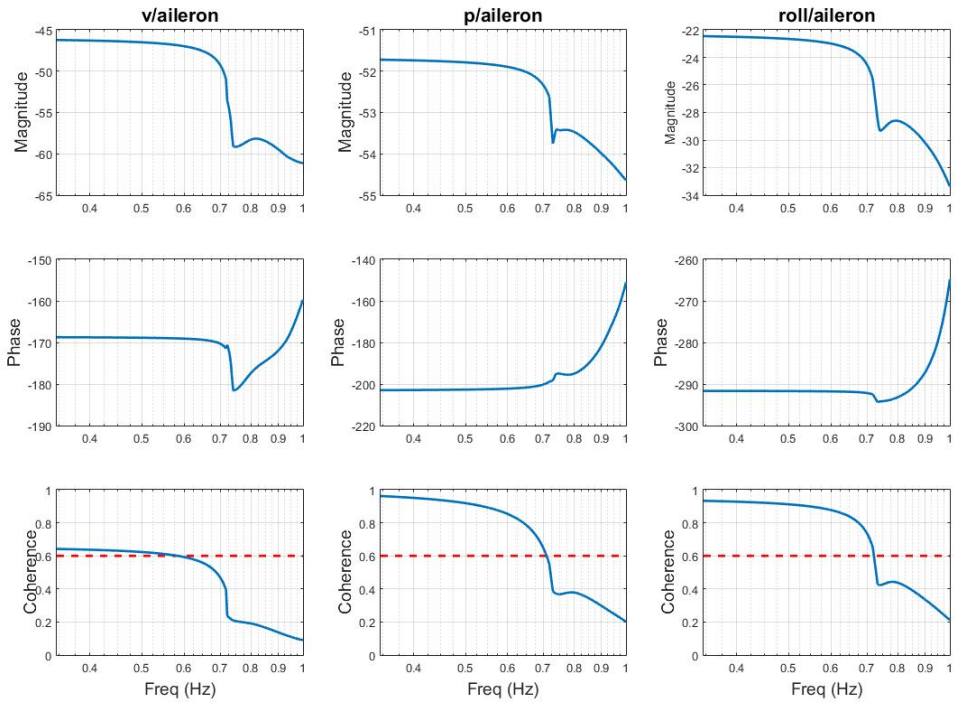

Figure 5.28: Lateral UC^{2}AV frequency response (CC-on).

The final cost values after CIFER optimization are shown in Table 5.27. The stability and control derivatives are presented in Table 5.28.

Table 5.27: Lateral UC^{2}AV (CC-on) Cost values after CIFER optimization.

	UC^{2}AV
v	62.71
p	10.54
ϕ	49.40
Average cost	40.88

Table 5.28: UC^{2}AV stability and control derivatives.

Parameter	**Value**	**CR bound**	**CR%**	**Insen %**
Y_w	-210.400	230.300	109.500	5.257
L_q	0.509	5.577	1096	32.990
Y_{δ_e}	-4.199	1.225	29.160	1.413
L_{δ_e}	0.019	0.014	72.930	2.195
τ	0.077	0.014	18.730	5.732

Table 5.29 indicates that the UC^{2}AV remains laterally dynamically stable with turning CC on. The final CC-on lateral model can be seen below:

$$\dot{x} = \begin{pmatrix} -42.0748 & -283.8869 & 0 \\ 7.9463 & 1.1313 & 0 \\ 0 & 1 & 0 \end{pmatrix} \begin{pmatrix} v \\ p \\ \phi \end{pmatrix} + \begin{pmatrix} -0.8399 \\ 0.0441 \\ -0.2147 \end{pmatrix} \begin{pmatrix} \delta_a \end{pmatrix} \tag{5.6}$$

Table 5.29: The longitudinal dynamic modes of the UC^{2}AV (CC-on).

	Eigenvalues	f_n (Hz)	ζ	τ sec
Mode 1	-20.471 ± 37.836	0.476	6.847	NA

Model Validation

Doublet inputs are applied to the aileron and the response is recorded (Figures 5.29 and 5.30). TIC and root mean square calculations are performed to determine the accuracy of the model (Table 5.30).

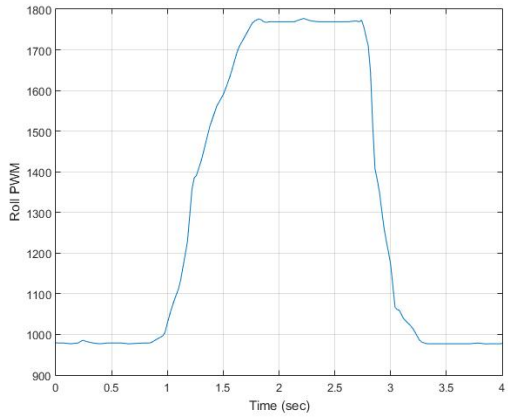

Figure 5.29: UC^{2}AV aileron doublet (CC-on).

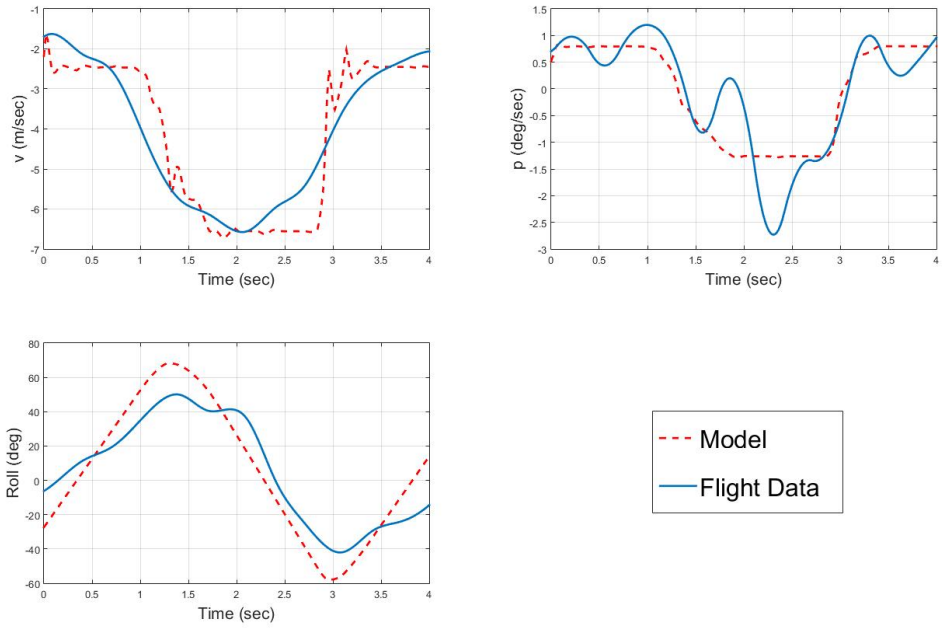

Figure 5.30: UC^{2}AV lateral model response (CC-on) vs. flight data.

Table 5.30: J_{rms} and TIC before and after calculation of biases and shifts for the UC^{2}AV CC-on lateral model.

	J_{rms}	TIC
Before calculation of biases and shifts	87.166	0.744
After calculation of biases and shifts	8.339	0.204

The final J_{rms} value does not meet the minimum standards. This is due to un-modeled nonlinear dynamics present in the response of the UC^{2}AV to the implemented doublet inputs. The final TIC value suggests that the mathematical model has acceptable predictive ability.

5.2.3 Remarks

The observations made after performing system identification using CC are summarized below:

- Negative pitching moment is observed while performing flight testing. The pitching moment causes changes in the aircraft trim values. However, this does not affect the UC^{2}AV stability properties. The derived models indicate that the UC^{2}AV (CC-on and CC-off) is statically and dynamically stable. Symmetric elevator sweeps around trim produce symmetric pitch, pitch rate, and vertical velocity w responses. Elevator sweeps in CC-on and CC-off cases produce similar responses. This can also be observed by examining the magnitude and phase plots of longitudinal frequency response (Figures 5.15 and 5.24). It can be seen from the two bode plots that the magnitude gain and phase shift is relatively the same for all identified parameters across the frequency range (CC-on and CC-off). A CC induced change in longitudinal trim values is also noted. The elevator trim values change from a PWM value

of 1400 μs to 1480 μs. This is nearly a 10% reduction in the total elevator inputs available for ascending altitude (pitching up).

As discussed in section (3.3.1), there are two longitudinal UAV dynamic modes. These are the phugoid mode, which is a low frequency mode, and the short period mode, which is a high frequency mode. It is known that the forward velocity u is only dynamically present in the phugoid mode [57]. Simulation experiments results presented in Chapter 4 indicate that u is dynamically present at frequencies < 0.20 Hz. Therefore, it can be concluded that the RMRC Anaconda and UC^{2}AV phugoid modes have frequencies < 0.20 Hz. Due to radio communication range, dynamics at frequencies > 0.35 Hz were captured (short period mode only). Therefore, the CC-on results indicate that CC does not affect the short period mode dynamics. However, it was noted that while the UC^{2}AV (CC-off) was able to consistently achieve pitch angle values between $+35^\circ$ to $+45^\circ$ at the lower frequencies (0.35-0.45 Hz), the UC^{2}AV (CC-on) was unable to consistently achieve such values and was limited to pitch values between $+25^\circ$ to $+35^\circ$ in many of the recorded data. This along with the new trim elevator values are an indication that the UC^{2}AV (CC-on) is unable to achieve the same pitch angles of the UC^{2}AV (CC-off) in the phugoid dynamic mode (frequency $<$ 0.35 Hz) due to the negative pitching moment effect.

- There is a reduction of the frequency range with acceptable coherence values for all longitudinal parameters (CC-off) compared to the RMRC Anaconda. This is likely caused by the additional weight of the UC^{2}AV.

- There is a significant reduction of the frequency range with acceptable coherence values for all lateral parameters (CC-off) compared to the RMRC Anaconda. This mainly caused by the small ailerons implemented on the CCW (UC^{2}AV aileron surface area = $\frac{1}{3}$ RMRC Anaconda aileron surface area) which reduces the lateral dy-

namic maneuverability of the UC^{2}AV.

- Lateral system identification of the UC^{2}AV (CC-on) produces a larger frequency range with acceptable coherence values when compared to UC^{2}AV (CC-off). This implies that CC improves the lateral maneuverability of the UC^{2}AV. However, the lateral UC^{2}AV (CC-on) coherence range is smaller than the lateral RMRC Anaconda range. This indicates that while CC does improve the lateral maneuverability, it does not compensate for lost aileron surface area.

- The mathematical models capture the dynamics associated with acceptable coherence values. Therefore, the models capture the improved lateral response of the UC^{2}AV.

- Some stability and control derivatives calculated for the CC-on models have large Cramér Rao bounds and percentages. This makes parameter estimation analysis using the obtained results unreliable. However, the Cramér Rao percentages and bounds can be reduced by collecting more data for system identification.

Chapter 6

Conclusion and Future Work

6.1 Conclusion

In this thesis, a system identification method is developed and implemented for a Class-I Circulation Control UAV. There has been a lot of work done to understand the aerodynamic properties of CC in wind tunnel environments. However, analysis of the effects of CC on a UAV equations of motions has not been performed. The aim of this thesis is to develop an understanding of the effects of CC on UAV dynamics. System identification is performed on a CC UAV with the CC system turned on and off. Derivation of mathematical models and parameter estimation of stability and control derivatives are performed. The mathematical models are to be used in the future to design autopilot algorithms.

Flight tests are held to investigate the effects of CC on UAV dynamics. A system identification method is then presented to capture the CC effects. The proposed method is first implemented in a simulation environment. To do so, a simulation platform is designed using X-Plane and Matlab. Simulation system identification produce accurate simulated mathematical models. An avionic system consisting of a sensory system and software system are developed to allow system identification with flight testing. System identification

is first performed on a baseline UAV with known aerodynamic properties. Afterwards, system identification is performed on the CC UAV.

Data collected from flight tests indicate that CC induces a noise down pitching moment effect which alters the dynamic properties of the UAV. The CC UAV models derived capture the noise down pitching moment effect as indicated by the validation experiments. Derivation of longitudinal and lateral dynamic models highlights the effects of CC on the decoupled motions. It was observed that besides changing trim values, CC does not effect the longitudinal dynamics or stability properties of the CC UAV. CC does change the lateral dynamics by making the UAV dynamically sensitive (more responsive) to high frequency pilot inputs while the dynamics at low frequency inputs remain largely unchanged. Data collected indicate that CC does not change the lateral trim values.

6.2 Future Work

Although the proposed method has produced acceptable models, there are a number of steps that could be taken to improve the quality of the models. The implemented method in this thesis uses initial stability and control derivative values by analyzing similar Class-I UAVs (weight and size) with known mathematical models. Identification of initial baseline stability and control derivatives using wind tunnel tests should improve the accuracy of the models. The algorithm developed in this thesis implements a Kalman based sensor fusion algorithm between an IMU and a GPS sensors. The sensor fusion algorithm assumes Gaussian noise distribution which could lead to inaccurate velocity estimation. The IMU sensor is unable to capture highly dynamic lateral motion without sensor fusion with the GPS. Upgrading the IMU sensor should therefore improve the accuracy of the estimated lateral velocity. System identification using more flight data will also increase the reliability of the model.

Bibliography

[1] N. V. Hoffer, C. Coopmans, A. M. Jensen, and Y. Chen, *A Survey and Categorization of Small Low-Cost Unmanned Aerial Vehicle System Identification*. Journal of Intelligent Robotic Systems, 2014.

[2] N. V. Hoffer, C. Coopmans, R. Fullmer, and Y. Chen, *Small Lost Cost Unmanned Aerial Vehicle System Identification By Error Filtering Online Learning (EFOL) Enhanced Least Squares Method*. 2015 International Conference on Unmanned Aircraft Systems, 2015.

[3] A. Dorobantu, A. M. Murch, B. Mettler, and G. J. Balas, *Frequency Domain System Identification for a Small, Low-Cost, Fixed-Wing UAV*. AIAA Guidance, Navigation, and Control Conference, 2011.

[4] J. Harris, F. Arthurs, J. V. Henrickson, and J. Valasek, *Aircraft System Identification using Artificial Neural Networks with Flight Test Data*. International Conference on Unmanned Aircraft Systems, 2016.

[5] R. Sparks, S. Michie, and K. Gill, *Development of an Integrated Circulation Control Fluidic Thrust Vectoring Flight Test Demonstrator*. 1st International Conference on Innovation and Integration in Aerospace Sciences, Queen's University Belfast, Northern Ireland, UK, 2005.

[6] G. A. I. Monterzino and C. P. Lawson, *Development of a Pneumatic System to Enable Flight without Conventional Control Surfaces*. 27th International Congress of the Aeronautical Sciences, Nice France, 2010.

[7] N. R. Alley, J. Steele, J. C. Neidhoefer, R. J. Englar, and G. Blaylock, *Development of a Cruise-Efficient Extreme-STOL-Capable Demonstrator UAV*. AIAA Infotech@Aerospace 2010 20 - 22 April 2010, Atlanta, Georgia, 2010.

[8] W. C. Horne and N. J. Burnside, *AMELIA CESTOL Test: Acoustic Characteristics of Circulation Control Wing and Leading- and Trailing-Edge Slot Blowing*. 51st AIAA Aerospace Science Meeting including theNew Horizons Forum and Aerospace Exposition, Dallas, Texas, 2013.

[9] W. E. Milholen, G. S. Jones, D. T. Chan, S. L. Goodliff, S. G. Anders, L. P. Melton, M. B. Carter, B. G. Allan, and F. J. Capone, *Enhancements to the FAST-MAC Circulation Control Model and Recent High-Reynolds Number Testing in the National Transonic Facility*. 31st AIAA Applied Aerodynamics Conference San Diego CA, 2013.

[10] K. Kanistras, M. J. Rutherford, and K. P. Valavanis, *Development of a Circulation Control Wing for UAVs*. IEEE Aerospace Conference, Montana, 2014.

[11] K. Kanistras, M. J. Rutherford, N. Vitzilaios, and K. P. Valavanis, *Experimental Study of Circulation Control Wings at Low Reynolds Numbers*. 32nd Applied Aerodynamics Conference, AIAA Aviation, Atlanta, 2014.

[12] K. Kanistras, S. P. Chander, K. P. Valavanis, and M. J. Rutherford, *Low Speed Wing Tunnel Investigation of a Circulation Control Wing for Enhanced Lift*. 33rd Applied Aerodynamics Conference, AIAA Aviation, Dallas, 2015.

[13] G. S. Jones, W. E. Milholen, D. T. Chan, B. G. Allan, S. L. Goodliff, L. P. Melton, S. G. Anders, M. B. Carter, and F. J. Capone, *Development of the Circulation Control Flow Scheme used in the NYF Semi-Span FAST-MAC Model*. 31st AIAA Applied Aerodynamics Conference San Diego CA, 2013.

[14] J. B. Montanya and D. D. Marshall, *Circulation Control and its Application to Extreme Short Take-Off and Landing Vehicles*. 45th AIAA Aerospace Sciences Meeting and Exhibit, Reno, NV, 2007.

[15] R. Cory and R. Tedrake, *Experiments in fixed-wing uav perching*. AIAA Guidance, Navigation, and Control Conference, 2008.

[16] R. Teo, J. Jang, and C. Tomlin, *Automated multiple uav flight-the stanford dragonfly uav program*. 43rd IEEE Conference on Decision and Control, vol. 4, pp. 4268 to 4273, 2004.

[17] V. Puttige and S. Anavatti, *Real-time neural network based online identification technique for a uav platform*. Proceedings of the International Conference on Computational Intelligence for Modelling Control and Automation, and International Conference on Intelligent Agents, Web Technologies and Internet Commerce, 2006.

[18] S. Carnduff, *System Identification of Unmanned Aerial Vehicles*. Ph.D. thesis, Cranfield University, 2008.

[19] R. Englar, G. Jones, B. Allan, and J. Lin, *2D Circulation Control Airfoil Benchmark Experiments Intended for CFD Code Validation*. AIAA Aerospace Sciences Meeting Including The New Horizons Forum and Aerospace Exposition, 2009.

[20] C. M. Cagle and G. S. Jones, *A Wind Tunnel Model to Explore Unsteady Circulation Control for General Aviation Applications*. 22nd AIAA Aerodynamic Measurement Technology and Ground Testing Conference, 2002.

[21] R. J. Englar, *Circulation Control Pneumatic Aerodynamics: Blown Force and Moment Augmentation and Modification; Past, Present and Future*. AIAA Paper, 2000-2541, presented at AIAA Fluids 2000 Meeting, Denver, CO, 2000.

[22] K. Kanistras, S. P. Chander, K. P. Valavanis, and M. J. Rutherford, *UC2AV Unmanned Circulation Control Aerial Vehicle for Short Takeoff and Enhanced Payload*. 34th Applied Aerodynamics Conference, AIAA Aviation, Washinton DC, 2016.

[23] P. C. Saka, K. Kanistras, M. J. Rutherford, and K. P. Valavanis, *Development of a Framework for a Circulation Control-Based Unmanned Aerial Vehicle*. IEEE Aerospace Conference, Montana, 2016.

[24] M. G. Alexander, S. G. Anders, and S. K. Johnson, *A Wind Tunnel Experiment for Trailing Edge Circulation Control on a 6Match Numbers*. 2004 NASA/ONR Circulation Control Workshop, 2005.

[25] W. Hoburg and R. Tedrake, *System identification of post stall aerodynamics for uav perching*. AIAA Infotech Aerospace Conference, pp. 1 to 9, 2009.

[26] Z. Li, N. Hoffer, B. Stark, and Y. Chen, *Design, modeling and validation of a t-tail unmanned aerial vehicle*. J. Intell. Robot. Syst. 69(1 to 4), 91 to 107, 2012.

[27] W. Debusk, G. Chowdhary, and E. Johnson, *Realtime system identification of a small multi-engine aircraft*. AIAA Atmospheric Flight Mechanics Conference, pp. 1 to 15, 2009.

[28] H. Wu, D. Sun, and Z. Zhou, *Model identification of a micro air vehicle in loitering flight based on attitude performance evaluation*. IEEE Trans. Robot. 20(4),702 to 712, 2004.

[29] M. Manani, A. Desbiens, and E. Gagnon, *Identification of a uav and design of a hardware-in-the-loop system for nonlinear control purposes*. AIAA Guidance, Navigation, and Control Conference, vol. 8, pp. 6441 to 6446, 2005.

[30] Y. Paw and G. Balas, *Development and application of an integrated framework for small uav flight control development*. Mechatronics 21(5), 789 to 802, 2011.

[31] J. Cho, J. Principe, D. Erdogmus, and M. Motter, *Modeling and inverse controller design for an unmanned aerial vehicle based on the self-organizing map*. IEEE Trans. Neural Netw. 17(2), 445 to 460, 2006.

[32] S. Salman, A. Sreenatha, and J. Choi, *Attitude dynamics identification of unmanned aircraft vehicle*. Int. J. Control. Autom. Syst. 4(6), 782 to 787, 2006.

[33] J. Dongwon and T. Panagiotis, *Modeling and hardwarein-the-loop simulation for a small unmanned aerial vehicle*. 2007 AIAA Conference, 2007.

[34] J. Nino, F. Mitrache, P. Cosyn, and R. Dekeyser, *Model identification of a micro air vehicle*. J. Bionic Eng. 4(4), 227 to 236, 2007.

[35] Y. L. H. Chao, L. Di, and Y. Chen, *Model identification of a micro air vehicle Roll channel fractional order controller design for a small fixed-wing unmanned aerial vehicle*. Control. Eng. Pract. 18(7),761 to 772, 2010.

[36] E. Atkins, R. Miller, T. Plet, K. Shaw, W. Ribbens, and D. Washabugh, *Solus: an autonomous aircraft for flight control and trajectory planning research*. 1998 American Control Conference, 1998.

[37] S. Brunke and M. Campbell, *Estimation architecture for future autonomous vehicles*. 2002 American Control Conference, vol. 2, pp. 1108 to 1114, 2002.

[38] V. Puttige and S. Anavatti, *Comparison of real-time online and offline neural network models for a uav*. International Joint Conference on Neural Networks, pp. 412 to 417, 2007.

[39] V. Puttige and S. Anavatti, *Real-time multi-network based identification with dynamic selection implemented for a low cost uav*. 2007 IEEE International Conference on Systems Man and Cybernetics, pp. 759 to 764, 2007.

[40] V. Puttige and S. Anavatti, *Real-time system identification of unmanned aerial vehicles: a multi-network approach*. J. Comput. 3(7), 31 to 38, 2008.

[41] S. Hansen and M. Blanke, *Control surface fault diagnosis with specified detection probability real event experiences*. International Conference on Unmanned Aircraft Systems, pp. 526 to 531, 2013.

[42] W. Park, E. Kim, Y. Song, and B. Ko, *A study on the real-time parameter estimation of durumi ii for control surface fault using flight test data (longitudinal motion)*. Int. J. Control. Autom. Syst. 5(4), 410 to 418, 2007.

[43] J. Evans, G. Elkaim, and B. Parkinson, *System identification of an autonomous aircraft using gps*. ION Global Positioning System Conference, pp. 1065 to 1071, 1997.

[44] C. Hu, X. Huang, J. Hu, and J. Zhu, *System identification of a small uavs speeding up process before take-off*. 5th Asian Cotnrol Conference, 2004.

[45] J. Rao, Z. Gong, and Z. Jiang, *GA-based flight motion model parameter identification of a subminiature fixed-wing unmanned aerial vehicle*. IEEE International Conference on Mechatronics and Automation, pp. 3549 to 3554, 2007.

[46] A. Kallapur, S. Ali, and S. Anavatti, *Application of extended kalman filter towards uav identification*. Auton. Robots Agents 207, 199 to 207, 2007.

[47] Y. Luo, H. Chao, L. Di, and Y. Chen, *Lateral directional fractional order (pi) control of a small fixed-wing unmanned aerial vehicles: controller designs and flight tests*. IET Control Theory Appl. 5(18), 2156, 2011.

[48] Y. Nong, Z. Qi, and D. Lin, *System identification of a small unmanned aerial vehicle based on time and frequency domain technologies*. 2011 9th World Congress on Intelligent Control and Automation, pp. 711 to 718, 2011.

[49] D. Jung, E. L. D. Zhou, R. Fink, J. Moshe, A. Earl, and P. Tsiotras, *Design and development of a low cost test-bed for undergraduate education in uavs*. 44th IEEE Conference on Decision and Control, pp. 2739 to 2744, 2005.

[50] M. Liu, G. Egan, and Y. Ge, *Identification of attitude flight dynamics for an unconventional uav*. IEEE/RSJ International Conference on Intelligent Robots and Systems, pp. 3243 to 3248, 2006.

[51] E. A. Morelli, *Practical Aspects of the Equation Error Method for Aircraft Parameter Estimation*. AIAA Atmospheric Flight Mechanics Conference, 2006.

[52] V. Klein and E. A. Morelli, *Aircraft System Identification Theory and Practice*. AIAA, 2006.

[53] M. B. Tischler and R. K. Remple, *Aircraft and Rotorcraft System Identification: Engineering Methods with Flight Test Examples*. AIAA, 2006.

[54] K. Kirkpatrick, J. M. Jr., and J. Valasek, *Aircraft System Identification Using Artificial Neural Networks*. AIAA Aerospace Sciences Meeting including the New Horizons Forum and Aerospace Exposition, 2013.

[55] T. M. Inc., *Matlab Neural Network Toolbox Release*. MathWorks, 2015a.

[56] S. P. Chander, *Design and Development of an Air Supply System for an Unmanned Circulation Control Aerial Vehicle*. Masters Thesis, University of Denver, 2016.

[57] B. Etkin and L. D. Reid, *Dynamics of Flight Stability and Control*. John Wiley Sons, INC., 1996.

[58] B. Etkin and L. D. Reid, *Dynamics of Flight Stability and Control*. John Wiley and Sons INC., 1995.

[59] T. M. Foster, *Dynamic Stability and handling Qualities of Small Unmanned Aerial Vehicles*. Brigham Young University Provo, 2004.

[60] M. Agha, K. Kanistras, P. C. Saka, M. J. Rutherford, and K. P. Valavanis, *System Identification of a Circulation Control UAV Using X-Plane Flight Simulation Software and Flight Data*. AIAA Aviation 2017 Modeling and Simulation Conference, 2016.

[61] A. Bittar, H. Figuereido, and A. Mendes, *Guidance Software in the Loop simulation using X-Plane and Simulink for UAVs*. International Conference on Unmanned Aircraft Systems, 2014.

[62] D. M. Agnecy, *The Universal Grids: Universal Transverse Mercator (UTM) and Universal Polar Sterographic (UPS)*. DMA Technical Manual, 1989.